UNIVERSITÉ DE BOURGOGNE
Laboratoire Interdisciplinaire Carnot de Bourgogne UMR CNRS 6303

NATIONAL ACADEMY OF SCIENCES OF ARMENIA
Institute for Physical Research

STUDY OF OPTICAL AND MAGNETO OPTICAL PROCESSES IN Rb ATOMIC VAPOR LAYER OF NANOMETRIC THICKNESS

by
Hrant HAKHUMYAN

A Thesis in Physics
Submitted for the Degree of
Doctor of Philosophy

Date of defense May 18 2012

Jury

David SARKISYAN	Professor IPR, NAS of ARMENIA, Ashtarak	Supervisor
Claude LEROY	Maître de Conférences ICB, Université de Bourgogne, Dijon	Supervisor
Yevgenya PASHAYAN-LEROY	Dr. of Physics ICB, Université de Bourgogne, Dijon	Co-Supervisor
Valeri PAKHALOV	Professor Yerevan State University, Yerevan	Referee
Atom MURADYAN	Professor Yerevan State University, Yerevan	Examiner
Hayk SARGSYAN	Professor Russian-Armenian State University, Yerevan	Examiner

Referees

Stefka CARTALEVA	Professor Institute of Electronics, BAS, Sofia	Referee
Valeri PAKHALOV	Professor Yerevan State University, Yerevan	Referee

LABORATOIRE INTERDISCIPLINAIRE CARNOT DE BOURGOGNE-UMR CNRS 6303
UNIVERSITE DE BOURGOGNE, 9 AVENUE A. SAVARY - 21078 DIJON - FRANCE

INSTITUTE FOR PHYSICAL RESEARCH, NATIONAL ACADEMY OF SCIENCES OF ARMENIA ASHTARAK-2, 0203 ARMENIA

Remerciements

J'aimerais exprimer ma grande considération à mes Directeurs de thèse, les Professeurs David Sarkisyan, Claude Leroy et Yevgenya Pashayan-Leroy pour leur soutien moral et scientifique et leur patience.

Je remercie l'Ambassade de France en Arménie pour son aide financière, notamment la bourse No. 2009-3684 en tant que Boursier du Gouvernement Français. Je veux remercier Jean-Paul Martin et Anne Rosensthiel du SCAC pour leur grande aide pendant ces trois années. Ce financement m'a aussi permis de découvrir les traditions françaises et d'appréhender les frontières de la Physique.

Je voudrais aussi remercier tous mes collègues et tout le personnel de l'Institute for Physical Research de l'Académie des sciences d'Arménie et du Laboratoire Interdisciplinaire Carnot de Bourgogne de l'université de Bourgogne pour leur aide et leur chaleureuse camaraderie.

Acknowledgments

I would like to express my sincere gratitude to my supervisors Profs. David Sarkisyan, Claude Leroy and Yevgenya Pashayan-Leroy for their moral and scientific support and patience.

I acknowledge the support of French Embassy in Armenia for Grant No. 2009-3684 as Boursier du Gouvernement Français. I want to thank Jean-Paul Martin et Anne Rosensthiel of the SCAC for their great help during these three years. This grant allowed me to discover the French traditions and learn frontiers of Physics.

I would also like to thank all the co-workers and staff of the Institute for Physical Research of National Academy of Sciences and Laboratoire Interdisciplinaire Carnot de Bourgogne of University of Bourgogne for the valuable assistance, kindly and warmhearted attitude.

Research conducted in the scope of the International Associated Laboratory IRMAS (CNRS-France & SCS-Armenia)

Part of the research leading to these results has received funding from the European Union FP7/2007-2013 under grant agreement n° 205025 - IPERA

Etude des processus optiques et magnéto-optiques dans une couche de vapeur de rubidium atomique d'épaisseur nanométrique

Les progrès réalisés dans la fabrication de lasers à bande étroite, continus, accordables (CW) (largeur spectrale $\gamma_L \sim 1$ MHz), résonnants avec les transitions atomiques du rubidium et du césium, ont accru les recherches dans le domaine de la spectroscopie à haute résolution. L'utilisation de diodes lasers modernes (DL) a permis de développer des techniques expérimentales qui sondent précisément la structure hyperfine des vapeurs de métaux alcalins.

Il y a de nombreux avantages à étudier les métaux alcalins : i) dans le domaine des fréquences optiques utilisées, les vapeurs alcalines ont un moment dipolaire important de transition depuis l'état fondamental et il en résulte une forte absorption et une fluorescence importante ; ii) la densité de vapeur peut être facilement changée en faisant varier la température de la cellule ; iii) la présence d'un seul électron de valence simplifie l'étude théorique du système en interaction.

Un grand nombre de processus cohérents et de processus magnéto-optiques, qui peuvent être réalisés par l'interaction de vapeurs atomiques et de lasers à bande étroite, trouvent leurs applications dans les techniques laser, en métrologie (détermination hautement précise de fréquences de transitions atomiques et développement de nouvelles mesures précises du temps), le développement de jauges magnétiques hautement sensibles, en communication quantique, le stockage optique d'informations et bien d'autres champs d'applications.

Les expériences faites avec des vapeurs de Rb ou de Cs sont réalisées avec une cellule en verre hermétiquement close mais qui peut contenir soit uniquement l'un de ces gaz soit un mélange de ces deux gaz ou même des mélanges avec d'autres gaz. Les cellules en verre sont adaptées à des températures autour de 100 °C, bien qu'à température ambiante le nombre

d'atomes de Rb et de Cs atteigne 10^{10} at./cm^3 ce qui est suffisant pour enregistrer un spectre d'absorption ou de fluorescence sous champ laser d'une DL à bande étroite. L'élargissement Doppler est une spécificité des processus d'absorption et de fluorescence, qui peut atteindre $400-600$ MHz et qui est beaucoup plus large que la largeur naturelle des transitions atomiques ($5-6$ MHz). Par conséquent, dû à un fort élargissement Doppler, une grande partie des transitions entre états de la structure hyperfine ne peut être résolue, ce qui conduit à des difficultés d'interprétation des raies atomiques, en particulier en présence de champs magnétiques et électriques extérieurs. Le développement de nouvelles méthodes spectroscopiques permettant une réduction de l'élargissement Doppler est actuellement une thématique importante en spectroscopie à haute résolution.

Le but de ce travail de thèse est l'étude expérimentale et théorique des transitions atomiques des raies D_1 et D_2 entre sous-niveaux Zeeman de la structure hyperfine du rubidium dans un champ magnétique variant de 5 à 7000 G. Les spectres seront réalisés à l'aide d'un laser continu à bande étroite interagissant avec une vapeur alcaline confinée dans une nano-cellule. Les applications pratiques de ce travail seront envisagées.

Le **chapitre I** présente un large panorama des méthodes spectroscopiques utilisées avec des cellules hermétiquement closes de dimension millimétrique ou centimétrique et compare ces méthodes avec celles utilisées avec des nano-cellules d'épaisseur variant de 300 à 800 nm. Les techniques expérimentales sont présentées. La construction d'une nano-cellule et d'une cellule multi-régions (deux cellules interconnectées : une nano-cellule et une cellule ordinaire) est précisément décrite. La spectroscopie sub-Doppler à l'aide d'une nano-cellule est comparée à d'autres techniques sub-Doppler : absorption saturée, réflexion sélective, jet atomique, piégeage cohérent de population et les méthodes utilisant la configuration de Ramsey pour des cellules centimétriques.

Le **chapitre II** s'intéresse à l'influence des paramètres expérimentaux tels que : intensité du laser, effets dus à l'addition d'un gaz tampon, modification de l'épaisseur de la colonne de vapeur alcaline dans l'intervalle $\lambda/2 - 4\lambda$, influence de la densité de vapeur atomique sur la largeur spectrale des raies résonnantes de fluorescence et des raies VSOP ("Velocity Selective Optical Resonance") afin de déterminer les paramètres exprérimentaux optimaux. Nous présentons un modèle théorique décrivant l'influence d'un gaz tampon additionnel sur les spectres de transmission et de fluorescence. Nous décrivons, expérimentalement et théoriquement, les particularités de l'élargissement du spectre dû à un gaz tampon dans le cas d'une nano-cellule et dans le cas d'une cellule ordinaire. Nous démontrons expérimentalement l'influence de l'intensité laser et de l'épaisseur de la nano-cellule -pour une épaisseur variant de $\lambda/2$ à λ- sur les spectres de fluorescence et transmission. L'influence de la température de la nano-cellule, qui détermine la densité d'atomes est démontrée expérimentalement, la densité d'atomes déterminant l'élargissement auto-collisionnel qui modifie les spectres de fluorescence et transmission.

Le **chapitre III** propose une description théorique des systèmes alcalins de type hydrogénoïde en interaction avec un champ magnétique excitateur. Le modèle mathématique décrivant le processus d'interaction est présenté. Le codage informatique, les méthodes mathématiques à la base de ce modèle sont expliqués ainsi que l'écriture d'un programme informatique qui permet de calculer les décalages de fréquence et les modifications d'intensité des transitions hyperfines (D_1 et D_2) entre sous-niveaux Zeeman d'atomes alcalins (plus particulièrement pour le rubidium). Le programme informatique est appliqué au rubidium ^{85}Rb et ^{87}Rb pour les trois polarisations σ^+, π et σ^- de l'excitation laser et nous discutons de caractéristiques particulières des transitions Zeeman pour ces deux isotopes Rb dans le cas de ces trois polarisations.

Enfin le **chapitre IV**, qui est logiquement connecté au **chapitre III**, justifie expérimentalement les résultats numériques obtenus au **chapitre III**. Trois méthodes d'études expérimen-

tales utilisées sont décrites : i) la technique "λ-Zeeman", basée sur le spectre de transmission d'une nano-cellule d'épaisseur égale à la longueur d'onde du laser excitateur ; ii) la technique "$\lambda/2$-Zeeman" qui est une méthode basée sur le spectre de fluorescence d'une nano-cellule d'épaisseur égale à la moitié de la longueur d'onde de la radiation laser ; iii) la technique "λ-Fluorescence-Zeeman" qui est une méthode basée sur le spectre de fluorescence d'une nano-cellule d'épaisseur égale à la longueur d'onde du champ laser. Nous démontrons qu'en utilisant ces trois techniques, il est possible d'étudier simultanément les décalages de fréquence et les variations d'intensité de transitions isolées entre sous-niveaux Zeeman pour les raies D_1 et D_2 de $^{85,\ 87}$Rb dans le cas des polarisations σ^+, π et σ^- du laser pour un champ magnétique variant de 5 à 7000 G. De même nous avons étudié le comportement des transitions interdites (interdites pour un champ magnétique nul). Nous proposons une configuration expérimentale qui permet de mesurer de faibles champs magnétiques de l'ordre de 5 G et avons étudié le régime Paschen-Back de la raie D_1 du ^{87}Rb pour un champ magnétique entre 0,5 et 0,7 tesla. La modification des caractéristiques quantiques du système étudié, en interaction avec un fort champ magnétique, est mise en évidence. Enfin une comparaison exhaustive des résultats théoriques et des données expérimentales est établie pour toutes les valeurs du champ magnétique.

Contents

Introduction

The relevance of the subject

The progress achieved in the fabrication of smoothly tunable narrowband continuous wave (CW) lasers (linewidth $\gamma_L \sim 1$ MHz) which are resonant with atomic transitions of Rb and Cs, provides increasing of researches in the field of high resolution spectroscopy. Usage of modern diode lasers (DL) allows to develop experimental technique to investigate the hyperfine structure of alkali metal vapours.

There are several advantages which lead to high interest investigation with alkali metals: i) in optical domain alkali metals have strong dipole momenta of transitions from ground states that cause strong absorption and fluorescence; ii) density of vapour can be easily changed by varying the cell temperature; iii) presence of a single valence electron simplifies the theoretical consideration of the system for various conditions.

A number of different coherent and magneto-optical processes which can be realized through interaction of atomic vapours with the narrowband lasers, find applications in laser technique, metrology (high precision determination of atomic transition frequencies and development of new standards of time), in development of high sensitive magnetic gauges, in quantum communication, information optical storage and many other fields.

To make experiment with vapours of Rb and Cs it is convenient to use sealed-off glass cell, which may contain pure vapours of these metals or mixture of Rb and Cs vapours either mixtures with other gases. Glass cells are suitable up to temperatures around 100 °C, although at the room temperature the number of atoms of Rb and Cs reaches 10^{10} at./cm^3

that is enough for registration of resonant absorption and fluorescence in field of radiation of narrowband DL. The Doppler-broadening is a peculiar characteristic of absorption and fluorescence processes, which may reach up to $400 - 600$ MHz and it is much broader in comparison with natural width of atomic lines ($5 - 6$ MHz). Hence, because of strong Doppler-broadening, a major part of transitions between states of the hyperfine structure can not be resolved and it leads to complications in the process of study of atomic states, particularly in presence of external magnetic and electric fields. Presently, it is an important area of investigation in high resolution spectroscopy: development of new methods, which allow a strong reduction of the Doppler-broadening and thus improvement of the spectral resolution of different atomic transitions and achieve natural linewidth, which is caused by lifetime of hyperfine atomic states (in some cases it is possible to reach subnatural spectral width).

In the 90s a large number of theoretical and experimental articles were published demonstrating new possibilities of usage of thin sealed-off glass cells [26–35], which allow to confine atomic vapour column in space with thickness variable from 10 to 100 micrometers. The usage of these cells allows to form optical resonances with sub-Doppler linewidth (from 10 to 100 MHz), although is it necessary to use supplementary techniques such as frequency modulation of laser radiation and implementation of technique of synchronous detection [33–35]. Since 2001 [36–42], it has been demonstrated that using nano-cells which have thickness of column of atomic vapour equal to a few hundreds of nanometers (cells fabricated from technical sapphire (i.e. sapphire grown in artificial way) and suitable up to 500 °C), allows one to obtain resonances with sub-Doppler width equal to $15 - 70$ MHz. The usage of these cells allows to obtain sub-Doppler resonances without any supplementary techniques. At the same time the following two processes are used: 1) In the transmission spectra of a nano-cell filled with vapours of rubidium (or cesium) atoms ($D_{1,\ 2}$ lines), having the column thickness $L = \lambda$ (λ is the wavelength of the resonant radiation equal to 794 or 780 nm for D_1 and D_2 lines, correspondingly), in case of use of tunable laser radiation, narrow velocity selective optical resonances (VSOP) are formed located at the atomic transitions with a spectral width

$15 - 20$ MHz; 2) In the fluorescence spectra of a nano-cell filled with the vapours of Rb (D_1 and D_2 lines), with the thickness of the column $L = \lambda/2$ narrow peaks of fluorescence with a spectral width $60 - 70$ MHz are formed. This narrowing is based on coherent Dike narrowing effect [39, 43]. The preliminary results showed that the application of VSOP and the narrow-band resonance fluorescence (FL) allow us to investigate successfully the behaviour of the atomic transitions of the hyperfine structure of Rb (or Cs) atoms, particularly to investigate the behaviour of the rubidium atomic transitions between Zeeman sublevels in external magnetic fields.

Based on the foregoing, one might expect that the use of narrow optical resonances will allow to realize the further investigation of Rb atomic transitions in a large range of values of the magnetic field, and use the results to practical applications. It was also important from a scientific point of view to investigate the influence of experimental parameters on the resonances mentioned above, in order to obtain the optimal experimental parameters.

The aim of the work is the experimental and theoretical study of the behaviour of individual atomic transitions of the hyperfine structure of Rb D_1 and D_2 lines between the Zeeman sublevels in external magnetic fields in a range of magnetic fields $5 - 7000$ G with the use of a narrow-band CW laser, within a nano-cell, as well as the study of the possibility of the practical applications of the obtained results.

Objectives of the thesis:

1. The development of the installation based on permanent magnets, which allows us to form strong magnetic fields with the possibility to place inside a Rb nano-cell with a heater and the possibility of transmission and recording of laser radiation.

2. The investigation of the influence of experimental parameters such as laser intensity, addition of buffer gas, change of the thickness of the column of vapour in the range of $\lambda/2 - 4\lambda$, influence of the vapour density of atoms on the value of the spectral

width of the FL and VSOP resonances for the following further use: the study of the behaviour of the frequency and intensity (the transition probabilities) of the atomic hyperfine structure transitions between the Rb, D_1 and D_2 lines Zeeman sublevels in high external magnetic fields.

3. The development of computational software, which allows to determine the frequency and intensity of atomic transitions between Zeeman sublevels in high magnetic fields for D_1 and D_2 lines of atomic Rb.

Scientific novelty:

1. Using a narrow-band resonant fluorescence from a nano-cell with a thickness of $L = \lambda/2$, and VSOP resonances formed at a thickness $L = \lambda$, for the first time it was experimentally investigated the behaviour of the frequency and intensity (transition probabilities) of the atomic hyperfine structure transitions between the ^{85}Rb, ^{87}Rb, D_1 and D_2 lines Zeeman sublevels in external magnetic fields in range $5 - 7000$ G. The behaviour of tens of previously unstudied atomic transitions was analyzed and it is demonstrated that the intensities of these lines can both greatly increase, and decrease (tenfold).

2. For the first time it is demonstrated that for certain values of the magnetic fields the probability of the "forbidden" transitions (at zero magnetic field) ^{87}Rb, D_2 line, $F_g = 1 \to F_e = 3$ (three transitions between the Zeeman sublevels for a σ^+ polarization of exciting radiation), $F_g = 1 \to F_e = 1$ and $F_g = 1 \to F_e = 3$ (one in each group of transitions between the Zeeman sublevels for a π polarization of exciting radiation); ^{87}Rb, D_1 line, $F_g = 1 \to F_e = 1$ (one transition between the Zeeman sublevels for a π polarization of exciting radiation), strongly increases and exceeds the probability of the allowed atomic transitions. Frequency shift of the strong atomic transition ^{87}Rb, D_2 line, $F_g = 1, m_F = +1 \to F_e = 1, m_F = +1$ shows a particular behaviour: the frequency remains practically unchanged in the range of magnetic fields of $100 - 1100$ G.

3. A numerical program that allows us to calculate the frequency positions and the intensities of the atomic transitions between Zeeman sublevels in external magnetic fields in the range of $0 - 10\ 000$ G for D_1 and D_2 lines of atoms Rb, Cs and Na is developed. The theoretical curves are in good agreement with experimental results.

4. For the first time it is demonstrated that, in the case of partial pressure of neon buffer gas up to 6 torr into the nano-cell of thickness $L = \lambda$ filled with Rb, VSOP resonances are recorded confidently, while the addition of 0.1 torr neon buffer gas in the cells of a centimeter thickness leads to the complete disappearance of VSOP resonances formed with the help of the widely used technique of saturated absorption. It is demonstrated for the first time that the spectral width of the resonant fluorescence of the rubidium nano-cell with thickness $L = \lambda/2$, for all values of the neon buffer gas pressures is much narrower $(6 - 8$ times) compared with the resonant fluorescence of an ordinary centimeter cell containing rubidium with the same pressures of neon.

The practical value of the work:

1. It is implemented a simple construction of a magnetometer based on nano-cell filled with rubidium, which allows us to determine the magnitude of both homogeneous and strongly inhomogeneous magnetic field: a) using the resonant fluorescence in the range $30 - 2500$ G, and b) using the VSOP resonances formed at a thickness of nano-cell $L = \lambda$ in range $5 - 7000$ G.

2. It is implemented a simple construction based on the nano-cell filled with rubidium and a permanent magnet which allows us to realize the frequency reference shifted on $3 - 5$ GHz in respect with the initial atomic frequencies of Rb D_1 and D_2 lines.

3. The compact setup, based on permanent magnets, which allows to form strong magnetic field up to 7000 G, in a cylindrical region with a diameter of 50 mm and a thickness

of 25 mm, was made up. It is possible to place a test sample in this cylindrical region and to exposure it by a laser radiation.

4. By using the developed numerical program it is possible to determine correctly the frequency and the intensity of the atomic transitions between Zeeman sublevels of hyperfine structure in external magnetic fields in the range $5 - 7000$ G for D_1 and D_2 lines of alkali atoms.

5. Using the resonant fluorescence from a nano-cell with a thickness of $L = \lambda/2$ it is proposed the construction of the manometer that allows to measure the pressure of the buffer neon gas mixed with the hot vapours of rubidium atoms. The interval of the defined pressure of the buffer gas is $1 - 400$ torr. Measurements can be realized online.

The statements of the thesis:

1. The use of narrow-band resonance fluorescence from a nano-cell with a thickness $L = \lambda/2$ and $L = \lambda$ transmission allows one to study the behaviour of the frequency and the intensity of atomic hyperfine structure transitions of Rb, D_1 and D_2 lines between the Zeeman sublevels in external magnetic fields of $5 - 7000$ G. The intensities of large number transitions modify significantly (manyfold) in the range of magnetic field $5 - 7000$ G.

2. The intensity of the investigated six, initially "forbidden" atomic transitions between Zeeman sublevels of Rb, D_1 and D_2 lines, exceeds the intensity of the "allowed" atomic transitions in the range of the studied values of magnetic field. The frequency of the strong transition ^{87}Rb, D_1 line, $F_g = 1, m_F = +1 \rightarrow F_e = 1, m_F = +1$ shows a particular behaviour: it remains almost constant in the range of magnetic fields of $100 - 1100$ G.

3. The developed numerical program allows one to determine correctly the frequency positions and intensities of atomic transitions between Zeeman sublevels in the range

of magnetic field $0 - 10\ 000$ gauss for D_1 and D_2 lines of alkali atoms.

4. The VSOP resonances formed with the help of a nano-cell of thickness $L = \lambda$ filled with Rb with an additional neon buffer gas are confidently detected for values of pressure up to 6 torr. The spectral width of the resonance fluorescence of the rubidium nano-cell with a thickness $L = \lambda/2$ for all pressures of neon buffer gas is $6-8$ times narrower compared with the resonant fluorescence of an ordinary centimeter cell containing rubidium with the same pressures of neon.

Approbation of the Thesis Statements

The statements of the thesis were presented and discussed at the seminars of the Institute for Physical Research of Armenian NAS; at the Laboratoire Interdisciplinaire Carnot de Bourgogne at the CNRS - University of Bourgogne, reported at the conferences of atomic and laser physics "European Conference of Physics EGAS-40" (Graz, Austria, 2008), "European Conference of Physics EGAS-41" (Gdańsk, Poland, 2009), 16-th International School on Quantum Electronics "Laser physics and application" (Nessebar, Bulgaria, 2010), "European Conference on Atoms Molecules and Photons ECAMP-10" (Salamanca, Spain, 2010), "European Conference of Physics EGAS-43" (Fribourg, Switzerland, 2011), "High Resolution Molecular Spectroscopy HRMS-22" (Dijon, France, 2011), "Laser Physics-2005, 2007, 2008, 2009, 2010, 2011" (Ashtarak, Armenia, 2005, 2007-2011).

The main results of this dissertation were published as articles in 15 peer reviewed journals and 10 abstracts in the conference Book of Abstracts represented in bibliography [1–25].

The thesis, which consists of introduction, four chapters and References, comprises 149 pages, contains 81 figures, 2 tables and 125 references.

In ***Chapter I*** an overview of spectroscopic methods is given for ordinary sealed-off cells of centimeter and millimeter length in comparison with methods based on use of nanometric thick cells (nano-cell) of thickness varying in range $300 - 800$ nm. The experimental

technique is considered. Construction of a nano-cell and a multi-region cell is described: two interconnected nano- and ordinary cells. We explain the method of measuring nano-cell thickness. It is also demonstrated comparison of sub-Doppler spectroscopy based on usage of a nano-cell with other techniques of sub-Doppler spectroscopy: Saturated absorption, Selective reflection, Atomic beam, Coherent population trapping and methods using cells of $0.5 - 1$ cm.

In ***Chapter II*** it is discussed the influence of experimental parameters such as the laser intensity, the addition of a buffer gas, the change of the thickness of the column of vapour in the range of $\lambda/2-4\lambda$, the influence of the vapour density of atoms on the value of the spectral width of the FL and VSOP resonances for the further use to determine optimal experimental parameters. We develop theoretical model describing the influence of additional neon buffer gas on transmission and fluorescence spectra. Experimental and theoretical descriptions of peculiarities of the buffer broadened spectra of nano-cell compared with ordinary cell are given. It is experimentally demonstrated the influence of the laser intensity and nano-cell thickness varying in range of $\lambda/2-4\lambda$ on transmission and fluorescence spectra. The influence of a nano-cell temperature which determines the density of atoms is demonstrated, meanwhile the density of atoms determines the collisional self-broadening, which modifies transmission and fluorescence spectra.

In ***Chapter III*** it is represented a theoretical description of the hydrogen-like, alkali metals atomic systems interaction with the external magnetic field. The mathematical model describing theoretical background of interaction process is shown. It is explained main principle of computational model, mathematical methods and principles which is in the base of model; and numerical software which allows one to calculate the frequency shifts and intensity modifications of transitions between Zeeman sublevels of alkali metals (especially Rb) hyperfine structure D lines. The frequency shifts and intensity modifications of the transitions for ^{85}Rb and ^{87}Rb, D_1 and D_2 lines in case of σ^+, π and σ^- polarizations of exciting laser radiation are considered. It is represented detailed discussions about particular behaviour of different transitions between Zeeman sublevels of ^{85}Rb and ^{87}Rb, D_1 and D_2 lines in case of

σ^+, π and σ^- polarizations.

In ***Chapter IV***, which is logically interconnected with ***Chapter III***, it is demonstrated experimental justification of computational results considered in ***Chapter III***. It is considered three different methods for experimental study: i) "λ-Zeeman technique" - a method based on use of transmission spectrum of a nano-cell of thickness equal to laser radiation wavelength; ii) "$\lambda/2$-Zeeman technique" - a method based on use of narrow-band fluorescence spectrum of a nano-cell of thickness equal to the half of the laser radiation wavelength; iii) "λ-Fluorescence Zeeman technique" - a method based on use of narrow-band fluorescence spectrum of a nano-cell of thickness equal to laser radiation wavelength. We demonstrate that using these methods, it is possible to study both, frequency shifts and intensity modification of individual transition between Zeeman sublevels of $^{85,\ 87}$Rb D lines for σ^+, π and σ^- polarizations of laser radiation in the range of magnetic field values $5 - 7000$ G. It is also considered peculiarities of behaviour of "forbidden" at zero magnetic field transitions. It is developed configuration which allows to measure weak magnetic field of magnitude 5 G and studied Paschen-Back regime of ^{87}Rb D_1 line for values of magnetic field $0.5 - 0.7$ tesla $(5000 - 7000$ G). It is demonstrated that interaction with strong magnetic field significantly modifies quantum characteristics of the atomic system. The comparison of theoretical results with experimental data is exhibited for all studied values of the magnetic filed.

Chapter 1

Methods of forming sub-Doppler optical resonances

1.1 Experimental technique

a) Semiconductor CW diode lasers

Active development of techniques leads to fabrication of diode lasers radiating in the range $400 - 1000$ nm with high spectral and specific technical characteristics. These lasers have narrowband radiation with line $\gamma_L = 0.5 - 10$ MHz and intensity of radiation in the range $10 - 100$ mW. The more attractive characteristics of diode lasers are: the narrowband radiation, compactness and low power consumption and comparatively easy way to vary the wavelength of radiation. The high efficiency of diode lasers is conditioned by the way of the radiation generation which is realized by direct pumping of active media by electric current. The temperature and the pumping current determine wavelength of the radiation and due to that, it is thus important to have stable and noiseless power supply as well as good thermocontroller for stabilization of temperature of diode's case. For linewidth narrowing a external-cavity is used. Tunable external-cavity diode lasers (ECDL) usually use a diffraction grating as the wavelength selective element in the external resonator. They are also called grating-stabilized diode lasers. In our experiments we use the ECDLs with common Littrow configuration.

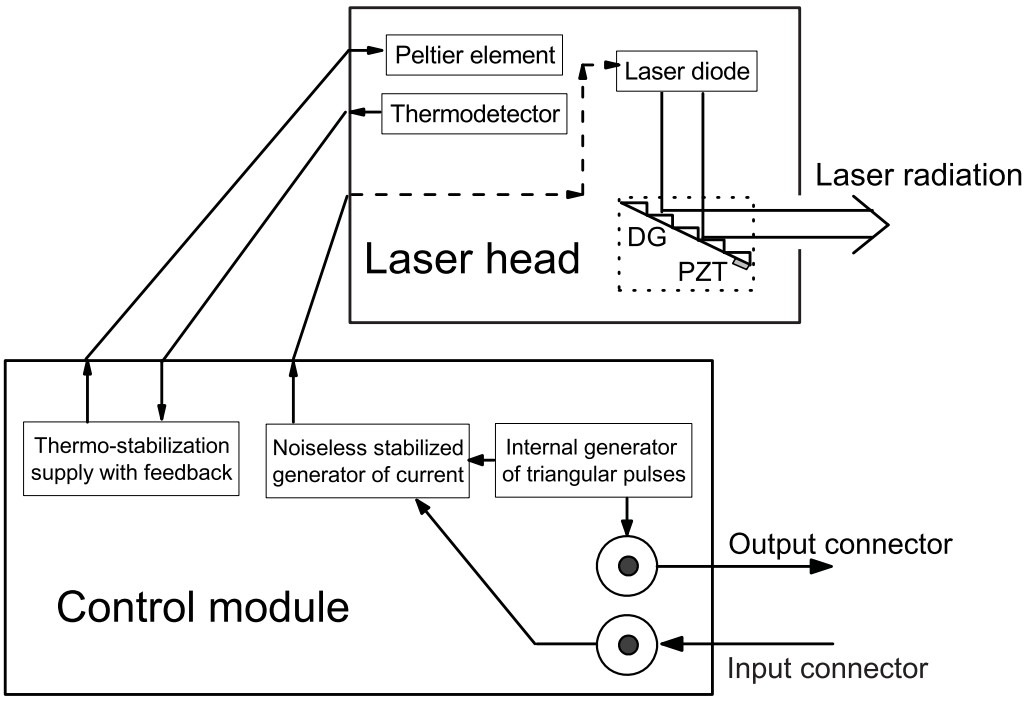

Figure 1.1: Block-scheme of control module and construction of external cavity.

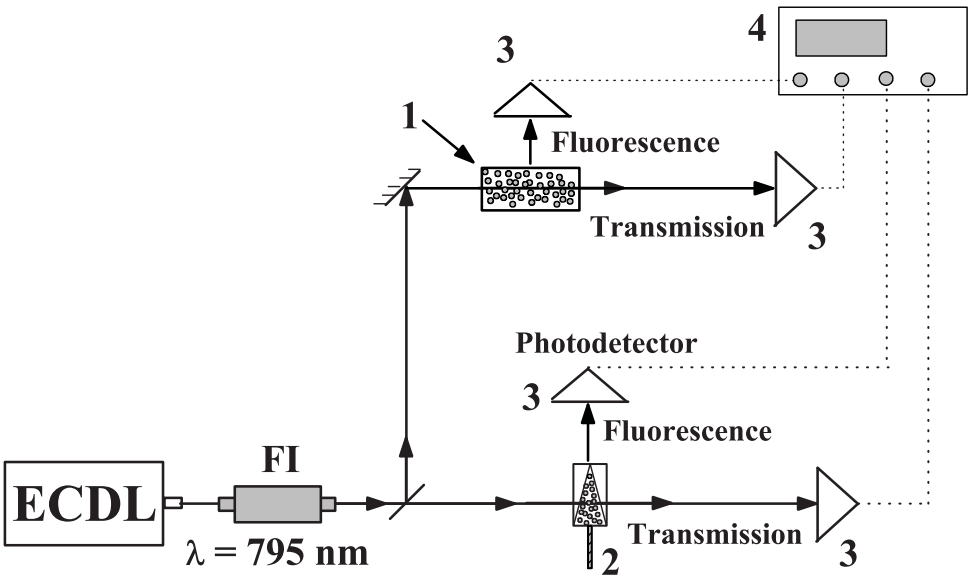

Figure 1.2: Experimental setup: ECDL-diode laser, FI-Faraday isolator, 1-ordinary cell with Rb ($L = 3$ cm), 2-nano-cell with Rb, 3-photodetector, 4-digital storage oscilloscope.

The common Littrow configuration contains a collimating lens and a diffraction grating as the end mirror. The first-order diffraction beam provides optical feedback to the laser diode chip, which has an anti-reflection coating on the side near end mirror.

Block-scheme of control module and construction of external cavity is represented on fig. 1.1. Stabilized noiseless current generator and thermo-stabilisation supply with feedback are the main parts of the control module.

DL parameters	**DL without external cavity**	**ECDL**
Emission wavelength	780 nm, 795 nm, 894 nm, 852 nm	780 nm, 795 nm, 894 nm, 852 nm
Spectral linewidth	$5 - 30$ MHz	$0.7 - 1$ MHz
Emission power	$10 - 80$ mW	$10 - 40$ mW
Divergence	~ 1 mrad	~ 1 mrad
Power supply parameters		
Injection maximal current	200 mA	200 mA
Current setting precision	0.1 mA	0.1 mA
Stabilization of current	± 0.03 mA	± 0.01 mA
Internal modulation	$10 - 3000$ Hz	$10 - 3000$ Hz
Current of modulation	$0 - 5$ mA	$0 - 4$ mA
External modulation	$0 - 100$ mA	$0 - 100$ mA
Temperature range	$+5 .. + 55$ °C	$+15 .. + 30$ °C
Precision of temperature measurement	0.1 °C	0.1 °C
Temperature setting precision	0.1 °C	0.1 °C
Temperature stabilization	0.03 °C	0.01 °C

Table 1.1: Technical characteristics of DLs

The emission wavelength can be tuned by rotating the diffraction grating. For this purpose diffraction grating (DG) is installed on a piezoelectrical (PZT) mount, which may rotate by changing the voltage applied on PZT chip.

Peltier element realizes the thermo-stabilization of the diode chip. In order to measure the diode chip temperature the chip is installed on a mount with a thermo-detector, which realizes a feedback with the control module.

The control module is equipped with input connector for the external modulation of the laser diode current. That allows to change the laser radiation wavelength (in case of low frequency modulation $\sim 0.1 - 10$ Hz) as well as frequency modulation (FM) (high frequency modulation $\sim 0.5 - 100$ kHz).

For synchronization with external devices, control module is also equipped with an output connector which passes train of triangular pulses from internal generator to external devices.

Main characteristics of diode lasers are represented in table 1.1. In our experiments we use ECDL producing a wavelength $\lambda = 780$ nm (D_2 line of Rb) and 794.7 nm (D_1 line of Rb) with tuning range $10 - 40$ GHz. For beam collimation a $2 - 4$ mm focal length lens is used. It results a divergence of 1 mrad of the outgoing beam.

b) Faraday isolator

In fact ECDL have big gain coefficient and it leads to high sensitivity of ECDL to feedback. It means that ECDL are very sensitive to reflections of the laser beam from optical elements of experimental setup. Strongest reflections appear when it is necessary to direct the laser beam perpendicularly to optical surfaces, for instance perpendicularly to the windows of a nano-cell filled with atomic vapours. In this case the nano-cell reflects $\sim 7\%$ of the incident beam intensity and back-reflected beam (feedback) causes non-stable regime of the laser process. In order to avoid the feedback of the laser radiation, a Faraday isolator (FI) is used. The principle of working of the FI is as follows: the laser beam is directed on a FI at first pass through a first Glan polarizer enlightened by a plane polarized laser radiation. After a first polarizer, the linearly polarized laser radiation passes through a magneto-active element and under the influence of the external magnetic field applied to the magneto-active element undergoes a rotation of the polarization plane of the laser radiation. The magnitude of the magnetic field applied to the magneto-active element is specially adjusted to rotate the plane of polarization of 45°. After the magneto-active element, the radiation passes through a second Glan polarizer which is rotated of 45° in respect with the first polarizer and transmits the laser radiation without losses. In this case the back reflected beam, after passing through a second polarizer and magneto-active element, will be rotated one more time of 45° and will not be passed through the first Glan polarizer due to perpendicular polarization of reflected beam in respect with the initial polarization. FI used in our experiments have return losses

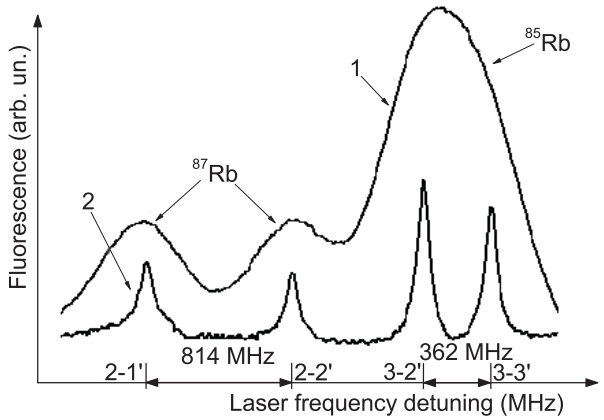

Figure 1.3: Fluorescence spectra for D_1 line, ^{85,87}Rb transitions (from left to right) ^{87}Rb, $F_g = 2 \to F_e = 1, 2$ and ^{85}Rb, $F_g = 3 \to F_e = 2, 3$ (see on fig.1.4) : (1) - spectrum obtained with ordinary cell $L = 3$ cm; (2) - spectrum obtained with nano-cell $L = \lambda/2$, in this case observed sevenfold narrowing of fluorescence spectrum.

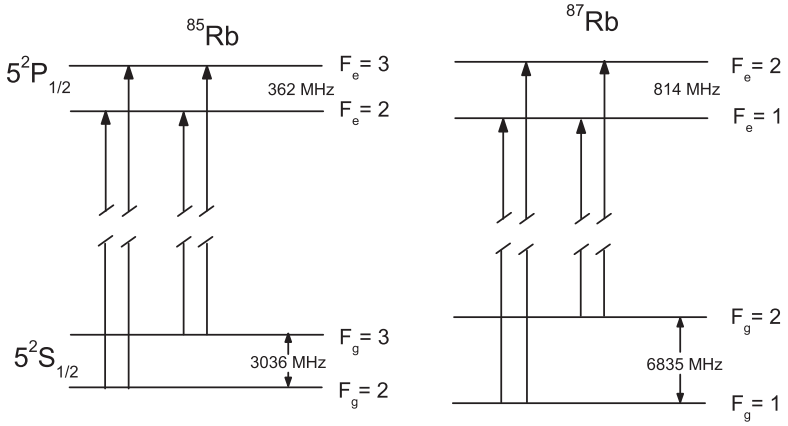

Figure 1.4: Simplified scheme of energy levels for D_1 line of $^{85,\ 87}$Rb atoms.

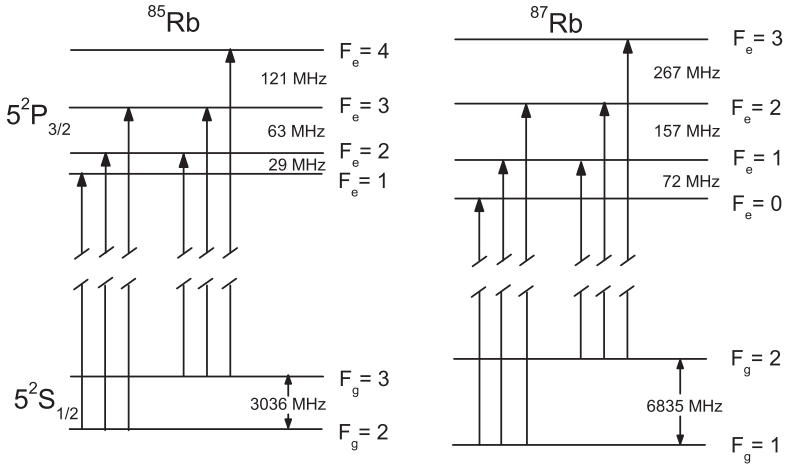

Figure 1.5: Simplified scheme of energy levels for D_2 line of $^{85,\ 87}$Rb atoms.

equal to 40 dB. It means that the reflected beam is 10^4 times attenuated. It is enough for stable work of ECDL.

c) Registration of laser radiation in the range $700 - 1000$ nm

In order to register signal of laser radiation absorption, fluorescence spectra, selective reflection, signal of probe radiation in saturated absorption spectroscopy and others, photo-detectors based on FD-24K photodiodes are used. These photodiodes have an aperture about 1 cm^2 (presence of a big aperture is important for the significant registration of weak fluorescence signals) and good sensitivity in the range $500 - 1100$ nm. To amplify the photodiode signal, an amplifier based on operational amplifier KR140UD8 is used. Experimental data are saved in a digital storage oscilloscope.

Our registration technique based on photo-detectors and digital oscilloscope was enough sensitive to register optical signals with power close to ~ 5 nW

d) Measurement of temperature

The temperature T_{SA} of cell's side-arm, which contains metal, determines the density of the atomic vapour of the alkali metals used in our experiments. To avoid condensation of atoms on optical windows of the cell, it is necessary to keep the temperature T_W of the windows $15 - 20$ °C higher than the temperature of the side-arm. It implies a permanent control of the temperature of the cell's windows and of the side-arm, thus we used a chromel-alumel thermocouple to measure and adjust the temperature. This thermocouple allows the measurement of the temperature up to 1000 °C, moreover it has very weak magnetic properties, which is important in the case of detection of magneto-optical effects especially with strong magnetic field of thousands gauss. An ordinary milli-voltmeter is used for measuring the voltage of the thermocouple: 0.01 mV corresponds to $T = 0.2$ °C.

1.2 Spectra of absorption and fluorescence of ordinary cell and comparison with nano-cell spectra

The simplest method of spectroscopy of atomic transitions by one laser is the formation of the spectra of transmission (or fluorescence (FL)) of atomic vapours, confined in cells of centimeter length [44]. In the case when a high resolution of frequency is not required, this simple method is convenient. On fig. 1.2 it is demonstrated an experimental scheme for registration of FL and transmission spectra in the cell of 3 cm length (1) and nano-cell (2) both filled with Rb, ECDL - cw DL, FI - Faraday insulator, (3)- photodetectors, (4)- four-channel digital oscillograph Tektronix TDS2014B. The thickness of nano-cell (with wedge-shaped gap) varied during the experiment by the means of its vertical shift.

On the upper curve (1) of fig. 1.3 it is demonstrated the FL spectrum ^{85,87}Rb, D_1 line from the cell of 3 cm length, obtained using ECDL with $\lambda = 794.7$ nm and $\gamma_L = 1$ MHz. The disadvantage of this method is that the atomic transitions are not resolved spectrally. This is because the width of an individual atomic transition described by a Gaussian function is Doppler-broadened and for $D_{1,2}$ lines of Rb atoms, this width is ~ 500 MHz [44].

The reason of the Doppler-broadening is the thermal movement of atoms inside the cell with different thermal velocities V_T (distribution of atomic velocities is described by Maxwell law) in different directions. As a result of the Doppler effect these atoms absorb shifted frequency ω in respect with the frequency ω_0 of atomic transition: $\omega = \omega_0 + \vec{k} \cdot \vec{V_T}$, where $\vec{k} = 2\pi\vec{n}/\lambda$, λ being the wavelength of the laser radiation, $\vec{n}$ denotes the unit vector in the direction of the laser radiation. It is obvious that if the frequency distance between the atomic levels of the hyperfine structure is less than the width of the Doppler-broadened spectrum of these transitions then they will be "hidden" under the Doppler outline overall. This happens for D_1 line of ^{85}Rb atoms (see diagram on fig. 1.4). As it is demonstrated on the upper curve (1) of fig. 1.3, even in case of such a big value of the hyperfine splitting, as 362 MHz, atomic transitions ^{85}Rb, $F_g = 3 \to F_e = 2, 3$ are"hidden" under the Doppler outline overall.

The lower curve (2) of fig. 1.3 shows the FL spectrum of the nano-cell with the thickness

$L = \lambda/2$ ($L = 397$ nm). The full width of the FL spectrum on the half-maximum (FWHM) is equal to ~ 70 MHz, that is a ~ 7-fold narrowing of the Doppler width. As it was earlier demonstrated in the reference [42], in case of small L (in the range $\lambda/2 - 3\lambda$) it is observed a strong narrowing of the FL spectral width, this width smoothly broaden while increasing L. It is important to mention that the amplitudes of the FL lines are close to the theoretically calculated amplitudes. So, for instance, the theoretical ratio of the amplitudes for the transitions ^{85}Rb, $F_g = 3 \to F_e = 2$ and $F_e = 3$ equals 1.25, and on fig. 1.3 it is 1.18 (that is 5% of inaccuracy). Note, that the behaviour of absorption (or transmission) linewidth, against to the thickness of nano-cell (unlike FL), has an oscillating character. For this experiment the laser intensity is $I_L \sim 10$ mW/cm^2 and the temperature of side-arm close to 110 °C. So, the FL spectrum of the nano-cell with thickness $L = \lambda/2$ can be a convenient method used in the sub-Doppler spectroscopy.

On fig. 1.6 it is demonstrated a transmission spectrum of ^{85,87}Rb D_1 line: the lower curve (1) is a spectrum from 3 cm cell, and the upper curve (2) of a $L = \lambda/2$ nano-cell ($L = 397$ nm).

The comparison of (1) and (2) demonstrates a strong narrowing of the spectrum in the case $L = \lambda/2$. As a rule, the FWHM for fluorescence spectrum is $1.5-1.8$ times more narrow, than for the transmission spectrum. It can be explained in the following way [42]: in the process of the FL spectra, atoms with slower velocities (with lower velocity V_z) are participating to the process (while more atoms may contribute to the transmission and absorption spectra), since the atoms should have enough time to absorb and radiate a photon before colliding with the walls of the nano-cell (the intensity of nonradiative transition after collision with wall tends to one) however, for the transmission and the absorption it is enough just to absorb a photon. Despite a little bit wider spectrum of the transmission in comparison with the FL spectrum, the transmission spectrum of the nano-cell with $L = \lambda/2$ can be used for the sub-Doppler spectroscopy as well.

In previous publications [36–42] it was demonstrated an uncommon behaviour of the transmission spectra depending on L/λ (in [45] it was demonstrated in the microwave

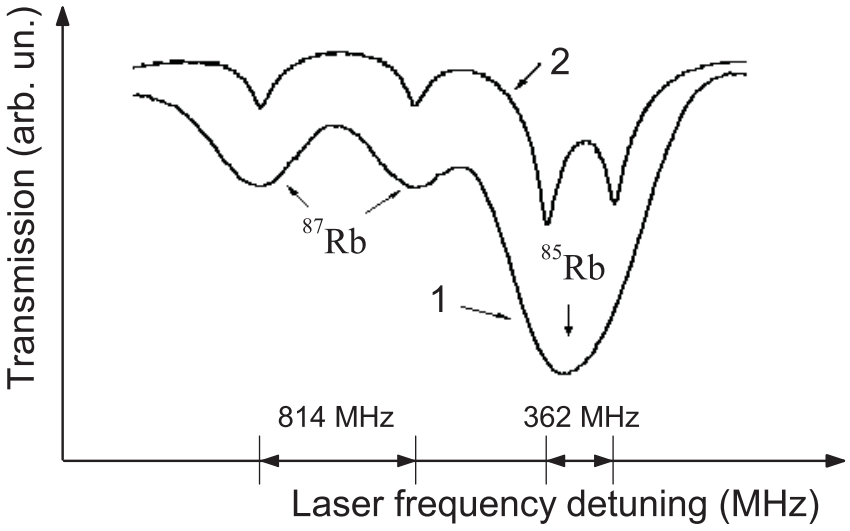

Figure 1.6: Transmission spectrum for D_1 line of $^{85,\ 87}$Rb atomic vapours: (1) ordinary cell, $L = 3$ cm; (2) nano-cell, $L = \lambda/2$.

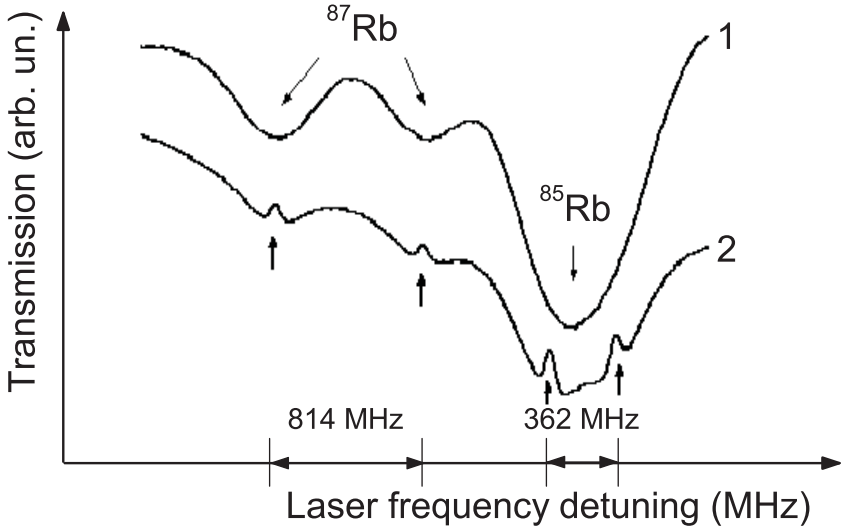

Figure 1.7: Transmission spectrum for D_1 line of $^{85,\ 87}$Rb atomic vapours: upper curve (1) ordinary cell, $L = 3$ cm; lower curve (2) nano-cell, $L = \lambda$.

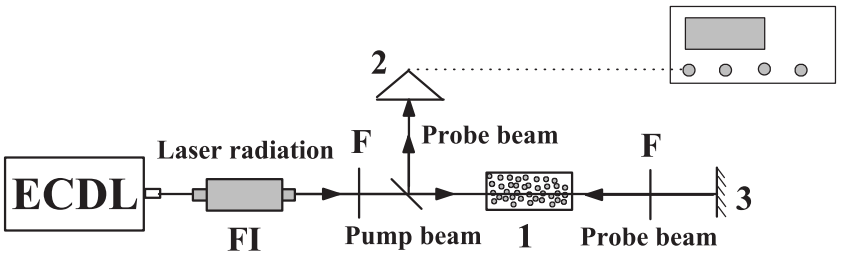

Figure 1.8: Experimental schema for the realization of SA spectroscopy. FI - Faraday Isolator, F - filter, 1 - sealed-off cell with Rb vapour, 2 - photodetector, 3 - mirror.

domain): the spectral width reach its minimum for $L = (2n + 1)\lambda/2$ (n is integer). This process is called Coherent Dike Narrowing (DCN). It is also shown in [46], that in the case $L = n\lambda$ the spectral width achieves its maximum, close to the Doppler width: that was called the collapse of DCN. In [47] the DCN effect and its collapse were investigated up to $L = 7\lambda/2$ for D_2 line of ^{85}Rb. However, for $L = n\lambda$ (n-integer) when the laser radiation intensity is equal to several mW/cm^2, the resonance of the decreased absorption appears on atomic transitions. On fig. 1.7 one can see the spectrum of transmission for the D_1 line of ^{85,87}Rb: the upper curve (1) for 3 cm length cell and the lower curve (2) for the nano-cell with $L = \lambda$ (794.7 nm). The reason of formation of these resonances is the Velocity Selective Optical Pumping: VSOP. VSOP resonances appear exactly on atomic transitions. The mechanism of formation of the VSOP resonances is the following: after the absorption of a photon, an atom passes from the ground state to one of the excited states (see fig. 1.4, 1.5). Then due to spontaneous relaxation, it may pass to another ground state. This is the usual process of optical pumping (OP). The OP leads to the reduction of the number of atoms in the initial ground state and, as a result, to the decreasing of the absorption signal. The efficiency η of the optical pumping is described by the following relation:

$$\eta \sim \frac{\Omega^2 \gamma_N t}{(\delta + \vec{k} \cdot \vec{V_T})^2 + \Gamma^2} \tag{1.1}$$

where Ω is the transition Rabi frequency, γ_N is natural linewidth, t is time of interaction with an exciting radiation, δ is the detuning from a resonance and Γ the sum of homogeneous and inhomogeneous broadenings. From the relation (1.1) it is obvious that increasing the time of interaction t, increases the efficiency η of the OP. For atoms flying perpendicularly to the laser beam the time of interaction is $t_D = D/V_T$ (D being diameter of laser beam), while for the atoms flying along the laser beam $t_L = L/V_T$. Since $D \sim 1$ mm and $L = \lambda$ (~ 800 nm for ^{85}Rb and ^{87}Rb), t_D is three order larger than t_L. For the atoms flying perpendicularly to the laser beam $\vec{k} \cdot \vec{V_T} = 0$ and relation (1.1) reaches its maximum for $\delta = 0$. Thus the VSOP resonances are located on the exact atomic transitions [46]. It is possible to assume

that VSOP peaks formed in the spectrum of transmission are convenient for the sub-Doppler spectroscopy.

1.3 Review of methods of forming sub-Doppler optical resonances

Introduction. It is well known, that in an ordinary cell (thickness in the range $1 - 100$ mm), which contains atomic vapours of metals, particularly vapours of alkali metals, it is impossible to resolve individual atomic transitions in absorption (transmission) and fluorescence spectra due to the Doppler-broadening [44]. The width of an individual Doppler-broadened atomic transition, having a Gaussian profile, at room temperature ($T = 27$ °C) for different alkali atoms achieves $400 - 1000$ MHz. The reason of the Doppler-broadening is the thermal motion of atoms with non-uniform velocities (Maxwell distribution) in all possible directions inside a cell. Due to the Doppler effect the atoms which move, absorb shifted frequency in respect to the atomic transition frequency: $\omega_{ab} = \omega_{tr} + \vec{k} \cdot \vec{V_T}$; where ω_{ab} is the absorbed photon frequency, ω_{tr} is the atomic transition frequency, V_T denotes the thermal velocity, $\vec{k} = 2\pi\vec{n}/\lambda$ is the wave vector, λ represents the wavelength of the laser radiation and $\vec{n}$ the unit vector in the direction of propagation of the laser radiation.

At room temperature, the Doppler-broadening of an individual atomic transition for Rb atomic vapours is close to ~ 500 MHz, while it reaches ~ 600 MHz near $100 - 120$ °C. This interval of temperature $100 - 120$ °C corresponds to the range of temperature used during the experiments with our nano-cells.

We may assume, that if the frequency distance between the atomic states of the hyperfine structure is less than the linewidth of the Doppler profile, it is impossible to resolve individual atomic transitions, and they will be hidden under the overall profile. On fig. 1.4 and fig. 1.5 the diagrams of the hyperfine structure of D_1 and D_2 lines of Rb atoms are demonstrated. It is obvious from the diagram, that the frequency distance between the atomic states of the hyperfine structure is less than 500 MHz (except D_1 line of ^{87}Rb, 814 MHz) and this leads to

the overlapping of the individual transition's profiles in absorption and fluorescence spectra.

In the present time, there are several methods, which allows one to resolve transitions between states of the hyperfine structure (to realize sub-Doppler spectroscopy). The most used methods are: saturated absorption, selective reflection from the border of the cell's windows-atomic vapour; and also the technique of atomic beams [44].

1.3.1 Saturated absorption spectroscopy

The method of saturated absorption (SA) (or spectroscopy of saturation) is one of the most famous and widely used methods of the sub-Doppler spectroscopy [44, 48–60]. It is based on the selective saturation of a non-uniformly broadened atomic transition caused by a laser beam optical pumping. A common scheme of SA realization is represented on fig. 1.8. The laser beam, after passing through a filter (this filter is used in order to change laser beam intensity), used as the pump beam (intensity is now ~ 10 mW/cm^3), passes through the cell 1 and is reflected back from mirror 3 (100% of reflection). Reflected, counterpropagating weak probe beam, attenuated again in a filter, overlaps with the pump beam in the cell 1. Due to the Doppler effect, only atoms which have z-component of velocity in the range of $V_z \pm dV_z = (\omega_{tr} - \omega_L \pm d\omega)/k$, will interact with the laser radiation of frequency ω_L, ω_{tr} is the transition frequency, $d\omega = \delta\omega_N + \Delta\omega_L$ is the sum of atomic state natural width $\delta\omega_N$ and laser linewidth $\Delta\omega_L$, k denotes the wave vector. The absorption of the radiation leads to a change of the population $n_i(V_z)dV_z$ of the upper and lower states for atoms with thermal velocity in the range of $V_z \pm dVz$. Due to this change, the population of the upper state increases and for the lower state – decreases. This kind of population transfer leads to a decrease of the absorption coefficient for the group of atoms which have the velocity V_z.

For the investigation of this group of atoms one should use a counterpropagating probe beam, this probe beam should interact with this group of atoms simultaneously with the pump beam. The Doppler effect depends of the direction of the motion of the atoms and it is obvious that the group of atoms, which will interact simultaneously with the both beams, should have z-component of the velocity $V_z = 0$.

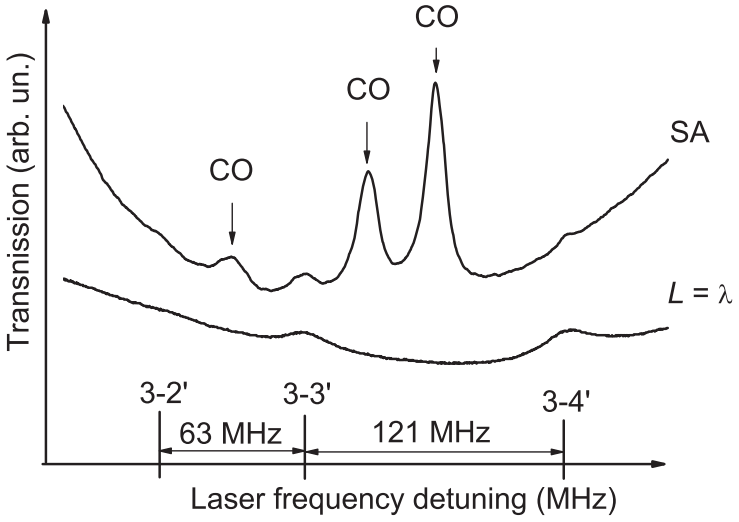

Figure 1.9: Spectra of ^{85}Rb $F_g = 3 \to F_e = 2, 3, 4$ D_2 line: upper curve is SA spectra and lower curve - transmission spectra of nano-cell with $L = \lambda$.

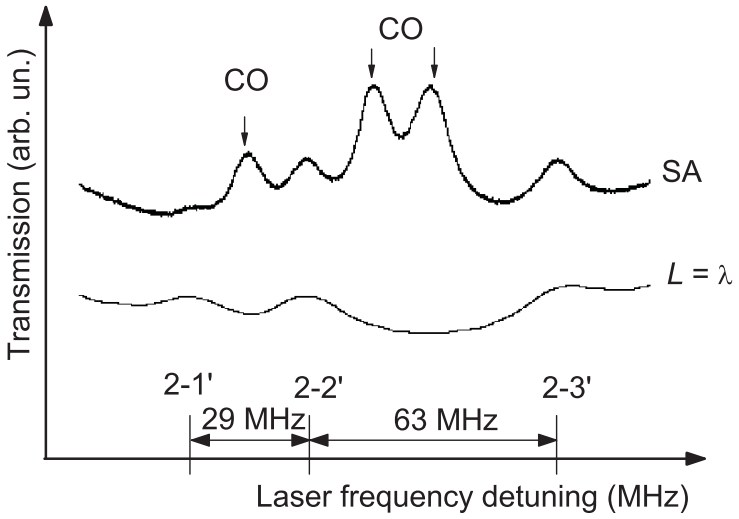

Figure 1.10: Spectra of ^{85}Rb $F_g = 3 \to F_e = 2, 3, 4$, D_2 line: upper curve is SA spectra and lower curve - transmission spectra of nano-cell with $L = \lambda$.

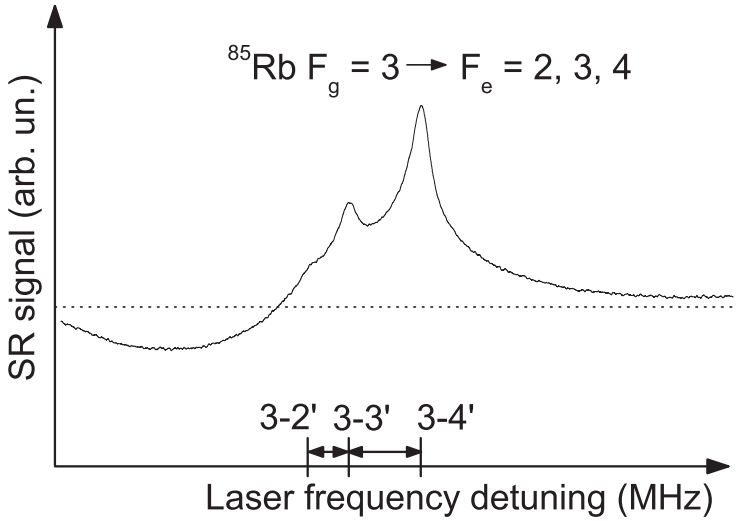

Figure 1.11: Selective reflection spectrum of ^{85}Rb $F_g = 3 \to F_e = 2, 3, 4$, D_2 line.

On an optical spectrum, exactly on an atomic transition, a peak of decreased absorption (Lamb depth) will appear. Also on the spectra of SA (fig. 1.9) so-called "Cross-over" resonances (CO) appear (the peak of decreased absorption is located exactly in the middle of two atomic transitions). Peaks in SA have uniformly broadened linewidth [44]. It is possible to obtain peaks in SA with linewidth close to the natural width (for Rb, $\gamma_N = 6$ MHz) by changing the experimental parameters.

On fig. 1.9 it is demonstrated a comparison of the spectrum of SA for D_2 ^{85}Rb transitions $F_g = 3 \to F_e = 2, 3, 4$ and the spectrum obtained with the use of the nano-cell in the region $L = \lambda$. In the experiment we used an ECDL laser with $\lambda = 780$ nm and $\gamma_L = 1$ MHz. The SA spectrum is obtained with an ordinary 8 cm length cell, the power of the pump beam being $P_P = 0.4$ mW and the probe beam $P_{Pr} = 0.1$ mW.

To be more precise we should mention, that VSOP resonances, which are formed by a single passing in the transmission spectrum of the nano-cell at $L = \lambda$, (fig. 1.10) have wider linewidth ($\sim 1,5$ times) than in the SA spectrum. However, for SA spectroscopy one should realize the scheme of two counterpropagating beams and in the case of the nano-cell usage the single passage scheme is used. Also for the realization of the SA spectroscopy it is necessary to have an intensity of laser radiation one order higher than in the case of nano-cell.

The SA has the following disadvantages: i) the ratio of the peaks amplitudes doesn't correspond to the ratio of the transition intensities due to the non-linear nature of SA. According to the theoretical calculations and experimental measurements the intensity of the transition $F_g = 3 \to F_e = 4$ is 2 times larger in comparison with the intensity $F_g = 3 \to F_e = 3$ (see fig. 1.9 lower curve), however in the SA spectrum its amplitude is 2 times less. ii) the presence of CO resonances (the amplitudes of CO resonances in fact, as a rule, are larger than the amplitudes of decreased absorption peaks) makes spectra of SA more complicated. Especially in case when the frequency distance between the hyperfine states is not large (CO and VSOP peaks partially overlapped) the CO peaks may change the position of the less intense VSOP peaks. This phenomena is demonstrated on fig. 1.10, where is shown the spectrum of SA for D_2 line of ^{85}Rb transitions $F_g = 2 \to F_e = 1, 2, 3$ and the spectrum

of the nano-cell with $L = \lambda$. The frequency distances between upper states are 63 MHz and 29 MHz and due to this reason distances between CO and VSOP peaks are less.

It result a non-convenient use of the SA spectroscopy.In case of the nano-cell, CO peaks are absent and this makes the use of the nano-cell spectra more convenient.

1.3.2 Method of selective reflection

In the method of selective reflection (SR) an emission is registered, reflected from the bound of the cell window - atomic vapour (dioptre window - vapour).

At the turn of the 70s it was demonstrated that the spectrum of the emission, formed during the reflection from this bound, has a sub-Doppler feature [61–69]. This is because the most major contribution in the spectrum of SR is made by atoms, flying parallelly to the windows of the cell and the atoms of low velocity. The determinative contribution of atoms flying parallelly to the windows of the cell exhibits in the following: the extension of the angle between normal to the windows of the cell and the direction of the laser radiation drastically increases the linewidth of the spectrum SR. The explanation of this phenomenon is the following: during the extension of the angle, a projection of a thermal velocity different from zero appears in the direction of the laser radiation $V_z = V_T \sin\theta$ for the atoms flying parallelly to the windows of the cell and this provides additional Doppler-broadening of SR spectrum. Therefore in order to obtain minimum width of a SR spectrum it is necessary to provide an angle of incidence close to the normal. The exact expression of the coefficient of reflection R for selective reflection is demonstrated in the work [69]. Let us mention that in order to estimate R, the well-known Fresnel formula can be used

$$R = \left(\frac{n_W - n_a}{n_W + n_a}\right)^2, \tag{1.2}$$

where n_W is the refraction index of cell's window (as a rule, a sapphire or a garnet window (resp.) is used, for which $n_W = 1.76$ and 1.82 in case of wavelength 780 nm (resp.)), and n_a is the refraction index of Rb atoms nearby atomic transition (it is well-known that the value n_a

depends on the density of vapours of Rb, with $n_a > 1$, when the frequency of the laser is less than the frequency of the atomic transition, and $n_a < 1$, when the frequency of the laser is more than the frequency of transition) [44]. Fig. 1.11 shows a spectrum of selective reflection from the bound garnet window - Rb atomic vapour for ^{85}Rb $F_g = 3 \rightarrow F_e = 2, 3, 4$, D_2 line. The horizontal dotted line indicates the value of reflection from the bound garnet window - Rb atomic vapours far from atomic resonance, when $n_a = 1$. In this case the reflection achieves $\sim 8.5\%$, meanwhile nearby the atomic transition peak reflection achieves $\sim 8.6\%$.

As it is demonstrated on the figure, the spectral width of the peaks in SR is approximately 1.5 times less in comparison with the similar peaks, obtained by using the nano-cell (see fig. 1.9). The comparison is taken at the same temperature and the same laser linewidth. But the disadvantages of the SR method are wide spectral wings of the line profile, which are spread for several hundreds of MHz (the reason is that the value n_a during the deviation from the resonance goes down slowly [44]). Besides, the main disadvantage of the SR method is the frequency shift of its peaks (at $10 - 15$ MHz) in respect with the frequencies of atomic transitions. The reasons of this shift are the followings: a) the index of refraction n_a for atoms is reaching its maximum value not in the exact atomic resonance, but in the frequency of less resonance; b) the interaction of an atom with the cell windows also leads to a shift of energy levels, and therefore to the corresponding transitions [67].

1.3.3 Utilization of atomic beam

In order to get an atomic beam the following construction is used. A heating stove inside of which some quantity of alkali metal is placed, is put in a metal pipe of $2 - 3$ meters length (as a rule made from stainless steel). The stove is heated up to $500 - 600$ °C in order to provide high density of atomic vapour of metals. Later, diaphragms with small holes (~ 1 mm diameter) are placed along the metal pipe in order to select only those atoms which propagate along the axis of the metal pipe. Vacuum inside the metallic chamber must be high enough (at the level $\sim 10^{-7}$ torr) to provide free running length for the atoms enough

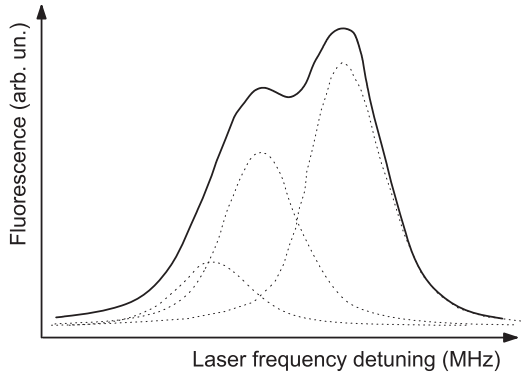

Figure 1.12: Spectrum of resonant fluorescence ^{85}Rb $F_g = 3 \rightarrow F_e = 2, 3, 4$, D_2 line obtained with atomic beam technique [70].

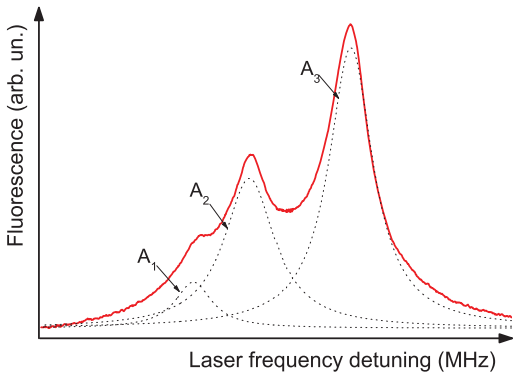

Figure 1.13: Spectrum of resonant fluorescence ^{85}Rb $F_g = 3 \rightarrow F_e = 2, 3, 4$, D_2 line obtained with a nano-cell.

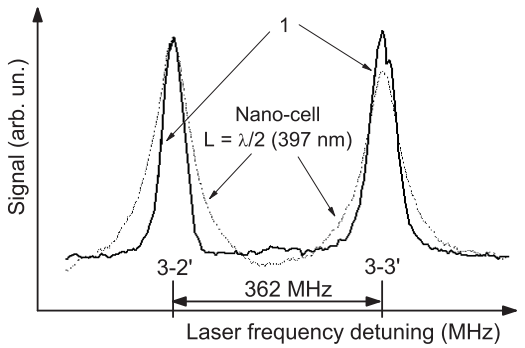

Figure 1.14: Spectrum ^{85}Rb $F_g = 3 \rightarrow F_e = 2, 3$, D_1 line: 1 - spectrum obtained with technique developed in [83]; dashed curve - fluorescence spectrum obtained with a nano-cell $L = \lambda/2$.

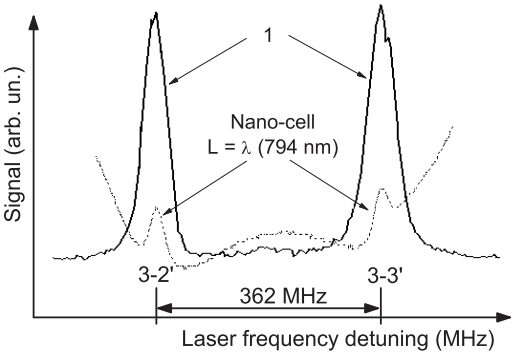

Figure 1.15: Spectrum ^{85}Rb $F_g = 3 \rightarrow F_e = 2, 3$, D_1 line: 1 - spectrum obtained with technique developed in [83]; dashed curve - transmission spectrum obtained with a nano-cell $L = \lambda$.

to fly till the end of the pipe without any collision (the length of free path of an atom is ~ 40 μm/torr). The density of the atoms flying till the end of the pipe is $\sim 10^{-8}$ part of the density of the atoms, that the stove provides ($\sim 10^{18}$ at/cm^3) and thus leads to a small value $\sim 10^{10}$ at/cm^3.

Taking into account that the diameter of a laser beam, directed perpendicularly to the atomic beam (in order to avoid Doppler-broadening), is equal to ~ 1 mm (the atomic beam is of the same size), thus the quantity of atoms in the zone of interaction is of order 10^7, which is a low value to registrate a spectra. Besides, for the insertion of a laser radiation into a metallic pipe, vacuum-tight optical windows should be set. On fig. 1.12 is shown the spectrum of the resonant fluorescence of ^{85}Rb, D_2, $F_g = 3 \to F_e = 2, 3, 4$ transitions obtained with the method of the atomic beam (from work [70]), and on fig. 1.13, the fluorescence spectrum of the same transitions, obtained using a nano-cell. In order to determine the amplitudes and the spectral widths of certain atomic transitions among the levels of the hyperfine structure we made "fitting" of these spectra (dotted lines). The models of curves used to reproduce the three transitions have been supposed to be Gaussian functions. One should note, that the set of parameters that determine the shape of these Gaussian functions is not unique, mainly the widths of three Gaussian curves are defined within a range of validity to reproduce the red observed spectrum of fig. 1.13.

As it is obvious from the comparisons of the spectra of fig. 1.12 and fig. 1.13, a better spectral resolution is achieved using the nano-cell. Besides, in case of utilization of nano-cell, relations of amplitudes in the spectrum of resonant fluorescence for transitions between the levels of the hyperfine structure are staying linear (it means that the amplitudes relate to intensities of transitions). In table 1.2 we give the ratio of the amplitudes in the spectra of resonant fluorescence, obtained from fig. 1.12 and fig. 1.13 with the theoretical values for comparison. The relations of the amplitudes in the spectrum of the resonant fluorescence of nano-cell exhibit a better accordance with the theory. Let us mention that the atomic beam with linear size of metal pipe with $L > 3$ m, is used nowadays, which reduces angular divergence and, as a result, allows one to get natural linewidth of the Rb D_2 line (~ 6 MHz).

Transitions	Theory	Atomic beam	Nano-cell
A_2/A_1	3,51	2,88	3,48
A_3/A_2	2,31	1,5	1,87

Table 1.2: Comparison of experimental results obtained with atomic beam [70] and nano-cell for ratio of fluorescence amplitudes of hyperfine transitions $F_g = 3 \rightarrow F_e = 2, 3, 4$ D_2 line with theoretical calculation.

In spite of good spectral resolution, the disadvantages of the technique of the atomic beam are: a) the high technical complication of making vacuum-tight system with optical windows and with a high vacuum inside (the vacuum pumping process must be uninterrupted); b) the frequent opening of the metal pipe in order to clean the metal which condensed on a inner surface and in order to put new quantities of metal, because the metal heated up to high temperature evaporates quickly; c) technical complication of registration of the absorption and fluorescence spectra as explained here before.

1.3.4 Method of coherent population trapping

Let us also mention a recently developed method: the method of coherent population trapping (CPT). This method allows to obtain resonance lines, with widths extremely less than the natural ones (recorded value $\sim$ 50 Hz while natural widths are close to 5 MHz) [55,71–76]. To realize the CPT experiment, a convenient way is to use a laser radiation containing two close frequencies ω_{L1} and ω_{L2}, which ensures the phase coherence of these two frequencies, in order to realize the bichromatic pumping interacting with Λ-system. The difference of frequencies of the two shoulder transitions of the Λ-system should be equal to the difference of frequencies $\omega_{L1} - \omega_{L2}$ itself equals to the difference of ground states hyperfine splitting frequencies (transition between the ground states is assumed to be forbidden in a first approximation). Then, when maintaining the frequency of the first radiation in an exact resonance and tuning the frequency of the second one, thus when the difference of the two laser frequencies coincides with the frequency of the hyperfine splitting of the ground states, the transmission spectrum of the first radiation exhibits a "peak" of increased transmission with a spectral width extremely less than the natural width. The bichromatic laser radiation must fulfilled

the strict condition that the two waves must be phase correlated (moreover in most cases these two radiations are formed from one initial beam). In spite of the high resolution of the CPT method, its realization is technically complicated as well as to obtain a well-collimated atomic beam.

1.3.5 Sub-Doppler spectroscopy using cells with thickness $0.5 - 1$ mm

In [77–83] the sub-Doppler spectroscopy method is used with cells of thickness $0.5 - 1$ mm. Here is reused the same idea on which was based the sub-Doppler spectroscopy with nano-cells: fast atoms with V_z along the laser radiation undergo a less influence of the OP (as a result of the collision with windows) in comparison with the atoms flying parallel to the cell windows, which form VSOP. But in order to obtain narrow VSOP resonances (~ 50 MHz), supplementary techniques [77–79,81–83] are necessary. Particularly, a time delay between the saturating and the probe radiations is included, however, VSOP formed with the nano-cell, is spectrally $2-3$ times more narrow and more simple to realize technically. On fig. 1.14, curve (1), the VSOP resonances are demonstrated, explained in [83], for D_1 line of ^{85}Rb transitions $F_g = 3 \to F_e = 2, 3$, with a cell of lengths $L = 1$ mm. The dotted curve - FL spectrum, is obtained with the nano-cell $L = \lambda/2$ (see also fig. 1.3). Note that although VSOP on the curve (1) have less width ~ 50 MHz, the FL spectrum (~ 70 MHz) describes correctly the intensities of the transitions $F_g = 3 \to F_e = 2$ $F_g = 3 \to F_e = 3$, for which the theoretical ratio equals 1.25, for the FL it equals 1.2, and 1 for the curve (1).

On fig. 1.15 the curve (1) - is the same as the one on fig. 1.14, the dotted curve demonstrates the spectrum of transmission, obtained with the nano-cell, $L = \lambda$ (see also fig. 1.7). In this case the width of VSOP resonances is less than 20 MHz, that is two times more narrow than for the curve (1), and the ratio of amplitudes is ~ 1.25. So, the spectroscopy based on the nano-cell with $L = \lambda$, demonstrates a better spectral resolution than the one based on the cells with $L \sim 1$ mm [82].

1.4 Constructions of thin cells and nano-cells, containing atomic vapours of alkali metals

1.4.1 Construction of thin cells containing atomic vapours (of thickness from a few to hundreds of μm)

The description of thin cells (the thickness of tens of μm) is shown on fig. 1.16. Rectangular, well polished plates are chosen as cell windows (1). The sizes of the plates are 20×30 mm of thickness 3 mm. The plates are made from a technical crystalline sapphire (Al_2O_3), which is chemically stable to aggressive hot Rb vapours, or from the crystal of a garnet ($Y_3Al_5O_{12}$), which is also chemically stable to Rb vapours [84, 85]. Since a crystalline sapphire has a natural birefringence, the windows of the cells are prepared in such a way that the c-axis is perpendicular to the surface of the window. In this case, if the laser radiation is oriented perpendicularly to the window, the birefringence significantly decreases.

In the study of the magneto-optical processes a great advantage of using garnet is that the birefringence is absent. The plates of a sapphire are transparent in the range $0.2 - 6$ μm, and for a garnet in the range $0.3 - 5$ μm. A sapphire or garnet plate (1) is made with a small wedge $\sim$ 10 angular minutes in order to avoid overlapping of the reflected radiation from the surfaces of the plate. Since in the experiments it is important to have different thickness L of atomic metal vapours, the gap between the windows of cells, as a rule, is made with variable thickness (that is wedge-shape). For this purpose at the top and the bottom part of the cell, between the windows, thin strips of titanium are placed (noted (2) on fig. 1.16). Note, that Ti is chemically stable to hot vapours of Rb and Cs. Further, for example, if a thin rectangular Ti strip of 0.5 mm width, 3 mm length and 50 μm thickness is placed at the top and a thin strip of 90 μm at the bottom, then after packing of the cell, the thickness L of a vapour column in the vertical plane (top-down) will vary from 50 to 90 μm. If the direction of the laser beam is fixed and the cell is placed in the vertical plane, then the laser beam will interact with atomic vapours of column thickness in the range $50 - 90$ μm.

It is important to note that within a beam of diameter $D_L = 0.5$ mm, the thickness of the

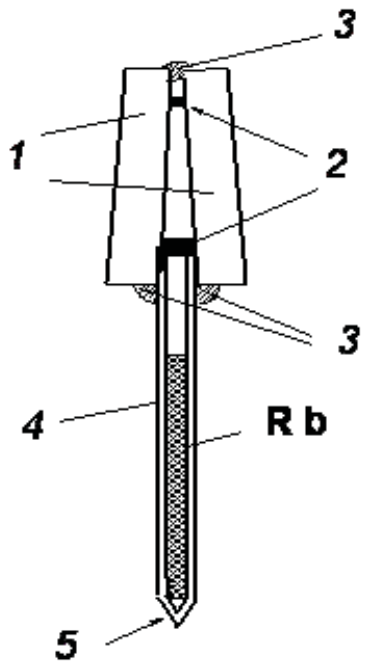

Figure 1.16: Description of thin cell (nano-cell): 1 - sapphire or garnet plates, 2 - titanium or platinum strips, 3 - glue, 4 - sapphire tube, 5 - glass side-arm.

(a) The thin cell with Rb.

(b) The nano-cell with Rb.

Figure 1.17: The photograph of thin cell and nano-cell: (a) thin cell, thickness L varying in range from 50 to 90 μm; (b) nano-cell with thickness L varying in range from 50 nm to 2 μm.

vapour column changes very slightly (5%). Further at the bottom of the windows a 2 mm diameter hole is drilled, where a thin crystal sapphire tube with an external diameter 2 mm and length 50 mm is placed (4). Then the whole construction is glued into a package (the glue spots are shown on fig. 1.16 (3)) in a vacuum chamber [45]. After the glueing a small glass side-arm is soldered to the sapphire tube (5). The further filling of Rb is done with a glass vacuum post as it is made for glass cells. The quantity of metallic Rb is chosen so that the sapphire tube with an inner diameter of 1 mm is almost completely filled (see fig. 1.17(a)). As it was demonstrated in [85], the density of Rb vapour is determined by the temperature T of the upper limit of the metallic Rb column in the sapphire tube (consequently a thermocouple is soldered to side-arm, so its tip has a good thermal contact with the upper limit of the column, see. fig. 1.17(b)).

In case of the corresponding construction of the heater, it is possible to obtain the following marginal temperature regime: T on the upper limit of the metallic Rb column ~ 500 °C and the temperature T of the glass side-arm (which is outside of the heater) ~ 80 °C at which a chemical reaction of Rb with a glass is negligible (a chemical reaction of Rb with a glass becomes significant at $T \sim 150 - 200$ °C). Concerning the reaction of Rb with sapphire, our experiments show that the reaction is absent up to temperatures $T \sim 700$ °C. Before filling the cell with Rb, it is connected to the vacuum post and pumped out during 4 hours when heated up to $T \sim 400$ °C. Due to the small thickness between the cell windows, it is complicated to remove gases and other impurities absorbed by surfaces of the cell windows. Therefore careful and long pumping out of thin cell (as well as nano-cell) at high temperatures is important.

The most complicated and important problem is to remove water completely from surface of sapphire or garnet. Note, that in order to get a cell which will have thicknesses of Rb atomic vapour L of several hundreds μm, one should put Ti strip (which works like spacer between the cell windows) thicker of thickness several hundreds μm. It means that the considered construction of the cell is universal for obtaining of thicknesses L in range from 5 μm to 1 mm.

1.4.2 Construction of nano-cells containing atomic vapours

The construction of nano-cells (the thickness of an atomic column is varies from 20 nm to several hundreds of micron) is similar with the one demonstrated on fig. 1.16 and considered in detail in [36]. In this case rectangular, smoothly polished sapphire or garnet plates, with the following sizes: width - 20 mm, height - 30 mm and thickness - 3 mm may be chosen as cell windows. The degree of finishing of a garnet polishing must be very high (more than $\lambda/10$). In order to form a nanometric gap between the cell windows, in the bottom side of the windows, by vacuum deposition, a thin strip (width is 1 mm, length is several mm and thickness - about $1-2$ μm) of sapphire (Al_2O_3) is created.

In case of particular problems, it was obligatory to use windows with a small thickness about 0.7 mm. In those cases after the cell filling and sealing-off under the pressure of the external atmosphere, the windows were pressed to each other, particularly in the region where the stripe are absent (top of plates), decreasing the gap between the cell windows up to $20-30$ nm. In case when the plates of ~ 0.7 mm were used, to increase plates thicknesses in the bottom part, little sapphire or garnet blocks were glued, which is well seen on fig.1.17(b). Inside is put and glued the thin sapphire pipe with the external diameter $\sim$ 2 mm and $\sim$ 50 mm length. For this purpose, a hole was drilled in the bottom side of the cell (where the supplementary sapphire blocks were glued) with a diameter of $\sim$ 2 mm. Further the all construction was gathered and glued in the vacuum chamber [45].

It is important to note, that since the distances between cell windows are small, a more careful and longer pumping ($\sim$ 8 hours) at high temperatures ($\sim$ 400 °C) is necessary. On fig. 1.17(b) is given a photograph of the nano-cell with a wage-shape gap between the windows and L in the range 50 nm - 2 μm. We would like to pay attention that on this photograph, an interferometric pattern is observed, which appears as a result of the reflection of the sunlight from the internal surfaces of the nano-cell windows. This is because the gap between the windows is of the wavelength λ of the sunlight. Note that the interferometric pattern is observed up to thicknesses about $2-2.5$ μm. On fig. 1.17(b) a thermocouple can also be

seen. A thermocouple is fixed so that its tip has a good thermal contact with the upper limit of the metallic Rb column inside the sapphire pipe. In order to increase the thermal contact, the tip of the thermocouple is tied to the sapphire pipe by a glass fibber.

1.4.3 Construction of combined, multi-region cells: ordinary cell interconnected with nano-cell

The description of combined, multi-region cells (MRC) is seen on fig. 1.18. MRC consists of two interconnected cells and a side-arm containing the studied alkali metal [1]. The nano-cell region (shown in the upper part of fig. 1.18) has a similar framework as the one demonstrated on fig. 1.16 previously considered. Rectangular, smoothly polished sapphire plates, with 20 mm $\times$ 30 mm $\times$ 0.7 mm nano-cell windows are chosen. Again, the degree of finishing of sapphire polishing must be very high (more than $\lambda/10$). In order to form a nanometric gap between the cell windows, in the bottom side of the windows by vacuum deposition, thin strip (width is 1 mm, length is several mm and thickness - about $1-2$ μm) of sapphire (Al_2O_3) is created. In order to increase the plates thicknesses in the bottom part of the windows, little sapphire blocks were glued, which is well seen on fig. 1.18. Further, it was necessary to fit the thin sapphire pipe in the cell and to glue it. For this purpose a hole was drilled in the bottom side of the cell (where supplementary sapphire blocks were glued) with diameter of $\sim$ 2 mm, then the thin sapphire pipe with an external diameter $\sim$ 2 mm and $\sim$ 20 mm length was fitted in the cell and the all construction was gathered and glued in the vacuum chamber [45]. Separately an ordinary cell was constructed (shown in the lower part of fig. 1.18). Two sapphire windows of one centimeter diameter were glued to one centimeter sapphire tube (the body of the ordinary cell). In order to glue two sapphire pipes in the middle of the sapphire tube on the sides, $\sim$ 2 mm diameter holes along the same direction were drilled. Then this construction was glued (interconnected) to the sapphire pipe connected with the nano-cell. The 1-cm long cell terminates with a sapphire side-arm containing metallic Rb.

Before filling the cell with Rb, it is connected to the vacuum post and pumped out

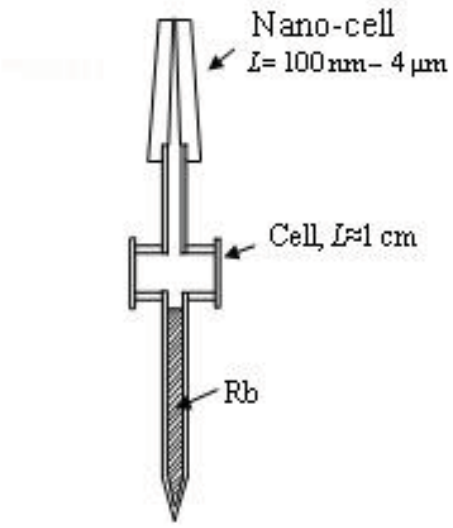

Figure 1.18: Scheme of a multi-region cell. Upper part is the nano-cell and lower part is the ordinary 1-cm cell.

Figure 1.19: Photograph of a multi-region cell.

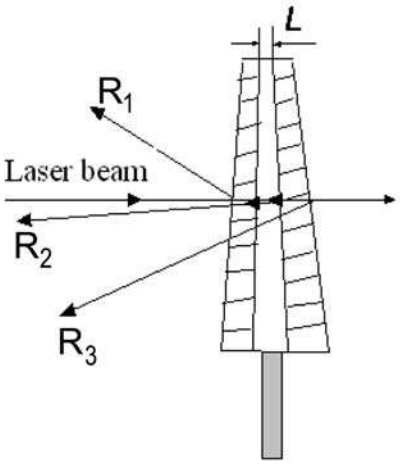

Figure 1.20: Configuration of reflections from nano-cell: R_1 - reflection from first surface, R_2 - reflection from inner gap (interferometric pattern), R_3 - reflection from backside surface.

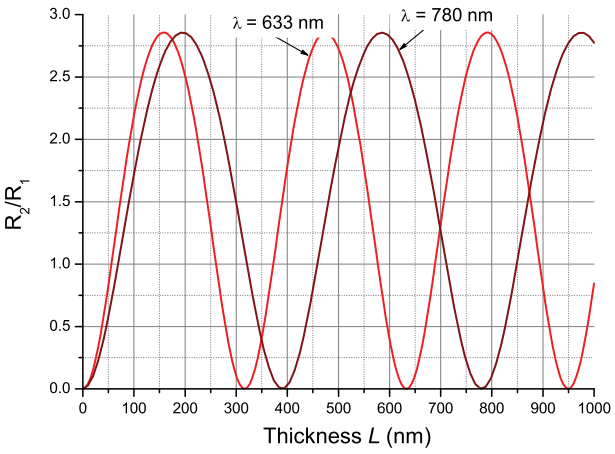

Figure 1.21: Variation R_2/R_1 as function of L for $\lambda = 633$ nm and $\lambda = 780$ nm.

during 8 hours when heated up to $T \sim 400$ °C in order to remove gases and other impurities absorbed by the surfaces of the cell windows. Further, in the system of the vacuum post, a certain quantity of buffer gas, corresponding to the partial pressure which is necessary for the experiment was let inside exactly before sealing-off.

Fig. 1.19 shows a photograph of MRC with a wage-shape nano-cell in the upper part of L varying in the range 100 nm - 4 μm and a ordinary 1-cm long cell in the lower part. As before, on the photograph it is observed an interferometric pattern.

On fig. 1.19 it is seen a cell holder containing thermocouple as well. A thermocouple is fixed so that its tip has a good thermal contact with the upper limit of the metallic Rb column inside the sapphire pipe. As already explained, in order to increase the thermal contact, a tip of the thermocouple is tied to the sapphire pipe by a glass fibber.

1.5 Determination of the thickness of a nano-cell using a laser beam

The method is based on the interferometry of reflected laser beams from two internal surfaces of the cell. Since the cell windows form a wage, by directing the laser radiation perpendicularly to the cell, one gets three reflections, demonstrated on fig. 1.20: R_1 - reflection from the first (external) surface, R_2 - reflection from the inner gap, which is a interferometric pattern of reflections from the two internal surfaces and, as a result, contains information about the thickness of the gap; R_3 - reflection from backside surface. A nano-cell can be considered as low-Q Fabry-Perot interferometer [39]. Because of this, by measuring the ratio of the intensities I_{R_2}/I_{R_1} for a certain λ, it is possible to determine the thickness L using the following relation for a Fabry-Perot interferometer [46]:

$$\frac{I_{R_2}}{I_{R_1}} = \frac{(1-R)^2}{R} \cdot \frac{F sin^2(\varphi/2)}{1 + F sin^2(\varphi/2)} \tag{1.3}$$

where R is the cell windows reflection coefficient, $F = 4R/(1-R)^2$ and $\varphi = 2\pi\delta/\lambda = 2\pi\ 2L\ cos\alpha/\lambda = 4\pi L/\lambda$ (α is practically ~ 0). From (1.3) it follows: the maximum of the

reflection is achieved for $\varphi/2 = (2k+1)\pi/2$ it means that $L = (2k+1)\lambda/4$ and the minimum of the reflection (i.e. $R_2/R_1 = 0$) is obtained for $\varphi/2 = \pi k/2$ that is for $L = k\lambda/2$, where k is an integer. In case of usage of garnet plates as nano-cell windows with refraction coefficient $n = 1.82$ (for $\lambda = 780$ nm), $R = [(n-1)/(n+1)]^2 = 0.084$ (i.e. 8.4%), $F = 0.4$ and ratio reaches to its maximum: $R_2/R_1 = 2.85$ (maximum for thicknesses $L = (2k+1)\lambda/4$). Hence, the maximal value of the reflection coefficient from the inner gar (R_2) achieves $R_2(max) = 2.85 \times 8.4\% \approx 24\%$ and $R_2(min) = 0$. It is important to mention, that one may obtain the maximal and the minimal coefficients of the reflection, only when the region of the uniform thickness (i.e. $L = \text{const}$) inside nano-cell is larger than the diameter of laser beam. Hence, the achievement the maximal and the minimal reflection, indicates a correctly selected homogeneous region L.

Thus, the intensity of the radiation transmitted through the nano-cell with $L = k\lambda/2$ will have the maximal magnitude, which has the intensity of two reflections less (from the first surface (R_1) and from the backside surface (R_3)) than the initial radiation, i.e. $R_1 + R_3 \approx 16.8\%$ less. When the thickness $L = (2k+1)\lambda/4$, the transmitted intensity is $16.8\% + 24\% = 40.8\%$ less than the initial intensity. Fig. 1.21 shows the variation of the intensity depending of the thickness of the cell calculated with the relation (1.3) (for certain parameters of the nano-cell) for $\lambda = 633$ nm and $\lambda = 780$ nm. Since the calculated curves demonstrates a periodical variation of the reflection, the thickness L can be measured up to a multiple of $\lambda/2$, particularly it is impossible to distinguish $L = \lambda/2$, $L = \lambda$ and $L = 3\lambda/2$. In order to eliminate this complication, we did the following in our experiments: the nano-cell is constructed so, that it contains the thickness $L < 100$ nm. Such kind of small thicknesses are visually observable: the reflection from this thickness is vanishing and visually this region has white colour. In the marginal case of zero thickness, an "optical contact" arises and obviously no reflection appears. Hence, measuring the thickness L from the region of $L < 100$ nm, such kind of ambiguity will be eliminated. Since for the different wavelength the maxima and the minima of the reflection achieve for the different thicknesses (see fig. 1.21), in experimental conditions it is more convenient to make a measurement of the nano-cell thickness directly

using setup DL (for example $\lambda = 780$ nm). In this case the thicknesses $L = \lambda/2$ (390 nm), $L = \lambda$ (780 nm), $L = 3\lambda/2$ (1170 nm) etc. give minimal reflection ($R_2 = 0$), while the maxima of reflection are reached for $L = \lambda/4$ (195 nm), $L = 3\lambda/4$ (585 nm) etc. It is possible to measure the maxima and the minima with a high precision, that is to determine the thickness of the gap with the precision ± 20 nm.

The thickness of the gap can be measured as well as by the transmission intensity: for example, in the case of $L = (2k+1)\lambda/2$ the minimum of the reflection is observed, that is in the transmitted light, the maximum of intensity will be detected, and inversely: in the case of $L = (2k+1)\lambda/4$, when the reflection is maximal, it will be minimal intensity in transmission.

It is important to note, that in some cases, the region of homogeneous thickness has a small size. It is clearly visible, that the reflection from the region with a homogeneous thickness, has a homogeneous color, due to the interference conditions for a certain wavelength of the light. In this case, in order to increase the precision of the measurement it is necessary to decrease the laser beam diameter in a spot with a diameter $D_L = 0.3 - 0.5$ mm. The advantage of this method is the possibility to make a measurement during the experiment, this measurement being precisely localized and with high accuracy.

1.6 Summary

1. We have specified the experimental technique used in the experimental setup and described the block-scheme, construction and technical characteristics of the continuous wave external cavity DL ($\lambda = 780$, 794 nm).

2. We compare the fluorescence and transmission spectra obtained by ordinary cell (several centimeters length) and nano-cell ($L = \lambda/2,\ \lambda$). We showed the sevenfold narrowing of the fluorescence and $\sim$ fivefold narrowing of the transmission spectra for $L = \lambda/2$ nano-cell in comparison with the ordinary cell.

3. Here is given a critical review of different techniques of the sub-Doppler spectroscopy: a) Saturated absorption; b) Selective reflection; c) Atomic beams; d) Method of coherent

population trapping; e) Method based on using cells with thickness in range $0.5-1$ mm. We analyzed the advantages and the disadvantages of these techniques in comparison with the one based on the nano-cell. We demonstrate the comparison of this techniques with the sub-Doppler spectroscopy based on the usage of the nano-cell.

4. It is described the construction of thin cell and nano-cells containing Rb vapours of thickness varying in range 30 nm $-$ 3 μm.

5. It is described the construction of the combined cell containing Rb vapour and additional quantity of Ne buffer gas: ordinary about one centimeter cell interconnected by a thin sapphire side-arm to the nano-cell with the thickness varying in the range $100-4000$ nm.

Chapter 2

Influence of external conditions on the spectra

Introduction. Recently it has been demonstrated that sealed-off submicron-thin cell containing atomic vapour of Rb, Cs, etc. with the thickness of the vapour column L comparable or smaller than resonant optical wavelength λ, is a very promising tool for fundamental studies of atom-light, atom-atom, atom-surface and atom-external magnetic field interactions [36, 86, 87]. The absorption and fluorescence spectra for D_1 and D_2 lines of Rb and Cs in a nano-cell as a function of L/λ, with L being in the range of $50 - 3000$ nm, have been published in [39, 42, 86–88]. It was revealed that for low laser intensity (< 1 mW/cm^2), the absorption linewidth of optical hyperfine transition between ground and excited levels exhibits oscillating behaviour and has the minimum value when $L = (2n + 1)\lambda/2$, and the maximum value when $L = n\lambda$ (n is integer). This is the manifestation of collapse and revival of Dicke-type coherent narrowing effect (DCN) [39]. For higher excitation intensity (~ 10 mW/cm^2), VSOP resonances appear in the transmission spectrum when $L = n\lambda$. Narrow-band VSOP resonances are located exactly at the atomic transitions, which was already used to form frequency reference for Rb and Cs atomic transitions [41, 42, 88].

The investigation of the influence of experimental parameters on the resonant absorption and fluorescence spectra behaviour is one of the most important problems of spectroscopy. Due to this the influence of the resonant laser intensity, the temperature of the nano-cell side-arm and the modification of spectra in presence of buffer gas were investigated. Study

of this processes allows one to determine the optimal experimental parameters and to explore the peculiarities of these influences for a nanometric thicknesses of vapour column. For these studies we have also developed special multi-region cells (MRC) with buffer gas.

In this chapter we present new peculiarities that we have observed for the first time in MRC and compare them with the results obtained with an ordinary-length buffered cell. The presented results are important for a further development of nanometric size devices.

2.1 Influence of buffer gas on the absorption and fluorescence spectra

Buffer gas is widely used in different fields of the experimental science. A lot of linear, nonlinear and coherent processes demonstrate essential modification of behaviour in the presence of buffer gas. Use of the buffer gas in the processes of Electro-magnetically induced transparency and CPT processes allows one to obtain ultra narrow optical resonances ($\sim$ 50 Hz). The implementation of the ultra narrow spectroscopy found its application in different fields such as metrology (the determination of the atomic transitions frequencies with a precision of several Hz and the development of new and more correct time standards), development of quantum magnetometers with a precision of pT, quantum communication, information optical storage etc. Besides, buffer gas is used in others actively developed fields, for instance in the formation of Bose-Einstein condensate where it is used as cooler an etc.

However the presence of the buffer gas inflicts a worse detection of the resonant absorption and fluorescence spectra, and washes out sub-Doppler features in saturated absorption spectroscopy [1–4]. For an ordinary Rb cm-size cell with addition of buffer gas, the velocity selective optical pumping/saturation (VSOP) resonances in saturated absorption spectra are fully suppressed if neon pressure > 0.5 torr. One could expect that the presence of a buffer gas can substantially alter the effect of collapse and revival of Dicke-type narrowing for the thickness $L = \lambda/2$ and $L = \lambda$, where λ is a resonant laser wavelength of $D_{1,2}$ lines.

We demonstrates a spectacular difference which is that for $L = \lambda$, VSOP resonances as

well as effect of collapse and revival of Dicke-type narrowing for the thickness $L = \lambda/2$ and $L = \lambda$ are still observable even when neon pressure is ≥ 6 torr. We suggest a online buffer gas pressure monitoring gauge using the narrow fluorescence spectra at $L = \lambda/2$.

2.1.1 Theoretical background

We consider a three-level atomic system (see fig. 2.1) interacting with a linearly polarized laser radiation of frequency ω. The three levels under consideration are: one ground hyperfine level $F = 1$ ($|1\rangle$) and two excited levels $F' = 2,\ 3$ ($|2\rangle$ and $|3\rangle$). For simplicity, we consider a one-dimensional situation, where the driving field is in the $\pm z$-direction and the atom is moving along z-direction with a velocity V_z. The detunings of the laser from the transitions $|1\rangle \rightarrow |2\rangle$ and $|1\rangle \rightarrow |3\rangle$ are $\Delta_1 = \omega_{21} - \omega - \vec{k}V_z$ and $\Delta_2 = \omega_{31} - \omega - \vec{k}V_z$, respectively, where $\vec{k}V_z$ is the shift due to the Doppler effect, with $\vec{k}$ being the wave vector of the excitation light. We analyze the observed spectra of resonant absorption and fluorescence on the basis of a standard density-matrix approach [89, 90].

The dynamical behaviour of the density matrix ρ is given by the Liouville equation of motion

$$\dot{\rho} = \frac{1}{i\hbar}\left[\hat{H}_0 + \hat{V}, \rho\right] + \text{relaxation terms}, \tag{2.1}$$

where $\hat{H}_0$ is the unperturbed atomic Hamiltonian, and $\hat{V} = -\hat{\mathrm{d}}E(t)$ is the atom-light interaction Hamiltonian in the electric-dipole approximation with $\hat{\mathrm{d}}$ being the electric dipole operator and $E(t)$ the electric field of the radiation light. The components of the density-matrix elements of Eq. (2.1) can be represented by in the rotating-wave-approximation

$$\begin{aligned}
\dot{\rho}_{11} &= -2\ \mathrm{Im}(\Omega_1^*\rho_{21}) - 2\ \mathrm{Im}(\Omega_2^*\rho_{31}) + \gamma_{21}\rho_{22} + \gamma_{31}\rho_{33}, \\
\dot{\rho}_{22} &= 2\ \mathrm{Im}(\Omega_1^*\rho_{21}) - 2\Gamma\rho_{22}, \\
\dot{\rho}_{33} &= 2\ \mathrm{Im}(\Omega_2^*\rho_{31}) - 2\Gamma\rho_{33}, \\
\dot{\rho}_{21} &= i\Omega_1(\rho_{11} - \rho_{22}) - i\Omega_2\rho_{32}^* - (\Gamma + i\Delta_1)\rho_{21}, \\
\dot{\rho}_{31} &= i\Omega_2(\rho_{11} - \rho_{33}) - i\Omega_1\rho_{32} - (\Gamma + i\Delta_2)\rho_{31}, \\
\dot{\rho}_{32} &= i\Omega_2\rho_{21}^* - i\Omega_1^*\rho_{31} - (2\Gamma + i\delta)\rho_{32},
\end{aligned} \tag{2.2}$$

where δ is the excited state hyperfine splitting, γ_{i1} is the rate of the spontaneous decay from the excited state $|i\rangle$ to the ground state $|1\rangle$, and $2\Gamma = \gamma_{21} + \gamma_1^{'} = \gamma_{31} + \gamma_2^{'}$. Here $\gamma_1^{'}$ and $\gamma_2^{'}$ are the rates of population lost from the system, responsible for the optical pumping of the other ground hyperfine level with $F = 2$ denoted as $|1'\rangle$ in fig. 2.1. The Rabi frequencies of the corresponding transitions are defined as $\Omega_1 = d_{12}E/2\hbar$ and $\Omega_2 = d_{13}E/2\hbar$, respectively. As the atoms are in thermal motion, we take the average of all ρ_{ij} values over the range of velocities, weighted by the one dimensional Maxwellian velocity distribution.

To take into account the laser bandwidth we use the phase diffusion model of Wigner-Levy [90,91], in accordance with which it is assumed that the laser radiation has a Lorentzian spectrum with the FWHM of γ_L. The bandwidth is incorporated into Eqs. (2.2) as a relaxation term for the non-diagonal element of the density matrix in accordance to the procedure given in [92]. The main assumptions made in the model are as follows: the atomic number density is assumed to be low enough so that the effect of collisions between the atoms can be ignored; the atoms experience inelastic collisions with the cell walls, i.e. atoms lose completely their optical excitation; the incident beam diameter largely exceeds the cell thickness which allows one to neglect the relaxation of atoms travelling out of the diameter of the laser beam. These assumptions allow us to take into account the collisional relaxation of each atom by solving the temporal equations for the atomic density matrix with proper boundary conditions for each atom separately. The effect of the reflection of the radiation from the highly-parallel windows of the nano-cell behaving as a Fabry-Perot cavity [40] is also taken into account. The model used here is described in [40, 41].

Fig. 2.3, 2.4 present the calculated dependence of the fluorescence linewidth and the amplitudes as a function of the neon pressure for Rb, D_1 line, $F_g = 3 \rightarrow F_e = 2, 3$, $\Omega_1 = \dfrac{d_{12}}{d_{13}}\ \Omega_2\ \Omega_2 = 0.4\gamma$, $V_T = 300$ m/s, where $\gamma = \gamma_N$ (6 MHz) + 3.7 MHz (the broadening caused by Rb-Rb collisions at 120 °C at the side-arm) + γ_L (laser linewidth $\sim$ 0.8 MHz) $\sim$ 10 MHz. One of the possible applications using this dependence is the development of an online pressure gauge.

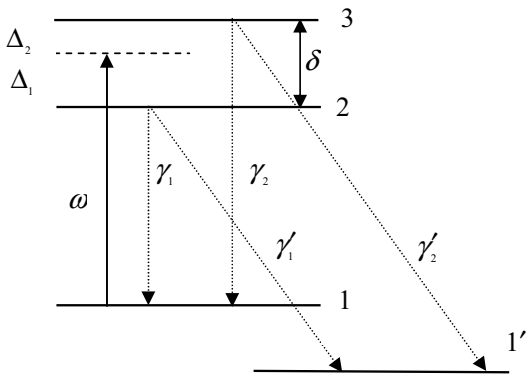

Figure 2.1: The three-level scheme around the D_1 line of ^{85}Rb.

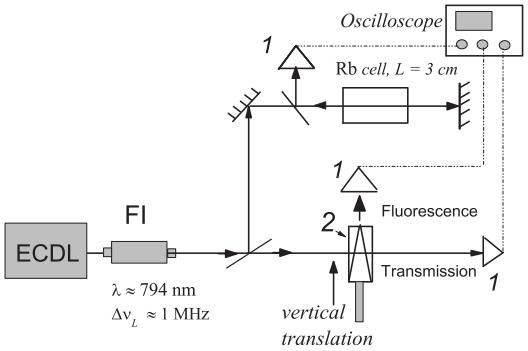

Figure 2.2: Sketch of the experimental setup. The laser beam is produced by ECDL; FI - Faraday isolator is used to avoid optical feedback. 1 - photo-detectors, 2 - MRC (only nano-cell is shown); the upper branching is to form a reference SA spectrum.

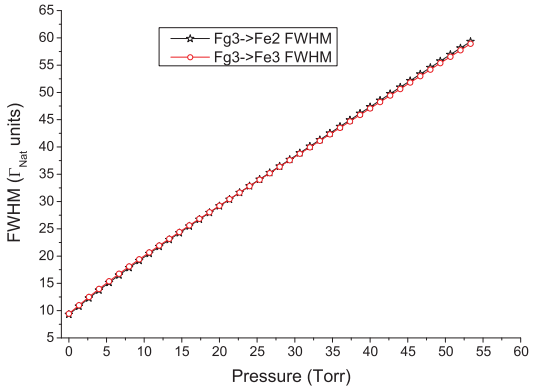

Figure 2.3: Dependence (theory) of the fluorescence linewidth for $L = \lambda/2$ as a function of the neon pressure for Rb D_1 line ($F_g = 3 \to F_e = 2,\ 3$), $\Omega_2 = 0.4\ \gamma$, $V_T = 300$ m/s.

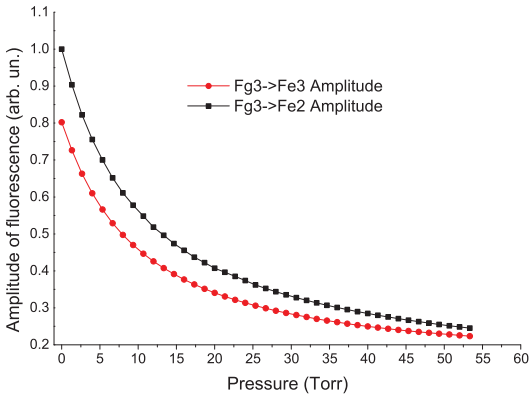

Figure 2.4: Dependence (theory) of the fluorescence amplitudes for $L = \lambda/2$ as a function of the neon pressure for Rb D_1 line ($F_g = 3 \to F_e = 2,\ 3$), $\Omega_2 = 0.4\ \gamma$, $V_T = 300$ m/s.

2.1.2 Experimental results and comparison with theory

MRC consists of two interconnected cells and a side-arm containing metal. The nanometric region (shown in the upper part of fig. 1.18) has a wedged thickness of the gap between the windows that allows one to exploit atomic vapour column thickness in the range of $0.1-4$ μm. The nano-cell is connected through a thin sapphire pipe with the 1 cm-long cell region (the lower part of fig. 1.18) with 2 sapphire windows. The 1 cm-long cell is terminated by a sapphire side-arm containing metallic Rb.

We have used 2 MRCs, filled with 6 torr and 20 torr of neon gas. Such design of MRC allows one to compare absorption and fluorescence signals simultaneously recorded for nano-cell and 1 cm-long ordinary cell. The MRC is placed in the oven with openings, which allow passing the laser radiation and registration of fluorescence in the direction perpendicular to the laser beam. The temperature of the MRC was kept at $\sim$ 120 °C at the side-arm (this latter defines Rb atomic vapour pressure), and somewhat (20 °C) higher at the windows in order to prevent Rb vapour condensation at the windows. This regime corresponds to the number density of Rb atoms $N \sim 10^{13}$ at/cm^3. The sketch of the experimental setup is presented in fig. 2.2.

To measure the transmission and fluorescence spectra at different nano-cell thicknesses, the oven with MRC was smoothly translated vertically as indicated by an arrow in fig. 2.2. Note that although it is technically easier to move only the nano-cell, in this case the temperature regime of the cell will be changed during the movement.

Extended cavity cw tunable diode laser with $\lambda = 794$ nm was used for the case of Rb D_1 line. The laser radiation is divided into two beams: the main beam is directed to a nano-cell (MRC) to study the absorption and fluorescence processes, while the second beam is used to form a reference spectrum by saturation absorption (SA) technique in a separate Rb cell. Atomic transitions of ^{85}Rb and ^{87}Rb D_1 line are shown in fig. 1.4. Transmission spectra for ^{85}Rb D_1 line $F_g = 3 \rightarrow F_e = 2,\ 3$ and ^{87}Rb $F_g = 2 \rightarrow F_e = 2$ transitions recorded in nano-cell filled with pure Rb (for $L = \lambda/2$ and $L = \lambda$) are shown in fig. 2.5(a) for laser

intensity < 0.1 mW/cm^2. Dicke-type coherent narrowing (DCN) effect is well seen: the spectral linewidth for $L = \lambda/2$ (~ 150 MHz) is narrower by a factor 3 than that for $L = \lambda$ (~ 450 MHz). Transmission spectra for the nano-cell filled with Rb and 6 torr of neon are shown in fig. 2.5(b) for the same thicknesses. DCN effect is still well seen [39]. The further increase of buffer gas pressure (fig. 2.5(c)) results in broadening and contrast reduction of DCN dips. We should note that transmission for $L = \lambda$ in fig. 2.5(b), (c) is more sensitive to I_L as compared with the case of $L = \lambda/2$. Particularly, at $I_L \sim 1$mW/cm^2 transmission for $L = \lambda$ can be higher (the absorption is lower) than for $L = \lambda/2$, which is caused by stronger influence of an optical pumping for $L = \lambda$ [88]. For this reason, in order to get graphs visually comparable with those presented in fig. 2.5(a) we have adjusted I_L for $L = \lambda$.

Fig. 2.6 presents theoretically calculated spectra corresponding to those presented in fig. 2.5, preserving the labeling (only transitions $F_g = 3 \to F_e = 2, 3$ are considered in the model). A good agreement with experimental results is seen. The striking point is that even with neon gas pressure up to 20 torr the DCN is still observable (graphs 2.6(c)), though less pronounced as compared with (a) and (b).

It is important to note that in the case of an ordinary $0.1 - 10$ cm-long alkali metal vapour cell, the addition of > 0.5 torr of (any) buffer gas leads to disappearance of all the sub-Doppler features in the saturated absorption spectrum. Curve (1) in fig. 2.7 shows the well-known SA spectrum obtained with 3-cm long ordinary cell with pure Rb. The VSOP and crossover (CO) resonances are well seen. The same spectrum recorded with 1-cm long Rb cell with 6 torr of neon is shown by curve (2). One can see that here all the VSOP and CO resonances are completely vanished. This is caused by the fact that in the case of buffer gas use there is no anymore selected group of atoms (due to the frequent collisions of Rb atoms with Ne gas), which is necessary to form sub-Doppler resonances in the transmission spectrum inside the Doppler-broadened one.

Fig. 2.8 shows transmission spectra for nano-cell with $L = \lambda$ on ^{85}Rb $F_g = 3 \to F_e = 2,\ 3$ and ^{87}Rb $F_g = 2 \to F_e = 2$ transitions ($I_L \sim 10$ mW/cm^2) for the following cases: curve (1) - nano-cell with pure Rb: the linewidth of VSOP resonances ~ 25 MHz; curve (2) - nano-cell

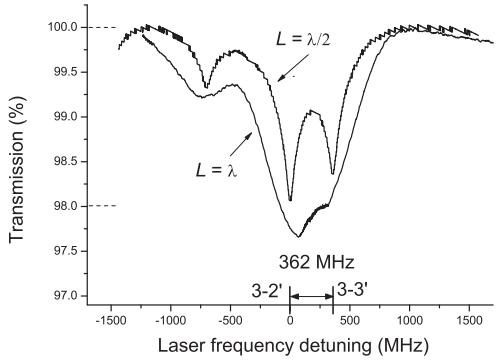

(a) Nano-cell with pure Rb, DCN and its collapse is well seen.

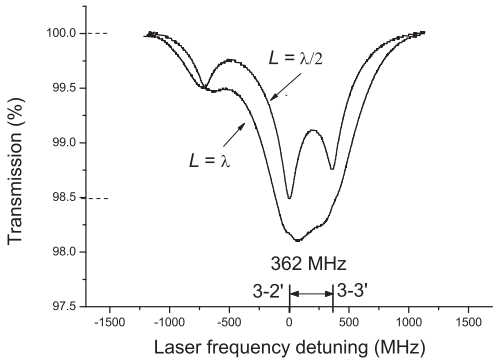

(b) Nano-cell with Rb + 6 torr Ne, DCN and its collapse is still well seen.

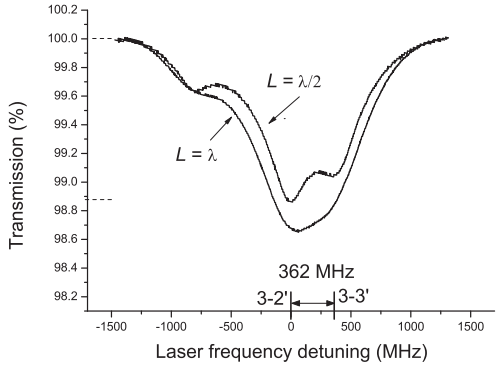

(c) Nano-cell with Rb + 20 torr Ne, DCN and its collapse is yet seen.

Figure 2.5: Experimental transmission spectra for $L = \lambda/2$ and $L = \lambda$. ^{87}Rb $F_g = 2 \rightarrow F_e = 2$ and ^{85}Rb $F_g = 3 \rightarrow F_e = 2, 3$, D_1 line transitions.

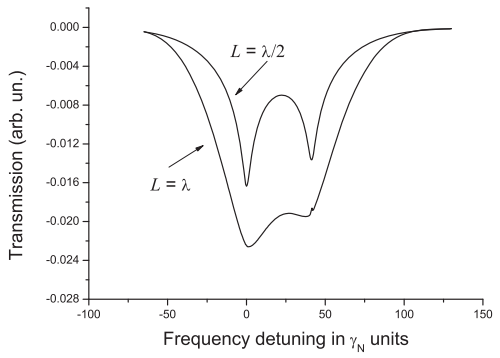

(a) Pure Rb, $L = \lambda/2$, and λ, $\Omega_L \sim 0.04\ \gamma$.

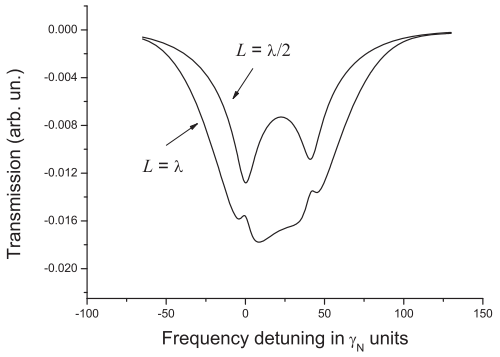

(b) Rb + 6 torr Ne for $L = \lambda/2$ and λ, $\Omega_L \sim 0.4\ \gamma$

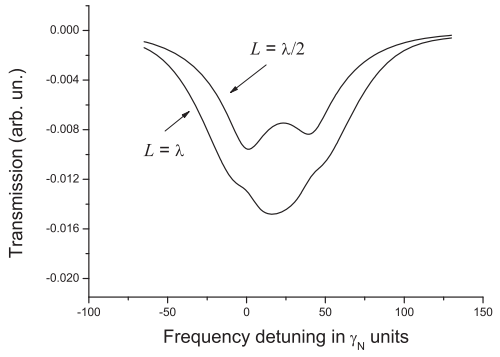

(c) Rb + 20 torr Ne, for $L = \lambda/2$ and λ, $\Omega_L = 0.8\ \gamma$.

Figure 2.6: Calculated spectra for cases presented in Fig. 2.5. ^{85}Rb, D_1 line only for $F_g = 3 \rightarrow F_e = 2, 3$ transitions: $V_T = 300$ m/s, pressure broadening 7 MHz/torr.

with Rb and 6 torr Ne: VSOP linewidth is $\sim$ 90 MHz; curve (3) - nano-cell with Rb and 20 torr Ne: VSOP resonances are absent.

The comparison of fig. 2.7 and fig. 2.8 shows a striking peculiarity: the VSOP still exist for the nano-cell with Rb + 6 torr neon when $L = \lambda$. This important difference in behaviour as compared with ordinary 1 cm-long cell can be explained as follows. The free path length of Rb atom for 6 torr Ne is somewhat less than 10 μm, so the atoms flying parallel to the windows inside the laser beam of 2 mm diameter experience hundreds of collisions with Ne atoms causing just additional broadening of VSOP. Meanwhile collisions of Rb atoms with longitudinal velocity with Ne atoms have a negligible impact since the thickness of nano-cell for $L = \lambda$ is less than 1 μm. It is important to note that the observed peculiarities of VSOP formation presented in fig. 2.8 are well described by the theoretical model (the graphs are not shown). Namely, the theory predicts i) formation of narrow VSOP with linewidth of $\sim \gamma_N$ in the case of pure Rb; ii) VSOP broadening for the case illustrated by curve (2); iii) absence of VSOP for the case illustrated by curve (3). It was demonstrated in [88] that under optimal experimental conditions, the FWHM of the fluorescence spectrum of an individual transition for $L = \lambda/2$ can be reduced down to $\sim$ 70 MHz (in the case of ordinary cm-size cell the value is $\sim$ 500 MHz). This striking feature of the nano-cell offers an important benefit in the case of the nano-cell filled with buffer gas, too. Fig. 2.9 presents fluorescence spectrum when $L = \lambda/2$ for 3 cases ((a) - experiment, (b) - theory): curve (1) - nano-cell with pure Rb vapour; curve (2) and (3) - nano-cell containing Rb vapour + 6 torr and 20 torr Ne, correspondingly. For theory (b): Rabi frequency $\Omega_2 = 0.4\gamma$ ($\gamma \sim 10$ MHz). For the calculations we used broadening rate of 7 MHz/torr, thus for 6 torr, Γ(total) $\sim$ 52 MHz, and for 20 torr, Γ(total) $\sim$ 150 MHz (take care that all these quantities in MHz have been divided by 2π in [1] in order to lead to computational simplifications), and Maxwellian velocity distribution with $V_T = 300$ m/s. Laser intensity is $\sim$ 10 mW/cm^2. As it is seen, up to 20 torr Ne the fluorescence spectrum has a sub-Doppler linewidth. As it is shown below, a tool for *in situ* pressure monitoring based on this effect can be developed.

In [93, 94] it was demonstrated a simple way to separate alkali metal isotopes: hydrogen

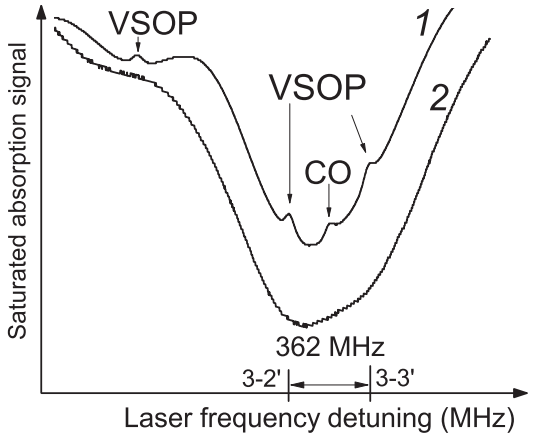

Figure 2.7: (1)- well-known SA resonances for 3 cm-long cell (pure ^{85}Rb, D_1 line), CO is crossover resonance; (2) - SA spectrum for 1 cm-long cell filled with Rb + 6 torr Ne showing absence of VSOP resonances.

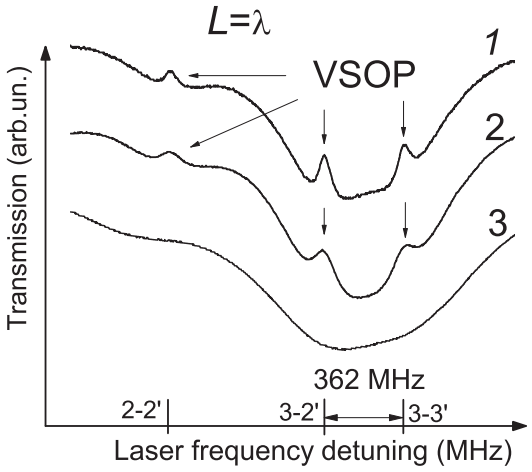

Figure 2.8: Rb D_1 line transmission spectra for $L = \lambda$. (1) - pure Rb nano-cell, VSOP resonances are well pronounced; (2) - Rb + 6 torr Ne nano-cell, VSOP resonances are broadened; (3) - Rb + 20 torr Ne nano-cell, VSOP resonances are washed out.

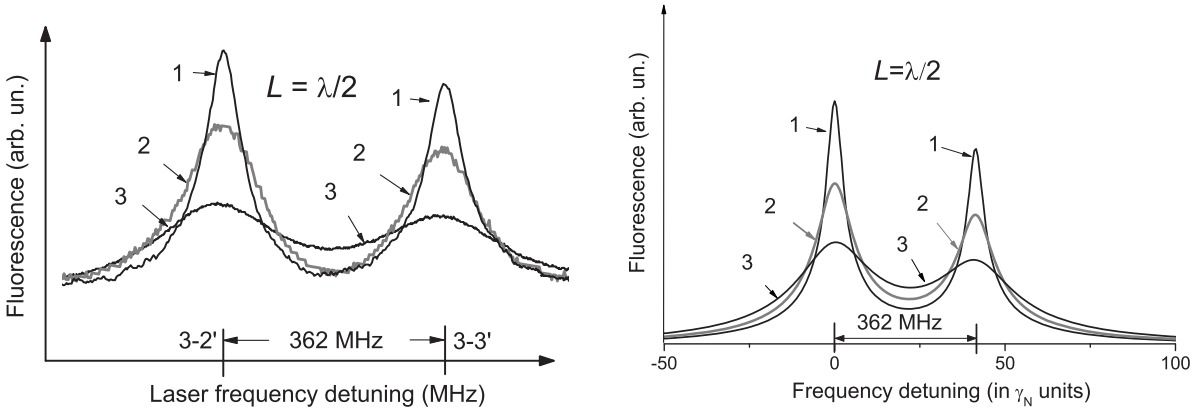

(a) Experiment

(b) Theory

Figure 2.9: ^{85}Rb D_1 line fluorescence spectra for $F_g = 3 \to F_e = 2,\ 3$ transitions in nano-cell with $L = \lambda/2$ for 3 cases: curves (1) - nano-cell with pure Rb: linewidth 76 MHz (a) and 72 MHz (b); curves (2) - nano-cell with Rb + 6 torr Ne (grey curve): 145 MHz (a) and 137 MHz (b); curves (3) - nano-cell with Rb + 20 torr Ne: 230 MHz (a) and 240 MHz (b). $\Omega_L = 0.4\gamma$, $V_T = 300$ m/s, pressure broadening 7 MHz/torr.

gas with a pressure of ~ 20 torr is added to the cell containing alkali metal vapour. Then the needed isotope is excited by a narrow-band resonant laser radiation (for the case of Rb vapour confined in a cell of ordinary $1-5$ cm length, the Doppler-broadened lines of ^{85}Rb and ^{87}Rb practically do not overlap). Selectively excited to 5P state isotope (e.g., ^{85}Rb) even at room temperature easily undergoes two-step chemical reaction with hydrogen, $^{85}Rb^* + H_2 \rightarrow {}^{85}Rb + H_2^*$; $^{85}Rb^* + H_2^* \rightarrow {}^{85}RbH^* + H$ forming ^{85}Rb hydride RbH. The reaction is more efficient when the cell is heated, so it is justified to use a sapphire cell which is resistive to chemically aggressive alkali vapour. The isotopic-selective hydride gets condensed on the cell walls. When the reaction is over, the residual non-reacted vapour can be driven out by freezing the cell side-arm, and the isotopic-pure hydride is easily dissociated by heating the cell body to > 300 °C. The pressure of gas (notably H_2) in the cell strongly varies in the course of chemical reaction; that is why it is important to have a tool for *in situ* pressure monitoring. The use of conventional room-temperature gas pressure gauges, especially for heated cell, is impossible because alkali metal vapour would condensate on a gauge. Alternatively, an nano-cell can be soldered to the main separation cell as is shown in fig. 1.18 and heated in the same oven up to needed temperature. The pressure in this case can be monitored online using curves similar to those presented in fig. 2.3, 2.4.

2.1.3 Conclusion

Comparison of the resonant absorption in the nano-cell filled with Rb vapour with another nano-cell filled with Rb and neon gas with pressure 6 torr and 20 torr shows that the spectra of the resonant absorption demonstrate sub-Doppler narrowing for the thickness $L = \lambda/2$ and broadening for the thickness $L = \lambda$, thus manifesting the effect of collapse and revival of Dicke-type narrowing ($\lambda = 794$ nm is a resonant laser wavelength). In an ordinary Rb cell with $L = 0.1 - 10$ cm filled with buffer gas, in the saturated absorption spectra VSOP and CO resonances are washed out when pressure > 0.5 torr. In contrast, for the nano-cell with $L = \lambda$ the VSOP resonances located at the atomic transition are still observable even when

neon pressure is 6 torr. Narrow-band fluorescence spectra of the nano-cell with $L = \lambda/2$ can be used as a convenient tool for online buffer gas pressure monitoring in the MRC in its several centimeter-long part, for the conditions when ordinary pressure gauges are unusable. Developed theoretical model well describes all experimentally observed peculiarities.

2.2 Influence of laser intensity and cell thickness on transmission and fluorescence spectra

In ordinary cm-size cells, for low absorption and low laser intensity regime, the behaviours of the resonant absorption and fluorescence spectra are very similar to each other [44]. In the case of a nano-cell, the following four distinctions have been revealed: i) the fluorescence spectral width is always narrower ($1.5 - 1.8$ times for $L = \lambda/2$, and ~ 3 times for $L = \lambda$), than the absorption width for the same transition; this general result is related with longer time needed to buildup the fluorescence, which implies absorption and emission cycle, thus imposing more strict atomic velocity restrictions (the atom has to emit photon before being quenched on the cell window); ii) in contrast to transmission, the increase of L results in monotonic increase of fluorescence spectral width, without oscillating behaviour versus L; iii) the fluorescence spectral width remains below the Doppler-broadening even when the thickness of vapour column is increased to $L \sim 4$ μm, while the absorption spectral width for these values of L reaches the Doppler-broadened width of cm-size cells; iv) the VSOP resonance peak in nano-cell transmission at $L = \mathrm{n}\lambda$ is observable for radiation intensities of several mW/cm^2, while the intensity required to observe VSOP resonance dip in the fluorescence spectrum is more than by one order of magnitude larger. Although sensitive detection, as well as higher laser intensity is needed to record resonant fluorescence emitted by a nano-cell, the first gained advantage is narrower sub-Doppler spectral width, and the second is that the fluorescence signal appears on a nearly zero background.

In particular experiment, the laser beam (ECDL, $\lambda = 794$ nm, $\gamma_L = 1$ MHz) is sent onto

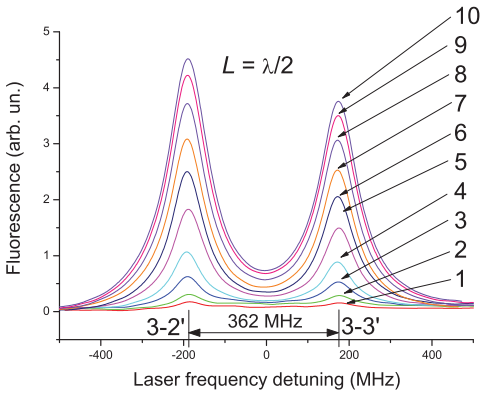

Figure 2.10: Fluorescence spectrum on Rb D_1 line emitted by nano-cell with $L = \lambda/2$ for different values of laser intensity. For the curves under number from 1 to 10 the corresponding laser intensities are: 4, 8, 20, 40, 80, 120, 160, 200, 240 and 252 mW/cm^2.

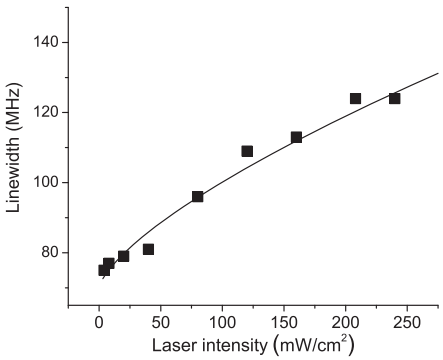

Figure 2.11: The spectral width of the fluorescence of the individual transition versus I_L: squares - experiment, solid line - plotted by empiric formula.

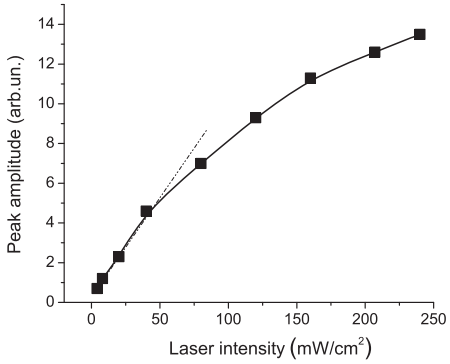

Figure 2.12: The peak amplitude of the fluorescence of the individual transition versus I_L: the squares - experiment, solid line-guide for the eyes, dot - line shows linear dependence.

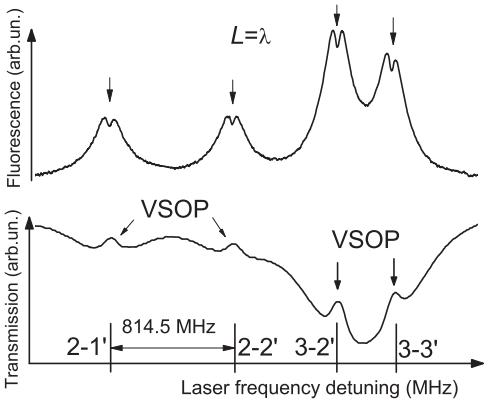

Figure 2.13: Fluorescence spectrum (upper curve) for the thickness $L = \lambda$, $I_L \sim 30$ mW/cm^2, dip of reduced fluorescence (mentioned by the arrows) appear at all transitions, the spectral width is ~ 20 MHz. The lower curves shows VSOP resonances in the transmission spectra, for $L = \lambda$.

the nano-cell at nearly normal incidence, laser intensity is $\sim$ 10 mW/cm^2, the operation temperatures are $T_{SA} \sim 110$ °C, and $T_W \sim 140$ °C. The fluorescence spectrum of Rb D_1 line for $L = \lambda/2$ is shown in fig. 1.3 (lower curve). The upper curve is the fluorescence emitted by an ordinary cm-size cell. As it is seen, all hyperfine transitions (labeled correspondingly) are resolved in the lower curve. Under optimal conditions (i.e. low I_L and sensitive detection), the FWHM of the fluorescence spectrum for an individual transition can be reduced down to $\sim$ 70 MHz (in the case of ordinary cm-size cell it is $\sim$ 500 MHz). Note that relative amplitude of the fluorescence peaks are in agreement with the transitions intensities. The line shape and magnitude of the resonant fluorescence on $F_g = 3 \rightarrow F_e = 2, 3$ transitions of the ^{85}Rb D_1 line, obtained for thicknesses $L = \lambda/2$ for different values of laser intensity is shown in fig. 2.10. For the curves under number from 1 to 9 the corresponding laser intensities are: 4, 8, 20, 40, 80, 120, 160, 200, 240 and 252 mW/cm^2. The striking point is that as it is seen from the figure even at 240 mW/cm^2 there is no sign of any dip in the fluorescence spectrum, meanwhile as it is shown below when the thickness of the atomic vapour is $L = \lambda$ a dips caused by the velocity selective optical pumping process appear when the intensity is $\sim$ 30 mW/cm^2 (see fig. 2.13). A similar behaviour exhibits transmission spectrum for thicknesses $L = \lambda/2$: the experimental results obtained at $I_L \sim 1$ W/cm^2 show that no dips of a reduced absorption appear in the transmission spectrum, in contrast $I_L \sim$ of several mW/cm^2 is sufficient to form dips at $L = \lambda$. These both effects for the fluorescence and absorption are caused by a strong Dicke-type coherent narrowing regime at thickness $L = \lambda/2$.

The spectral width of the fluorescence of the individual transition (after fitting with 2 Lorentzian curves - see below) as a function of the laser intensity is presented in fig. 2.11. The solid curve is plotted by empiric formula: $\gamma_{FL}[\text{MHz}] = 70[\text{MHz}] + 1.2 \times I^{0.7}[\text{mW/cm}^2]$. As it is seen from the formula the value of γ_{FL} at $L = \lambda/2$ will reach the Doppler spectral width of 500 MHz at laser intensity $\sim$ 4.5 W/cm^2. Thus, the fluorescence spectral width at $L = \lambda/2$ can be used as a direct laser intensity gauge.

The peak amplitude of the fluorescence for the individual transition as a function of the laser intensity is presented in fig. 2.12. It is interesting to note that up to $50 - 60$ mW/cm^2

there is a linear dependence, meanwhile for an ordinary cm-size cell the saturation effects appear for the laser intensity of a several mW/cm^2. This is caused by the fact that as the size of the vapour cell is reduced, the lifetime of the ground-states becomes shorter because of collisions of the atoms with the cell windows, which cause transitions between the ground states. Thus, the value of $\Gamma = (2\pi t)^{-1}$, which is in denominator of the formula (1.1), where $t = L/V_T$ (V_T is the thermal velocity) for the case of $L = \lambda/2 \sim 0.4$ μm is large enough ($\Gamma > 100$ MHz), and one could expect that the efficiency of the optical pumping process will be reduced. Note, that further reduction of the thickness $L < \lambda/2$ will causes additional increasing of the saturation intensity value for the fluorescence process.

In fig. 2.13, 2.14 it is presented fluorescence spectra for the thickness $L = \lambda$ (upper curves) with the laser intensity $\sim$ 30 mW/cm^2. As it is seen VSOP dips of reduced fluorescence (mentioned by the arrows) appear at all transitions of the ^{87}Rb, $F_g = 2 \rightarrow F_e = 1, 2$ and ^{85}Rb, $F_g = 3 \rightarrow F_e = 2, 3$ fig. 2.13 and ^{85}Rb, $F_g = 2 \rightarrow F_e = 2, 3$ fig. 2.14. The spectral width of the dip of reduced fluorescence is $\sim$ 20 MHz. Optimization of experimental parameters, in particular, use of lower laser intensity and uniform area of the thickness $L = \lambda$ should result in smaller spectral width (less than 10 MHz). Note, that the dips of reduced fluorescence appear exactly at the frequency of atomic transitions. The lower curves shows VSOP resonances in the transmission spectra for $I_L = 30$ mW/cm^2. Note that for VSOP formation in the transmission spectrum when $L = \lambda$, the laser intensity is of several mW/cm^2 and the laser spectral width in the range of $1 - 50$ MHz is sufficient. Though, for the dip formation in the fluorescence spectrum laser intensity has to be > 20 mW/cm^2, and the laser spectral width has to be strictly no more than a few MHz. Thus, the VSOP formation in transmission spectra when $L = \lambda$ is a more robust process.

The line shape and magnitude of the resonant fluorescence on $F_g = 3 \rightarrow F_e = 2, 3$ transitions as a function of the nano-cell the thickness L varying in the range of $\lambda/2$ up to 4λ (with $\lambda/2$ step) for the laser intensity $\sim$ 10 mW/cm^2 is shown in fig. 2.15. As it was mentioned, the narrowest spectral width of the fluorescence is achieved when L is in the range $\lambda/4 < L < \lambda/2$, particularly for $L = \lambda/2$ ($\sim$ 70 MHz) presented in fig. 2.15. As it

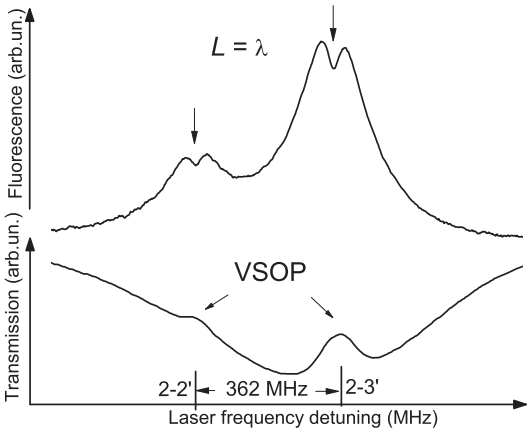

Figure 2.14: Fluorescence spectrum (upper curve) for the thickness $L = \lambda$, $I_L \sim 30$ mW/cm^2, dip of reduced fluorescence (mentioned by the arrows) appear at all transitions, the spectral width is ~ 20 MHz. The lower curves shows VSOP resonances in the transmission spectra, for $L = \lambda$.

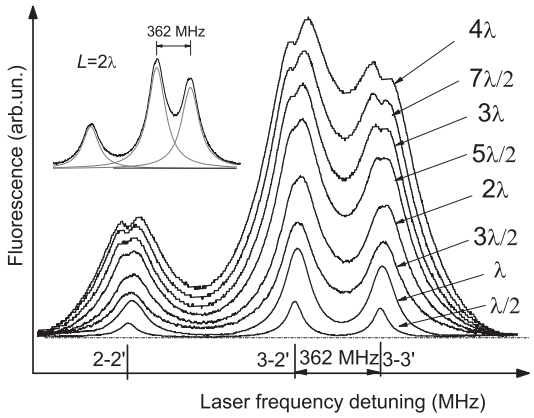

Figure 2.15: Fluorescence spectrum on the ^{87}Rb, $F_g = 2 \to F_e = 2$, ^{85}Rb, $F_g = 3 \to F_e = 2, 3$ transitions emitted by nano-cell with different values of the thickness L: from $\lambda/2$ up to 4λ, with $\lambda/2$ step, $I_L \sim 5$ mW/cm^2 .

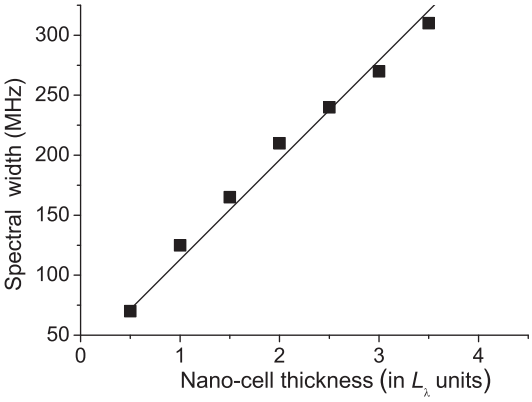

Figure 2.16: The spectral width of the fluorescence of the individual transition versus thickness L: squares - experiment, solid line - plotted by empiric formula.

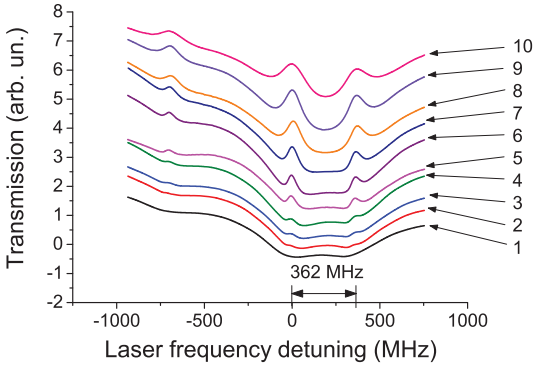

Figure 2.17: Transmission spectrum on Rb D_1 line obtained by nano-cell with $L = \lambda$ for different values of laser intensity. For the curves under number from 1 to 10 the corresponding laser intensities are: 0.15, 0.4, 1.1, 1.6, 4.5, 6.7, 18.3, 67.6, 102 and 267 mW/cm^2.

is seen, for this value of the laser intensity, there are no dips of reduced fluorescence up to $L = 2\lambda$. The dips appear when $L > 2\lambda$ and it is easy to explain that the dips formation is determined by the product $I_L \times L$. Thus, either keeping the intensity of I_L and increasing the length L, or keeping the length L and increasing the intensity I_L it is possible to form narrow dips of reduced fluorescence in the range of $\lambda - 10\lambda$. Note, that even at the largest thickness $L = 4\lambda$ (≈ 3.2 μm) the spectral width of the fluorescence is still sub-Doppler (i.e. < 500 MHz). The spectral width of the fluorescence of the individual transition as a function of the nano-cell thickness L is presented in fig. 2.16. For the correct spectral width measurement, a fitting with three Lorentzian curves has been provided and as example the case of $L = 2\lambda$ is presented in the inset on fig. 2.15 (three grey lines). The solid curve is plotted by the empiric formula: $\gamma_{FL}[\text{MHz}] = 30[\text{MHz}] + 83 \times L_\lambda$ (in $L_\lambda = L/\lambda$ units). Estimation by this empiric formula predicts that up to $L \sim 4.5$ μm the spectral width of the fluorescence is less than the Doppler one for a cm-size cell. Note, that linear (relatively weak) dependence of the γ_{FL} versus thickness L means that in the case of ± 20 nm accuracy of determination of the thickness $L \approx \lambda/2$ leads to additional spectral width broadening of several MHz. This relative insensitivity is important for the application of the thickness $L \approx \lambda/2$.

Let us for a while come back to fig. 1.7 the transmission spectrum on the same transitions is presented for the thickness $L = \lambda$ (lower curve). Obviously, the spectral width of the spectrum is much larger than in the case of $L = \lambda/2$, however the VSOP resonances appear exactly at the frequency positions of atomic transitions (the VSOP resonances are absent when the laser intensity is less than 0.1 mW/cm^2).

The line shape and magnitude of the transmission on $F_g = 3 \rightarrow F_e = 2, 3$ transitions of the ^{85}Rb D_1 line, obtained for thicknesses $L = \lambda$ for different values of laser intensity is shown in fig. 2.17. For the curves under number from 1 to 10 the corresponding laser intensities are: 0.15, 0.4, 1.1, 1.6, 4.5, 6.7, 18.3, 67.6, 102 and 267 mW/cm^2.

The spectral width of the transmission of the individual transition as a function of the laser intensity is presented in fig. 2.18. The solid curve is plotted by the empiric formula:

$\gamma_{FL}[\text{MHz}] = 12.3[\text{MHz}] \times (1 + 0.9 \times I[\text{mW/cm}^2])^{0.265}$. Following to the formula the value of γ_{FL} at $L = \lambda$, even at laser intensity ~ 10 W/cm^2, will not reach the Doppler spectral width of 500 MHz.

The peak amplitude of the transmission for the individual transition as a function of the laser intensity is presented in fig. 2.19. It is interesting to note that linear dependence for VSOP peaks in transmission spectra is observed up to ~ 7 mW/cm^2 and saturation effects are observed at ~ 100 mW/cm^2, meanwhile for an ordinary cm-size cell the saturation effects appear for the laser intensity of a several mW/cm^2 (a typical value is ~ 10 mW/cm^2). This is caused by the fact that as the size of the vapour cell is reduced, the lifetime of the ground-states becomes shorter because of collisions of the atoms with the cell windows, which cause transitions between the ground states.

2.3 Influence of cell temperature on spectra

The metal vapour pressure is determined by the temperature of the upper edge of the metallic column. In our experiments the temperature of the nano-cell is kept at $\sim 110 - 120$ °C on the side-arm, and $20 - 30$ °C higher at the windows (in order to prevent the Rb vapour condensation at the windows). This regime corresponds to the number density of Rb atoms $N \sim 10^{13}$ at/cm^3. The increasing of the cell side-arm temperature leads to an increasing of the number density of Rb atoms N and, as a result, to the increasing of the number of collisions between the investigated atoms. It is well known, that increasing of the collisions number induces additional line broadening and line frequency shift, red or blue shift depending on nature of the collisions [44]. The collision-induced additional line broadening is therefore often called pressure broadening. From pressure broadening and pressure shifts of spectral lines, information about collision processes and interatomic potentials can be extracted.

The frequency shift of atomic transition can be explained as follows: when an atom A with the energy levels E_i and E_k approaches another atom or molecule B, the energy levels of A are shifted because of the interaction between A and B (dipole-dipole interaction). This

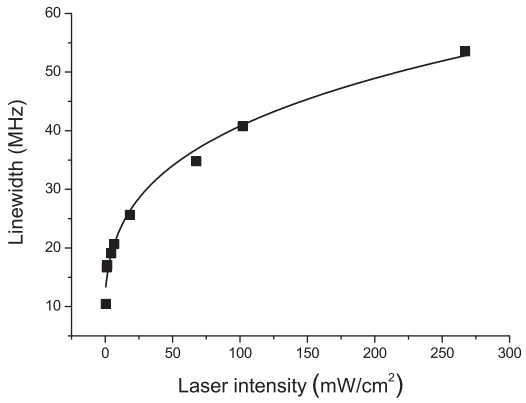

Figure 2.18: The spectral width of the transmission of the individual transition versus I_L: squares - experiment, solid line - plotted by empiric formula.

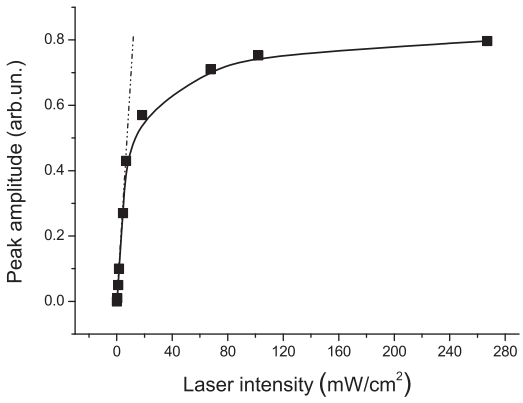

Figure 2.19: The peak amplitude of the transmission of the individual transition versus I_L: squares - experiment, solid line - plotted by empiric formula.

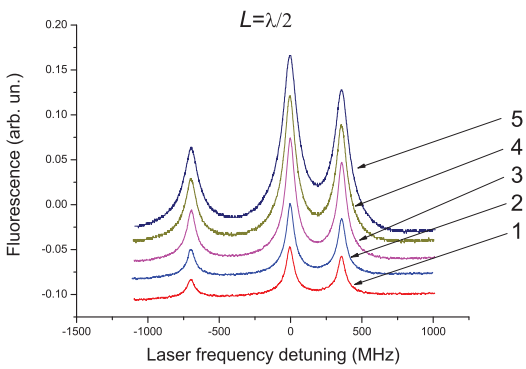

Figure 2.20: Fluorescence spectrum of nano-cell with $L = \lambda/2$ for different temperatures of the cell side-arm. For the curves 1 - 5, the corresponding temperatures are: 112, 134, 146, 158 and 170 °C.

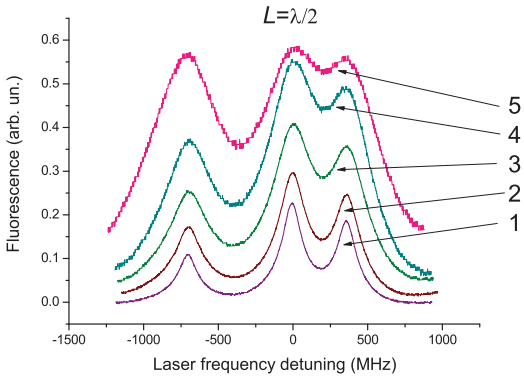

Figure 2.21: Fluorescence spectrum of nano-cell with $L = \lambda/2$ for different temperatures of the cell side-arm. For the curves 1 - 5, the corresponding temperatures are: 182, 194, 206, 218 and 230 °C.

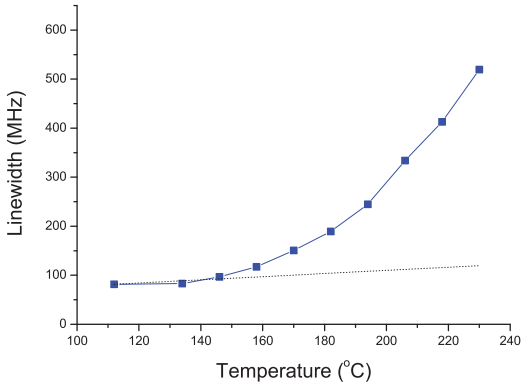

Figure 2.22: The spectral width of the fluorescence of the individual transition versus T_{SA}: experiment.

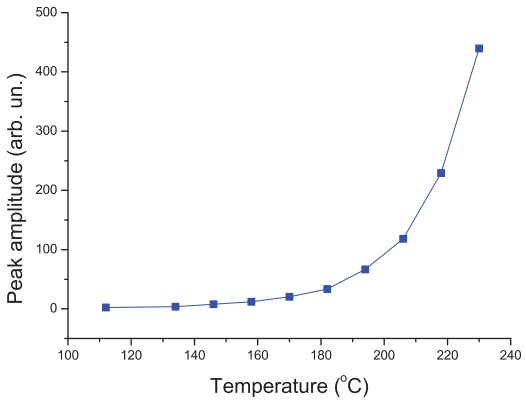

Figure 2.23: The peak amplitude of the fluorescence of the individual transition versus T_{SA}: experiment.

shift depends on the electron configurations of A and B and on the distance $R(A, B)$ between both collision partners, which is the distance between the centers of mass of A and B. The energy shifts ΔE are, in general, different for the levels E_i and E_k and may be positive as well as negative. The energy shift ΔE is positive if the interaction between A and B is repulsive, and negative if it is attractive [44].

The line broadening comes from two contributions: a) the phase shift, due to the frequency shift of the atomic transition during the collision; b) the quenching collisions which shorten the effective lifetime of the upper level.

Because of the long-range Coulomb interactions between charged particles (electrons and ions), pressure broadening and shift is particularly large in plasmas and gas discharges. This is of interest for gas discharge lasers, such as the HeNe laser or the argon-ion laser. The interaction between charged particles can be described by the linear and quadratic Stark effects. It can be shown that the linear Stark effect causes only line broadening, while the quadratic effect also leads to line shifts. The classical models used to explain collisional broadening and line shifts can be improved by using quantum mechanical calculations [44].

In the infrared and microwave ranges, collisions may sometimes cause a narrowing of the linewidth instead of a broadening (Dicke narrowing) [95]. This can be explained as follows: if the lifetime of the upper atomic level is long compared to the mean time between successive collisions, the velocity of the atoms is often altered by elastic collisions and the mean velocity component is smaller than without these collisions, resulting in a smaller Doppler shift. When the Doppler width is larger than the pressure-broadened width, this effect causes a narrowing of the Doppler-broadened lines, if the mean-free path is smaller than the wavelength of the molecular transition [96]. For higher pressures, the pressure broadening overcompensates the Dicke narrowing, and the linewidth increases again. There is a second effect that causes a collisional narrowing of spectral lines. In the case of very long lifetimes of levels connected, the linewidth is not determined by the lifetimes but by the diffusion time of the atoms out of the laser beam. Inserting a noble gas into the sample cell decreases the diffusion rate and therefore increases the interaction time of the sample atoms with the laser field,

which results in a decrease of the linewidth with pressure [97] until the pressure broadening overcompensates the narrowing effect.

Increasing of the active (sample) atoms (in our case the Rb atoms) leads to the broadening of the atomic transitions. The reason of this broadening is resonant collisions (Rb-Rb) and process called self-broadening [44, 98, 99]. For ordinary cell the broadening rate is equal to ~ 3.7 GHz/torr [44].

The line shape and magnitude of the resonant fluorescence on $F_g = 3 \rightarrow F_e = 2, 3$ transitions as a function of the nano-cell side-arm temperature T_{SA} which varies in the range of 112 up to 230 °C (with 12 °C step) for the laser intensity ~ 2 mW/cm^2 and temperature of the cell windows 270 °C is shown in fig. 2.20 for $T_{SA} = 112, 134, 146, 158$ and 170 °C; and in fig. 2.21 for $T_{SA} = 182, 194, 206, 218$ and 230 °C. The number density of Rb for this temperatures varies in the range $4.6 \cdot 10^{12} - 1.6 \cdot 10^{15}$ at/cm^3. From fig. 2.20, 2.21 it is seen the significant broadening of the spectra with increasing of the cell side-arm temperature.

The spectral width of the fluorescence of the individual transition as a function of the cell side-arm temperature is presented in fig. 2.22. For the correct spectral width measurement, a fitting with three Lorentzian curves has been provided. From fig. 2.22 it is seen that the spectral width achieves the Doppler-broadened profile at the temperature of the side-arm equal to 230 °C. Dotted line denotes broadening of the atomic line of spectra obtained with ordinary cell for rate of broadening equal to ~ 3.7 GHz/torr. From fig. 2.22 the one may conclude that self-broadening is much stronger for nano-cell in comparison with the ordinary cell.

The peak amplitude of the fluorescence of the individual transition as a function of the cell side-arm temperature is presented in fig. 2.23. The peak amplitude of the resonant fluorescence demonstrates strong increasing with increasing of the cell side-arm temperature.

It is important to note that for the case of $L = \lambda/2$, the atomic vapour density can be risen up to $10^{16} - 10^{17}$ at/cm^3 (this depends on atomic transition intensity), and the absorption will be still below 100% due to small value of L ("optically thin" absorption regime). This is simply determined by the product $N \times L$ (N is the atomic vapour number density), which is

relevant in absorption. This enables to study the broadening and shift of atomic transitions at very high atomic densities from transmission spectra recorded with the help of $L = \lambda/2$ nano-cell: the self-broadening and frequency shifts become pronounced at atomic vapour densities $> 10^{14}$ at/cm^3, when on-resonance D line absorption of atomic vapour in ordinary cm-size cells is in deep "optically thick" regime. This has been implemented in the work [98]. The frequency of laser diode radiation with $\sim$ 1 MHz spectral width was scanned in the vicinity of $5^2S_{1/2} - 6^2P_{3/2}$ blue transitions (λ = 420.2 nm) of ^{85}Rb and ^{87}Rb isotopes. A strong red shift of all the atomic transitions was detected at the temperature $T > 300$ °C ($N > 10^{16}$ at/cm^3). The examination of the fig. 2.22, 2.23 allows one to determine the optimal temperature regime in order to obtain narrow and detectible fluorescence spectra on the experiment. As it was mentioned the narrowest spectral width of the fluorescence is achieved when L is in the range $\lambda/4 < L < \lambda/2$, particularly for $L = \lambda/2$ achieves $\sim$ 70 MHz. In order to obtain linewidth close to the $\sim$ 70 MHz, the temperature of the cell side-arm should not exceed 130 °C.

2.4 Summary

1. We studied the influence of the Ne buffer gas on transmission and fluorescence spectra of a nano-cell. It is developed theoretical model describing the influence of a buffer gas. We represent comparison of theoretical data with experimental results for transmission and fluorescence spectra of a nano-cell for pressure of Ne equal to 6 torr and 20 torr. It is demonstrated that VSOP peaks are detectable for pressure of Ne up to 20 torr, meanwhile for SA spectra the addition of any buffer gas > 0.5 torr washes out VSOP and CO resonances. It is shown, that for any pressure of buffer gas, fluorescence spectra of a nano-cell is narrower that, the fluorescence spectra of an ordinary cell with the same pressure of buffer gas.

2. We studied the influence of laser intensity and nano-cell thickness on transmission and fluorescence spectra. It is demonstrated that fluorescence spectra of a nano-cell

has a sub-Doppler nature up to 250 mW/cm^2. It is interesting to note, that up to 50 mW/cm^2 there is a linear dependence of the fluorescence amplitude, meanwhile for an ordinary cell the saturation effects appear for the laser intensity of a several mW/cm^2. It is shown that the transmission spectra has a sub-Doppler nature up to intensities equal to 270 mW/cm^2 and the saturation effect of peak amplitude are observed at $\sim$ 100 mW/cm^2, meanwhile for ordinary cell the saturation effects appear for the laser intensity of several mW/cm^2. It is shown that fluorescence spectra demonstrate linear dependence of linewidth versus thickness L of a nano-cell and it is less that, the Doppler width up to thickness equal to $L \sim 4.5$ μm.

3. It is demonstrated that fluorescence spectra linewidth achieves Doppler-profile at the temperature of the side-arm equal to 230 °C. We found that in order to obtain linewidth of the fluorescence spectra close to $\sim$ 70 MHz, the temperature of the side-arm should not exceed 130 °C.

Chapter 3

Magneto-optical processes in nano-cell. Part I

Introduction. It is well known, that initially (in the absence of external field) each one of the levels of hyperfine structure is degenerated and the degeneracy is equal to $2F + 1$, with the angular momentum $\vec{F}$ defined as

$$\vec{F} = \vec{L} + \vec{S} + \vec{I} \tag{3.1}$$

where $\vec{L}$ is the orbital angular momentum, $\vec{S}$ is the spin momentum and $\vec{I}$ the nuclear spin momentum. Under the influence of an external magnetic field this degeneracy is broken. This degeneracy is broken due to the reason that atoms under the influence of external magnetic field undergo splitting and shift of their energy levels and changes in their transition intensities. These two last effects evaluated for various laser polarizations must be taken into account when one considers absorption profiles of alkali-metal D lines, which result from the contribution of many transitions influenced by the laser spectrum and the Doppler broadening. We have experimentally studied this interaction for external field from 0 to 10 000 gauss when the alkali vapour is confined in submicron thin vapour cell with thickness $L = \lambda/2$ and $L = \lambda$, λ being the laser wavelength.

The Hamiltonian describing the atomic system within a magnetic field B can be expressed

as the sum of the unperturbated atomic Hamiltonian and interaction Hamiltonian

$$H = H_0 + H_B, \tag{3.2}$$

where H_0 is the unperturbed Hamiltonian and H_B describes the interaction with magnetic field B. It can be represented as

$$H_B = -\frac{\mu_B B}{\hbar}(g_L L + g_S S + g_I I), \tag{3.3}$$

where μ_B is the Bohr magneton ($\mu_B = 1.399624$ MHz/G), g_L is the orbital Landé factor, g_S is the spin Landé factor and g_I is nuclear Landé factor [100].

The value for g_S has been measured very precisely, and the value is 2.0023193043622(15). The value for g_L is approximately 1, but to account for the finite nuclear mass, the quoted value is given by

$$g_L = 1 - \frac{m_e}{m_{nuc}}, \tag{3.4}$$

which is correct to lowest order in m_e/m_{nuc}, where m_e is the electron mass and m_{nuc} is the nuclear mass [101].

The nuclear factor g_I accounts for the entire complex structure of the nucleus, and so the quoted value is an experimental measurement [102].

The intensity of a transition, induced by the laser electric field is proportional to the square of the transfer coefficients modified by the presence of the magnetic field. Due to the mixing of states the strong nonlinearity of the transition intensities versus the external magnetic field intensity is observed.

3.1 The theoretical model considering interaction with a magnetic field

The so-called Dirac equation [103] for an electron to order v^2/c^2 is the starting point to

study the spectra of an atom within an electromagnetic field describes by the potentials $\vec{A}, V$

$$\left[\frac{1}{2m}(\vec{p}+\frac{e}{c}\vec{A})^2+\frac{e}{mc}\vec{S}.\vec{\nabla}\times\vec{A}-\frac{p^4}{8m^3c^2}-\frac{e\hbar}{8m^2c^2}\Delta V-\frac{e}{2m^2c^2}\vec{S}.(\vec{\nabla}V\times\vec{p})-eV\right]\Psi=E\Psi, \quad (3.5)$$

with $\vec{S}=\frac{\hbar}{2}\,\vec{\sigma}$ where $\vec{\sigma}=(\sigma_x,\sigma_y,\sigma_z)$, $\sigma_i(i=x,y,z)$ are the matrices of Pauli. For a potential $V=V(r)=\frac{Ze}{r}$, the term $-\frac{e}{2m^2c^2}\,\vec{S}.(\vec{\nabla}V\times\vec{p})$ describing the spin-orbit interaction is rewritten on a more compact form $H_{SO}=\xi(r)\vec{L}.\vec{S}$. It is worth to notice that this term leads naturally to calculate the Hamiltonian matrix in the basis $|n,L,J,F,m_F\rangle\equiv|F,m_F\rangle$ with $\vec{F}=\vec{I}+\vec{J}$ and $\vec{J}=\vec{L}+\vec{S}$. Thus for the Zeeman interaction, defined by $H_Z=-\vec{\mu_L}.\vec{B}-\vec{\mu_S}.\vec{B}-\vec{\mu_I}.\vec{B}$ with $\vec{\mu_L}=-\frac{g_L\beta}{\hbar}\vec{L}$ the magnetic orbital momentum, $\vec{\mu_S}=-\frac{2\beta}{\hbar}\vec{S}$ the magnetic moment of spin $\vec{S}$ and $\vec{\mu_I}=-\frac{g_I\beta}{\hbar}\vec{I}$ the magnetic moment of the nuclear spin $\vec{I}$ where $\beta=\frac{e\hbar}{2mc}$ is the Bohr magneton, the basis $|F,m_F\rangle$ can be chosen as a good basis to the first order if the condition $E_Z << E_{SO}$ is fulfilled (E_Z and E_{SO} are (resp.) eigenenergies of H_Z and H_{SO}). For the magnetic field considered in calculations, this condition is respected as the magnetic field will vary from 0 to 10^4 G. One should note that all the previous discussion is valid for a magnetic field $\vec{B}$ supposed uniform ($\vec{A}=\frac{1}{2}(\vec{B}\times\vec{r})$), which is what we have supposed in the development of the Zeeman interaction. Interaction of atoms with laser radiation field in such cells is strictly anisotropic and longitudinal size of the nano-cell being nanometric, one may consider this hypothesis of uniformity as valid. We shall see that indeed, in spite of strong inhomogeneity of B-field (in our case it can reach 150 G/mm), due to small thickness of the atomic vapour column inside nano-cell, numerical calculations based on our previous assumption are in accordance with experimental measurements.

The Hamiltonian of interaction $H_Z=-\vec{\mu_L}.\vec{B}-\vec{\mu_S}.\vec{B}-\vec{\mu_I}.\vec{B}$ may be expanded using different forms [103–107], we chose a formulation [104] which leads to

$$H_B=-\frac{\mu_B B}{\hbar}(g_L L+g_S S+g_I I) \quad (3.6)$$

where g_L, g_S and g_I are respectively the orbital, spin and the nuclear Landé factor.

We adopt a matrix representation in the coupled basis, that is, the basis of the unperturbated atomic state vectors $|n, L, J, F, m_F\rangle \equiv |F, m_F\rangle$ to evaluate the matrix elements of the Hamiltonian (3.6). In this basis one obtain the following relation for the matrix elements

$$\begin{aligned}\left\langle F, m_F|H_B|\tilde{F}, m_{\tilde{F}}\right\rangle = \left\langle IJF, m_F|H_B|I\tilde{J}\tilde{F}, m_{\tilde{F}}\right\rangle = \\ (\mu_B B)\delta(J, \tilde{J})\delta(m_F, m_{\tilde{F}})g_J(-1)^{I+J+m_{\tilde{F}}+1}\sqrt{J(J+1)}\times \\ \sqrt{(2J+1)}\sqrt{2F+1}\sqrt{2\tilde{F}+1}\begin{pmatrix} F & 1 & \tilde{F} \\ -m_F & 0 & m_{\tilde{F}} \end{pmatrix}\begin{Bmatrix} J & 1 & \tilde{J} \\ \tilde{F} & I & F \end{Bmatrix},\end{aligned} \tag{3.7}$$

where the parenthesis and curly brackets denote respectively the $3j$ and $6j$-symbols.

Using the relations given in [108], we may expand the $3j$ and $6j$-symbols and thus express in a more convenient way for a computational task, the diagonal and off-diagonal matrix element (3.7). In this basis, the diagonal matrix elements are given by

$$\langle F, m_F|H_B|F, m_F\rangle = E_0(F) + \mu_B g_F m_F B, \tag{3.8}$$

where $E_0\,(F)$ is the initial energy [109] of the sub-level $|n, L, J, F, m_F\rangle \equiv |F, m_F\rangle$ and g_F is the effective Landé factor [109].

The non-zero off-diagonal matrix elements verify the following selection rules $\Delta L = 0, \Delta J = 0, \Delta F = \pm 1, \Delta m_F = 0$:

$$\begin{aligned}\langle F-1, m_F|H|F, m_F\rangle = \langle F, m_F|H|F-1, m_F\rangle = -\frac{\mu_B B}{2}(g_J - g_I)\times \\ \left(\frac{[(J+I+1)^2 - F^2][F^2 - (J-I)^2]}{F}\right)^{1/2}\left(\frac{F^2 - m_F^2}{F(2F+1)(2F-1)}\right)^{1/2}.\end{aligned} \tag{3.9}$$

The Hamiltonian matrix is then block diagonal where each block corresponds to a given value of m_F. The diagonalization of the Hamiltonian matrix allows one to find the eigenvectors and the eigenvalues, that is to determine the eigenvalues corresponding to the energies of Zeeman sub-levels and the new states vectors which can be expressed in terms of the initial

unperturbed atomic state vectors,

$$|\Psi(F_e, m_e)\rangle = \sum_{F'_e} \alpha^e_{F_e F'_e}(B, m_e)|F'_e, m_e\rangle \tag{3.10}$$

and

$$|\Psi(F_g, m_g)\rangle = \sum_{F'_g} \alpha^g_{F_g F'_g}(B, m_g)|F'_g, m_g\rangle. \tag{3.11}$$

The state vectors $|F'_e, m_e\rangle$ and $\left|F'_g, m_g\right\rangle$ are the unperturbated state vectors, respectively, for the excited and the ground states. The coefficients $\alpha^e_{F_e F'_e}(B, m_e)$ and $\alpha^g_{F_g F'_g}(B, m_g)$ are mixing coefficients, respectively, for the excited and the ground states; they depend on the field strength and magnetic quantum numbers m_g or m_e. One obtain these mixing coefficients by diagonalizing the Hamiltonian of the considered system.

Diagonalization of the Hamiltonian matrix for alkali metals, in case of different polarization of the exciting radiation, allows to obtain the shift of position of the energy levels in presence of external magnetic field.

The intensity of a transition, induced by the interaction of the atomic electric dipole and the oscillating laser electric field is proportional to the spontaneous emission rate of the associated transition A_{eg}, that is, to the square of the dipole momentum modified by the presence of the magnetic field

$$W_{eg} \propto A_{eg} \propto \left(\left\langle \Psi(F_e, m_e)|r^1_q|\Psi(F_g, m_g)\right\rangle\right)^2, \tag{3.12}$$

Specially, $\left\langle \Psi(F_e, m_e)|r^1_q|\Psi(F_g, m_g)\right\rangle$ denotes the matrix element that couples the two hyperfine sublevels $|\Psi(F_e, m_e)\rangle$ and $|\Psi(F_g, m_g)\rangle$ (where e refer to the excited states and g refer to the ground states). Taking into account expressions (3.10) and (3.11) for the state vectors, dipole momentum (all α coefficients are real) can be evaluated to

$$\left\langle \Psi(F_e, m_e)|r^1_q|\Psi(F_g, m_g)\right\rangle = \sum_{F'_e F'_g} \alpha^e_{F_e F'_e}(B) \left\langle F'_e, m_e|r^1_q|F'_g, m_g\right\rangle \alpha^g_{F_g F'_g}(B), \tag{3.13}$$

where the primed quantum numbers refer to the unperturbed states and the unprimed quantum numbers refer to the new states. To calculate these matrix elements, it is useful to factor out the angular dependence and write the matrix element as a product of a Clebsch-Gordan coefficient and a reduced matrix element, using the Wigner-Eckart theorem [110]

$$\left\langle F_e, m_e | r^1_q | F_g, m_g \right\rangle = \langle F_g \; m_g, 1 \; q | F_e, m_e \rangle \, \langle F_e || r || F_g \rangle \, . \tag{3.14}$$

Here, q ($q = -1, 0, +1$) is an index labeling the component of r in the spherical basis, and the doubled bars indicate that the matrix element is reduced. We can also write (3.14) in terms of a Wigner $3j$ symbol as:

$$\left\langle F_e, m_e | r^1_q | F_g, m_g \right\rangle = (-1)^{F_g - m_e} \sqrt{(2F_e + 1)} \begin{pmatrix} F_g & 1 & F_e \\ m_g & q & -m_e \end{pmatrix} \langle F_e || r || F_g \rangle \, . \tag{3.15}$$

The $3j$ symbol (or, equivalently, the Clebsch-Gordan coefficient) vanishes unless the sublevels satisfy $m_e = m_g + q$. The reduced matrix element of rhs of (3.15) can be further simplified by factoring out the F_e and F_g dependence into a Wigner $6j$ symbol, leaving a further reduced matrix element that depends only on the L, S, and J quantum numbers [110]:

$$\begin{aligned} \langle F_e || r || F_g \rangle = \; & \langle J_e \; I, F_e || r || J_g \; I, F_g \rangle = \\ & (-1)^{F_e + J_e + I + 1} \sqrt{(2F_g + 1)(2J_e + 1)} \begin{Bmatrix} F_e & 1 & F_g \\ J_g & I & J_e \end{Bmatrix} \langle J_e || r || J_g \rangle \, . \end{aligned} \tag{3.16}$$

Let us demonstrate this property. The tensor operators $V^{k_1}_{q_1}$ and $W^{k_2}_{q_2}$ are supposed to act on independent kets of variable in space H_1 and H_2 and consequently we are considering operators $V^{k_1}_{q_1}$ and $W^{k_2}_{q_2}$ here:

$$T^k_q = \left[V^{k_1} \times W^{k_2} \right]^k_q = \sum_{q_1 = -k_1}^{k_1} \sum_{q_2 = -k_2}^{k_2} \langle k_1 q_1, k_2 q_2 | k q \rangle \, V^{k_1}_{q_1} W^{k_2}_{q_2} . \tag{3.17}$$

We want now to evaluate the matrix element:

$$\left\langle j_1\ j_2\ J\ m|T^k_q|j'_1\ j'_2\ J'\ m'\right\rangle . \tag{3.18}$$

According to the Wigner-Eckart theorem one obtain:

$$\begin{aligned}\left\langle j_1\ j_2\ J\ m|T^k_q|j'_1\ j'_2\ J'\ m'\right\rangle &= \langle J'\ m'\ k\ q|J\ m\rangle \left\langle j_1\ j_2\ J||T^k||j'_1\ j'_2\ J'\right\rangle = \\ &= (-1)^{J'-k+m}\sqrt{2J+1}\begin{pmatrix} J' & k & J \\ m' & q & -m \end{pmatrix}\left\langle j_1\ j_2\ J||T^k||j'_1 j'_2 J'\right\rangle .\end{aligned} \tag{3.19}$$

Let rewrite (3.18) using (3.19)

$$\begin{aligned}\left\langle j_1\ j_2\ J\ m|T^k_q|j'_1\ j'_2\ J'\ m'\right\rangle = \sum_{\{q_1,q_2\}}(-1)^{k_1-k_2+q}\sqrt{2k+1}\begin{pmatrix} k_1 & k_2 & k \\ q_1 & q_2 & -q \end{pmatrix}\times \\ \left\langle j_1\ j_2\ J\ m|V^{k_1}_{q_1}W^{k_2}_{q_2}|j'_1\ j'_2\ J'\ m'\right\rangle .\end{aligned} \tag{3.20}$$

But $|j_1 j_2 J m\rangle$ and $|j'_1\ j'_2\ J'\ m'\rangle$ denote two coupled states and each of them is built from two non-coupled components: for the first one $|j_1\ m_1\rangle$ and $|j_2\ m_2\rangle$ and for the second one $|j'_1\ m'_1\rangle$ and $|j'_2\ m'_2\rangle$. So it means, that coupled states can be expressed by the use of $3j$-symbols and we obtain:

$$|j_1\ j_2\ J\ m\rangle = \sum_{\{m_1,m_2\}}(-1)^{j_1-j_2+m}\sqrt{2J+1}\begin{pmatrix} j_1 & j_2 & J \\ m_1 & m_2 & -m \end{pmatrix}|j_1\ m_1\rangle\,|j_2\ m_2\rangle \tag{3.21}$$

$$|j'_1\ j'_2\ J'\ m'\rangle = \sum_{\{m'_1,m'_2\}}(-1)^{j'_1-j'_2+m'}\sqrt{2J'+1}\begin{pmatrix} j'_1 & j'_2 & J' \\ m'_1 & m'_2 & -m' \end{pmatrix}|j'_1\ m'_1\rangle\,|j'_2\ m'_2\rangle \tag{3.22}$$

We rewrite Eq. (3.20) using (3.21) and (3.22):

$$\left\langle j_1\ j_2\ J\ m|T^k_q|j'_1\ j'_2\ J'\ m'\right\rangle = \sum_{\{q_1,q_2\}}\sum_{\{m_1,m_2\}}\sum_{\{m'_1,m'_2\}}(-1)^{k_1-k_2+q}\sqrt{2k+1}\begin{pmatrix} k_1 & k_2 & k \\ q_1 & q_2 & -q\end{pmatrix}\times$$

$$(-1)^{j_1-j_2+m}\sqrt{2J+1}\begin{pmatrix} j_1 & j_2 & J \\ m_1 & m_2 & -m\end{pmatrix}\times(-1)^{j'_1-j'_2+m'}\sqrt{2J'+1}\begin{pmatrix} j'_1 & j'_2 & J' \\ m'_1 & m'_2 & -m'\end{pmatrix}\times$$

$$\left\langle j_1\ m_1\right|\left\langle j_2\ m_2\right|V^{k_1}_{q_1}W^{k_2}_{q_2}\left|j'_1\ m'_1\right\rangle\left|j'_2\ m'_2\right\rangle = \tag{3.23}$$

$$\sum_{\{q_1,q_2\}}\sum_{\{m_1,m_2\}}\sum_{\{m'_1,m'_2\}}(-1)^{k_1-k_2+q+j_1-j_2+m+j'_1-j'_2+m'}\sqrt{(2k+1)(2J+1)(2J'+1)}$$

$$\begin{pmatrix} k_1 & k_2 & k \\ q_1 & q_2 & -q\end{pmatrix}\begin{pmatrix} j_1 & j_2 & J \\ m_1 & m_2 & -m\end{pmatrix}\begin{pmatrix} j'_1 & j'_2 & J' \\ m'_1 & m'_2 & -m'\end{pmatrix}\times$$

$$\left\langle j_1\ m_1\right|V^{k_1}_{q_1}\left|j'_1\ m'_1\right\rangle\left\langle j_2\ m_2\right|W^{k_2}_{q_2}\left|j'_2\ m'_2\right\rangle$$

as indeed $V^{k_1}_{q_1}$ acts only on kets $|j_1\ m_1\rangle$ and doesn't act on the kets $|j_2\ m_2\rangle$ (same for $W^{k_2}_{q_2}$ and kets $|j_2\ m_2\rangle$).

$$\left\langle j_1\ j_2\ J\ m\right|T^k_q\left|j'_1\ j'_2\ J'\ m'\right\rangle =$$

$$\sum_{\{q_1,q_2\}}\sum_{\{m_1,m_2\}}\sum_{\{m'_1,m'_2\}}(-1)^{k_1-k_2+q+j_1-j_2+m+j'_1-j'_2+m'+j'_1-k_1+m_1+j'_2-k_2+m_2}\times$$

$$\sqrt{(2k+1)(2J+1)(2J'+1)(2j_1+1)(2j_2+1)}\begin{pmatrix} k_1 & k_2 & k \\ q_1 & q_2 & -q\end{pmatrix}\begin{pmatrix} j_1 & j_2 & J \\ m_1 & m_2 & -m\end{pmatrix}\times \tag{3.24}$$

$$\begin{pmatrix} j'_1 & j'_2 & J' \\ m'_1 & m'_2 & -m'\end{pmatrix}\begin{pmatrix} j'_1 & k_1 & j_1 \\ m'_1 & q_1 & -m_1\end{pmatrix}\begin{pmatrix} j'_2 & k_2 & j_2 \\ m'_2 & q_2 & -m_2\end{pmatrix}\left\langle j_1\right|V^{k_1}\left|j'_1\right\rangle\left\langle j_2\right|W^{k_2}\left|j'_2\right\rangle$$

We apply again Wigner-Eckart theorem to the two last terms of (3.23). Due to the reason that (3.19) and (3.24) represent the same matrix element, we equate them and multiply both sides by $\dfrac{1}{(-1)^{J'-k+m}}\begin{pmatrix} J' & k & J \\ m' & q & -m\end{pmatrix}$ and sum over m, m' and q. With help of relation

$$\sum_{\{m_1,m_2,m_3\}} \begin{pmatrix} j_1 & j_2 & j_3 \\ m_1 & m_2 & m_3 \end{pmatrix} \begin{pmatrix} j_1 & j_2 & j_3 \\ m_1 & m_2 & m_3 \end{pmatrix} = 1 \tag{3.25}$$

we obtain

$$\begin{aligned} \langle j_1\ j_2\ J||T^k||j_1'\ j_2'\ J'\rangle = & \sum_{\{m,m',q\}} \sum_{\{q_1,q_2\}} \sum_{\{m_1,m_2\}} \sum_{\{m_1',m_2'\}} (-1)^{k_1-k_2+j_1'-j_2'+j+q+m'-m_1-m_2} \times \\ & \sqrt{(2k+1)(2J'+1)(2j_1+1)(2j_2+1)} \begin{pmatrix} J' & k & J \\ m' & q & -m \end{pmatrix} \begin{pmatrix} k_1 & k_2 & k \\ q_1 & q_2 & -q \end{pmatrix} \times \\ & \begin{pmatrix} j_1 & j_2 & J \\ m_1 & m_2 & -m \end{pmatrix} \begin{pmatrix} j_1' & j_2' & J' \\ m_1' & m_2' & -m' \end{pmatrix} \begin{pmatrix} j_1' & k_1 & j_1 \\ m_1' & q_1 & -m_1 \end{pmatrix} \begin{pmatrix} j_2' & k_2 & j_2 \\ m_2' & q_2 & -m_2 \end{pmatrix} \times \\ & \langle j_1|\, V^{k_1}\, |j_1'\rangle\, \langle j_2|\, W^{k_2}\, |j_2'\rangle \end{aligned} \tag{3.26}$$

We have a sum over six $3j$-symbols and we can distinct a $9j$-symbol. Using the symmetries of the $3j$-symbols to remove the phase factor, we obtain the result

$$\begin{aligned} \langle j_1\ j_2 J\ ||\ T^k\ ||\ j_1'\ j_2'\ J'\rangle = & \sqrt{(2k+1)(2J'+1)(2j_1+1)(2j_2+1)} \begin{Bmatrix} j_1 & j_1' & k_1 \\ j_2 & j_2' & k_2 \\ J & J' & k \end{Bmatrix} \times \\ & \langle j_1|\, V^{k_1}\, |j_1'\rangle\, \langle j_2|\, W^{k_2}\, |j_2'\rangle \end{aligned} \tag{3.27}$$

In particular, let us examine the case of $k_2 = 0$. Putting $k_2 = 0$ into the $9j$-symbol of Eq. (3.27) causes it to vanishing unless $j_2 = j_2'$ and $k_1 = k$. By putting $k_2 = 0$ in Eq. (3.27), we find that the $9j$-symbol collapses to a $6j$-symbol. Here we are using the following property of $9j$-symbol:

$$\left\{ \begin{array}{ccc} j_1 & j_2 & j_3 \\ j_4 & j_5 & j_6 \\ j_7 & j_8 & 0 \end{array} \right\} = (-1)^{j_2+j_3+j_4+j_7}[(2j_3+1)(2j_7+1)]^{-\frac{1}{2}} \left\{ \begin{array}{ccc} j_1 & j_2 & j_3 \\ j_5 & j_4 & j_7 \end{array} \right\} \delta_{j_3 j_6}\ \delta_{j_7 j_8} \quad (3.28)$$

Now we can make changes in (3.27) according to the property (3.28)

$$\begin{aligned} &\left\langle j_1\ j_2\ J \,||\, T^k \,||\, j_1'\ j_2'\ J' \right\rangle = \\ =&\sqrt{(2k+1)(2J'+1)(2j_1+1)(2j_2+1)} \left\{ \begin{array}{ccc} j_1 & j_1' & k \\ j_2 & j_2 & 0 \\ J & J' & k \end{array} \right\} \langle j_1 | \, V^{k_1} \, | j_1' \rangle = \\ =&\ (-1)^{j_1+j_2+J'+k}\sqrt{(2k+1)(2J'+1)(2j_1+1)(2j_2+1)}\times \\ &[(2j_2+1)(2k+1)]^{-\frac{1}{2}} \left\{ \begin{array}{ccc} j_1 & j_1' & k \\ J' & J & j_2 \end{array} \right\} \langle j_1 | \, V^{k_1} \, | j_1' \rangle = \\ =&\ (-1)^{j_1+j_2+J'+k}\sqrt{(2J'+1)(2j_1+1)} \left\{ \begin{array}{ccc} j_1 & j_1' & k \\ J' & J & j_2 \end{array} \right\} \langle j_1 | \, V^{k_1} \, | j_1' \rangle \end{aligned} \quad (3.29)$$

Thus, we found that rme expressed in the coupled basis, can be described as a product of a me in the uncoupled basis by $6j$-symbol. Using invariance of $6j$-symbol under the permutation of any two columns and invariance to interchange of upper and lower arguments in any two columns the one obtain the final relation expressed in following way:

$$\begin{aligned} &\left\langle j_1\ j_2\ J \,||\, T^k \,||\, j_1'\ j_2'\ J' \right\rangle = \\ &= (-1)^{j_1+j_2+j'+k}\sqrt{(2J'+1)(2j_1+1)} \left\{ \begin{array}{ccc} J & k & J' \\ j_1' & j_2 & j_1 \end{array} \right\} \langle j_1 | \, T^k \, | j_1' \rangle \end{aligned} \quad (3.30)$$

According to relation (3.30) one obtain relation (3.16) taking into account that for the dipole operator r^k the rank of the operator k is equal to one ($k = 1$). The numerical

value of the $\langle J_e||r||J_g\rangle$ matrix elements are preserved while calculating dipole momentum for transitions among D_1 or D_2 lines. Thus the calculation of transition intensity is equivalent to the calculation of the transfer coefficients:

$$W_{eg} \propto A_{eg} \propto a^2 \left[\Psi(F_e, m_e); \Psi(F_g, m_g); q\right], \tag{3.31}$$

The transfer coefficients are expressed as

$$a\left[\Psi(F_e, m_e); \Psi(F_g, m_g); q\right] = \sum_{F_e' F_g'} \alpha^e_{F_e F_e'}(B) a\left(\Psi(F_e, m_e); \Psi(F_g, m_g); q\right) \alpha^g_{F_g F_g'}(B), \tag{3.32}$$

where the unperturbated transfer coefficients have the following definition

$$\begin{aligned} &a\left(\Psi(F_e, m_e); \Psi(F_g, m_g); q\right) = (-1)^{1+I+J_e+F_e+F_g-m_e} \\ &\times\sqrt{2J_e+1}\sqrt{2F_e+1}\sqrt{2F_g+1} \begin{pmatrix} F_e & 1 & F_g \\ -m_e & q & m_g \end{pmatrix} \begin{Bmatrix} F_e & 1 & F_g \\ J_g & I & J_e \end{Bmatrix}, \end{aligned} \tag{3.33}$$

the parenthesis and curly brackets denote, respectively, the $3j$ and $6j$ symbols, g and e point respectively ground and excited states.

Formulas $(3.7 - 3.33)$ have been used to calculate the frequency shifts and modification of intensities for the corresponding transitions.

3.2 Computational model

In the previous section we considered the theoretical model used for the calculation of the transitions frequency shifts in respect to their initial positions and the modification of the transition intensities. The mixing of states of the unperturbed atomic system induces these changes. It was mentioned, that using formulas $(3.7 - 3.33)$ one may calculate the frequency shifts and modification of intensities for the corresponding transitions for some certain polarization of the exciting laser radiation. We calculated the shift and intensity modification in the range of magnetic field from 0 to 10 000 gauss with step 0.1 gauss. As a result, being of

interest for us, we calculated physical quantities for 100 000 values of B. We should mention, that the considered systems contain large number of states, thus it is a highly recurrent task to calculate all these physical quantities. For example, ^{87}Rb in optical branch has 8 hyperfine states, which are degenerated by magnetic momentum (Zeeman sublevels) and degeneracy degree is equal to $2F+1$ for each hyperfine state. As a result, for ^{87}Rb the number of Zeeman sublevels is equal to 32 (8 (for $5^2S_{1/2}$) + 8 (for $5^2P_{1/2}$) + 16 (for $5^2P_{3/2}$) = 32). It means one should calculate 32 energy values and 32 state vectors containing 32 components and make all mathematical operations 100 000 times.

The computational model was developed for the calculation of the transitions frequency shifts in respect to initial positions and transitions intensity modification for all range of considered magnetic field. Fig. 3.1 shows the block scheme of the used computer code. The code was developed in such a way, that it is possible to use it for all alkali metals.

In a first step input data are the characteristics of the atomic system for which the calculation should be done. More precisely input data are: frequency distance between the atomic states of the hyperfine structure, nuclear magnetic angular momentum I, which is different for different alkali atoms and isotopes, the Landé factors [102], the polarization of the exciting laser radiation and the maximal value of the magnetic field B.

Then, next step the program construct the Hamiltonian of the system. Computational algorithm is based on principles of the quantum summation over quantum angular momenta (respect of the triangular relation) and the use of relations (3.8) and (3.9) with corresponding selection rules. The Hamiltonian has a block-diagonal structure. Structure of the Hamiltonian for optical domain of alkali metals is represented on fig. 3.2. Elements in the blocks are determined by the relations (3.8) and (3.9). All other elements are equal to zero. First block describes the interaction between ground states $S_{1/2}$ of the atomic system. Second block corresponds to the excited stated $P_{1/2}$ and third block to the excited states $P_{3/2}$.

On the third step the program diagonalizes the Hamiltonian in order to determine the eigenvectors and eigenvalues of the atomic system. From mathematical point of view the process of diagonalization of the Hamiltonian matrix H is equivalent to the unitary

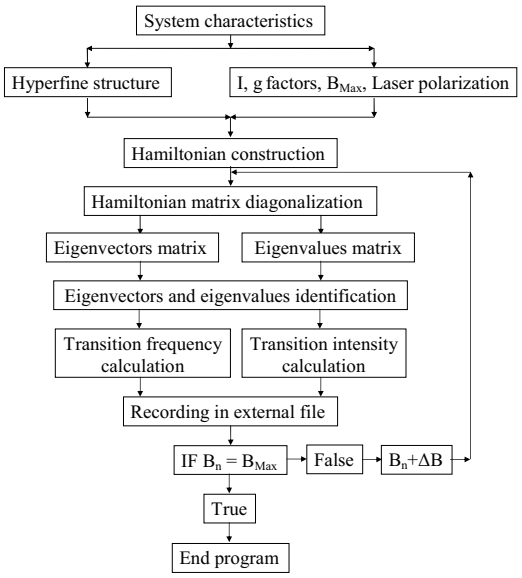

Figure 3.1: Block scheme of computer program calculating transitions frequency shift and transition intensity modification.

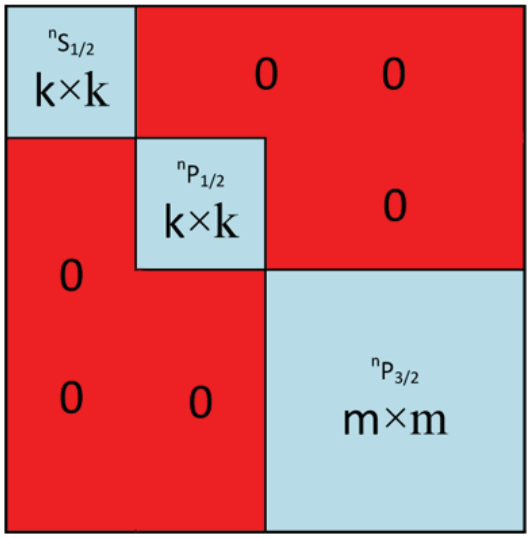

Figure 3.2: Structure of the Hamiltonian for optical domain of alkali metals.

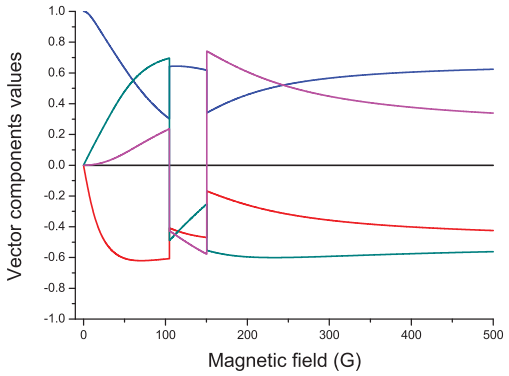

(a) The eigenvector components before identification.

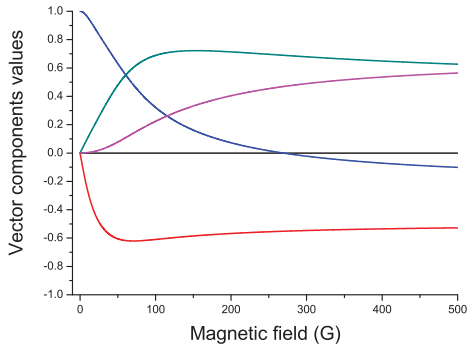

(b) The eigenvector components after identification.

Figure 3.3: The components of eigenvector calculated by computational program.

transformation

$$H = V^T U\ V \tag{3.34}$$

where U denotes the diagonal matrix containing eigenvalues of the Hamiltonian and V is the matrix of the eigenvectors of the Hamiltonian. V^T denotes the conjugate transpose of the matrix V. Eigenvalues of the Hamiltonian matrix can be obtained from equation

$$det\,|H - \lambda I| = 0 \tag{3.35}$$

where λ is a eigenvalue of an H and I denotes the unit matrix. Solving equation (3.35) can be represented in a matrix form as follow

$$det \begin{vmatrix} H_{11} - \lambda & H_{12} & ... & H_{1n} \\ H_{21} & H_{22} - \lambda & ... & H_{2n} \\ . & . & . & . \\ . & . & . & . \\ . & . & . & . \\ H_{n1} & H_{n2} & ... & H_{nn} - \lambda \end{vmatrix} = 0. \tag{3.36}$$

Solving equation (3.36) one may find all non-trivial solutions of the system, i.e. all eigenvalues of the Hamiltonian matrix. The eigenvectors of the Hamiltonian can be found from relation

$$H\Psi_i = \lambda_i \Psi_i \tag{3.37}$$

where λ_i denotes the ith eigenvalue and Ψ_i is the eigenvector corresponding to λ_i.

In the computer model, we used Gaussian diagonalization algorithm. This algorithm allows one to obtain in one cycle all eigenvalues and eigenvector for a given value of the magnetic field.

Due to the interaction with the magnetic field, Zeeman sublevels undergoes strong shift in respect to the initial position. This leads to Zeeman sublevels crossings and these crossings

degenerate the Hamiltonian matrix. Degeneration means that several eigenvalues get equal values and it is difficult to distinguish eigenvectors from each other. On fig. 3.3(a) are demonstrated the evolution of components for one of the eigenvectors as a function of the magnetic field B. One may see that curves are not smooth and continuous, that means that the code mixed eigenvectors for some values of magnetic field [5]. In order to identify eigenvectors a function is implemented in the code as explained here after.

In the fourth step the program identifies eigenvectors and eigenvalues. On fig. 3.3(b) are shown the components of the same eigenvector as a function of magnetic field B. As it is seen on the figure, the curves are continuous. To create the algorithm of the function, we assume that variation of the eigenvectors and eigenvalues as a function of the magnetic field should be smooth and uninterrupted function. It means that the variation of the derivative of the function for each value of the magnetic field should not outnumber some infinitesimal quantity. From computational point of view this variation of one step of program, should be enough small. Thus algorithm of function calculates left and right derivatives for each value of the magnetic field and this allows to identify eigenvalues and eigenvectors of the system.

During the fifth step, the program calculates shifts, and using relations (3.32) and (3.33), calculates intensities modification for all possible transitions of the system according to the selection rules. Selection rules of transition are determined by the polarization of the exciting laser radiation.

Further program records all calculated values in an external file and verifies current value of the magnetic field. If current value of the magnetic field is equal to the maximal value, the program stops execution of the algorithm. In opposite case, the program increases value of the magnetic field of $\Delta B = 0.1$ G and returns to the execution as indicated on fig. 3.1.

3.3 Consideration of the theoretical calculations

3.3.1 ^{87}Rb D_1 line transitions from the ground states $F_g = 1, 2$

The diagram of the energy levels for ^{87}Rb D_1 line transitions is demonstrated of fig. 1.4.

Taking into account the degeneracy of hyperfine levels, the diagram of the energy levels has a more complicated structure. The number of Zeeman sublevels for ground states $F_g = 1, 2$ is equal to 8 (3 Zeeman sublevels for $F_g = 1$ and 5 sublevels for $F_g = 2$) and 8 sublevels for excited states $F_e = 1, 2$ (analogically with ground states).

We calculated frequency shifts and intensity modifications for all possible transitions between the ground and excited states for σ^+, π and σ^- polarizations of the exciting laser radiation. On fig. 3.4, 3.5 and 3.6 are exhibited the result of the calculation made for ^{87}Rb D_1 line transitions from the ground states $F_g = 1, 2$ respectively for σ^+, π and σ^- polarizations of the exciting laser radiation.

The allowed transitions between magnetic sublevels of hyperfine states for the ^{87}Rb, D_1 line from ground states $F_g = 1, 2$ in the case of σ^+ (left circular) polarized excitation and selection rules $\Delta m_F = +1$ are depicted respectively on fig. 3.4(e) and fig. 3.4(f). As it is seen from these diagrams, there are allowed 5 transitions from $F_g = 1$ and 7 transitions from $F_g = 2$.

The frequency shifts of these transitions are shown on fig. 3.4(a) and fig. 3.4(b) respectively for $F_g = 1$ and $F_g = 2$. The numbering of the curves on the figure corresponds to the numbering of the transitions on the diagrams as exhibited on fig. 3.4(e) and fig. 3.4(f). From fig. 3.4(a) and fig. 3.4(b) it is seen that under the influence of external magnetic field, the transitions between Zeeman sublevels undergo strong frequency shift in respect to their initial value. These shifts of the transition are conditioned by strong shift of the Zeeman sublevels in respect to the initial positions, which exceeds the frequency distance between hyperfine levels and may achieve tens of GHz.

On fig. 3.4(c) and fig. 3.4(d) are demonstrated transitions intensity modification respectively for $F_g = 1$ and $F_g = 2$.

As it is seen from fig. 3.4(c), amplitudes of the transition 1 and 3 on the diagram 3.4(e) decrease very fast with increasing of the magnetic field and for a magnitude of the magnetic field equals to 2000 G is close to zero. Though, amplitudes of the transitions 2, 4 and 5 increase with increasing of magnetic field and asymptotically tend to the same value.

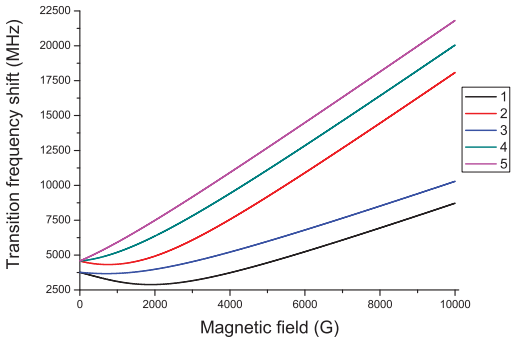

(a) The transitions frequency shift versus magnetic field, ground state $F_g = 1$.

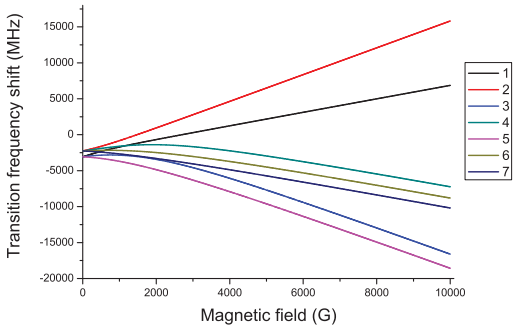

(b) The transitions frequency shift versus magnetic field, ground state $F_g = 2$.

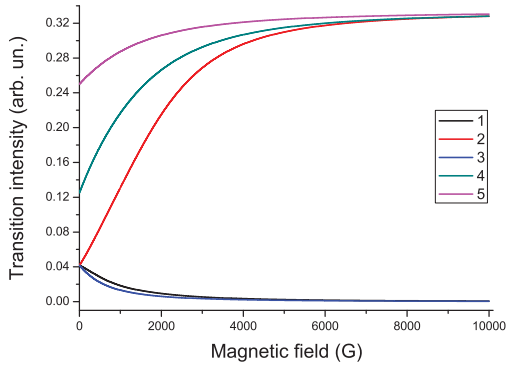

(c) The transitions intensity versus magnetic field, ground state $F_g = 1$.

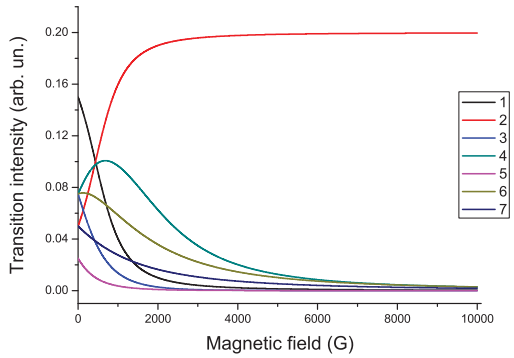

(d) The transitions intensity versus magnetic field, ground state $F_g = 2$.

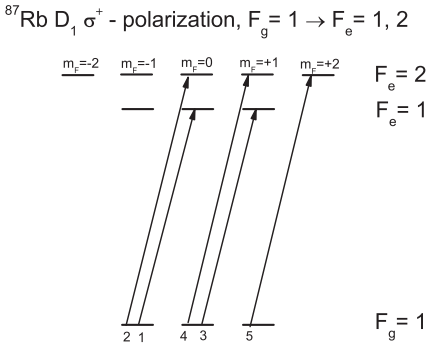

(e) The diagram of transitions from ground state $F_g = 1$.

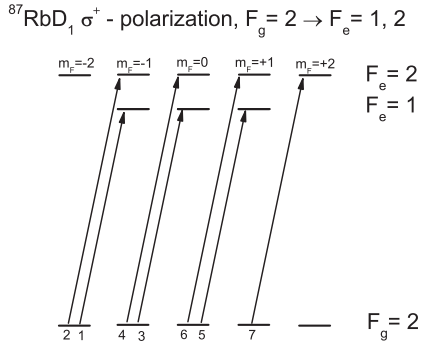

(f) The diagram of transitions from ground state $F_g = 2$.

Figure 3.4: The calculated frequency shift and intensity modification for ^{87}Rb transitions D_1 line for σ^+-polarized exciting radiation.

Interesting situation is observed on fig. 3.4(d). Amplitudes of the transitions from the ground state $F_g = 2$ with increasing magnetic field all tend to zero, except one transition 2. Amplitude of this transition with increasing magnetic field increases. For a magnitude of the magnetic field equals to ~ 1000 G, amplitude of this transition became the largest one and with increasing magnetic field asymptotically tends to its maximal value. The frequency of this transition undergoes "blue" shift equal to ~ 18 GHz for a value of the magnetic field near 10 000 G.

On fig. 3.5 is demonstrated frequency shift and intensity modification for ^{87}Rb D_1 system in case of π polarization of the laser radiation. The allowed transitions between magnetic sublevels for the ^{87}Rb, D_1 line from $F_g = 1$ and $F_g = 2$ ground states in the case of π (linear) polarized excitation and selection rules $\Delta m_F = 0$ are shown respectively on fig. 3.5(e) and fig. 3.5(f). As it is seen from these diagrams, there are allowed 6 transitions from $F_g = 1$ and 8 transitions from $F_g = 2$.

The transitions frequency shifts are shown on fig. 3.5(a) and fig. 3.5(b). It is interesting to note, that for transitions 1 and 8 from ground state $F_g = 2$, a linear shift of the frequencies in the whole range of the magnetic field is observed. To the transition denoted 1 corresponds the transition between Zeeman sublevels $F_g = 2, m_F = -2 \rightarrow F_e = 2, m_F = -2$ and to the transition under number 8 $F_g = 2, m_F = 2 \rightarrow F_e = 2, m_F = 2$. The reason of this linear behaviour is that the Zeeman sublevels corresponding to these transitions do not interact with any others Zeeman sublevels. Thus, magnetic field don't mix quantum states of these sublevels and as a result one may observe linear Zeeman effect in the whole range of the magnetic field values.

These systems have another interesting property. Unlike excitation with σ^+ polarized laser radiation, for π polarized radiation, there exists transition, which are "forbidden" in dipole approximation for $B = 0$. These two transitions are: $F_g = 1, m_F = 0 \rightarrow F_e = 1, m_F = 0$ (number 3 in fig. 3.5(e)) and $F_g = 2, m_F = 0 \rightarrow F_e = 2, m_F = 0$ (number 5 on fig. 3.5(f)).

On fig. 3.5(c) and fig. 3.5(d) are demonstrated theoretically calculated intensity modification for transitions respectively from $F_g = 1$ and $F_g = 2$.

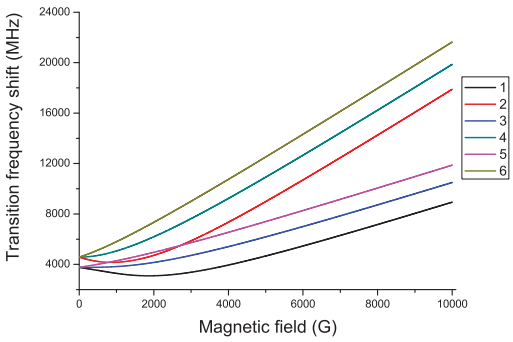

(a) The transitions frequency shift versus magnetic field, ground state $F_g = 1$.

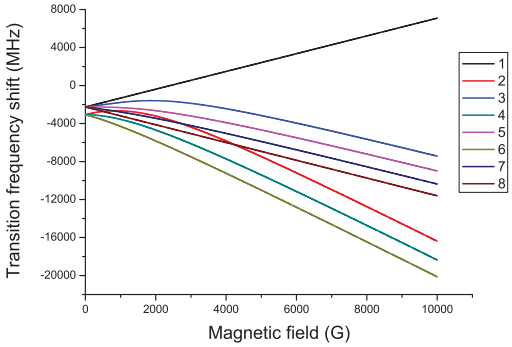

(b) The transitions frequency shift versus magnetic field, ground state $F_g = 2$.

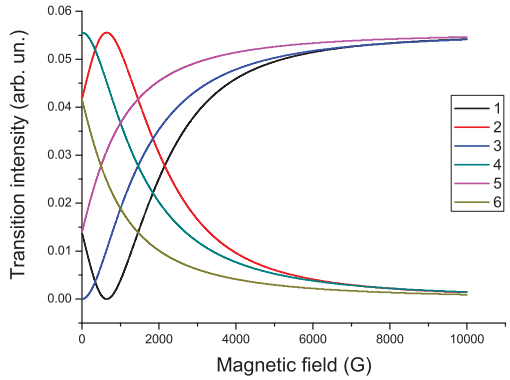

(c) The transitions intensity versus magnetic field, ground state $F_g = 1$.

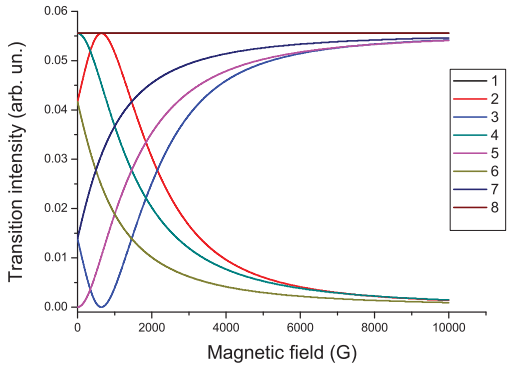

(d) The transitions intensity versus magnetic field, ground state $F_g = 2$.

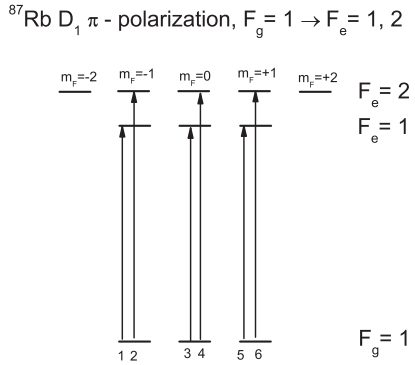

(e) The diagram of transitions from ground state $F_g = 1$.

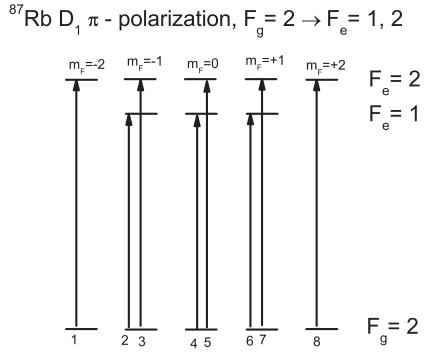

(f) The diagram of transitions from ground state $F_g = 2$.

Figure 3.5: The calculated frequency shift and intensity modification for ^{87}Rb transitions D_1 line for π-polarized exciting radiation.

For curve number 3, as it is seen from calculated curves, for the initially $B = 0$ the value of the transition intensity is equal to zero. However, due to the mixing of the quantum states under the influence of the external magnetic field, this transition intensity undergoes significant modification and with increasing magnetic field value, it is observed continuous increasing of the transition intensity. Starting from the values of magnetic field $B \sim 2300$ G the intensity on this transition is among the three strongest transitions and with increasing magnetic field the intensity value of these transitions asymptotically tend to the same value.

Similar peculiarity is observed for the transitions from ground state $F_g = 2$. The curve denoted 5 on fig. 3.5(d) corresponds to the transition $F_g = 2, m_F = 0 \rightarrow F_e = 2, m_F = 0$. Intensity of this transition is equal to zero for $B = 0$. With increasing of magnetic field its intensity increases and tends to the values of the strongest transition.

Previously was mentioned, that transitions denoted 1 and 8 demonstrate linear frequency shift (see fig. 3.5(b)). These transitions demonstrate particular behaviour of the transition intensity modification also. Two horizontal lines denoted 1 and 8 on fig. 3.5(d) (due to the same value of the transition intensity, it is impossible to distinguish these curves from each other) correspond respectively to the transitions $F_g = 2, m_F = -2 \rightarrow F_e = 2, m_F = -2$ and $F_g = 2, m_F = 2 \rightarrow F_e = 2, m_F = 2$. As it was mentioned earlier, there is no mixing of quantum states for these two states and as a result intensities of these transitions preserve their initial values.

On fig. 3.6 is demonstrated frequency shift and intensity modification for ^{87}Rb D_1 system in case of σ^- polarization of the laser radiation. The allowed transitions between magnetic sublevels for the ^{87}Rb, D_1 line from $F_g = 1$ and $F_g = 2$ ground states in the case of σ^- (right circle) polarized excitation and selection rules $\Delta m_F = -1$ are shown respectively on fig. 3.6(e) and fig. 3.6(f). As it is seen from these diagrams, there are allowed 5 transitions from $F_g = 1$ and 7 transitions from $F_g = 2$.

The frequency shifts of the transition in case of σ^- polarization of the exciting radiation are demonstrated on fig. 3.6(a) and fig. 3.6(b) respectively from $F_g = 1$ and $F_g = 2$ ground states. The transitions from the ground state $F_g = 1$ demonstrate strong positive shift of

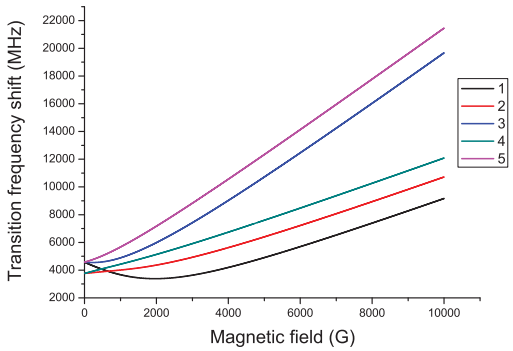

(a) The transitions frequency shift versus magnetic field, ground state $F_g = 1$.

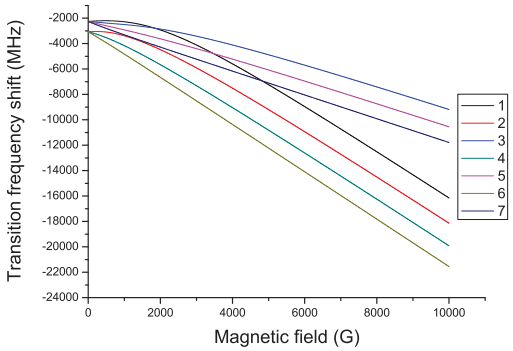

(b) The transitions frequency shift versus magnetic field, ground state $F_g = 2$.

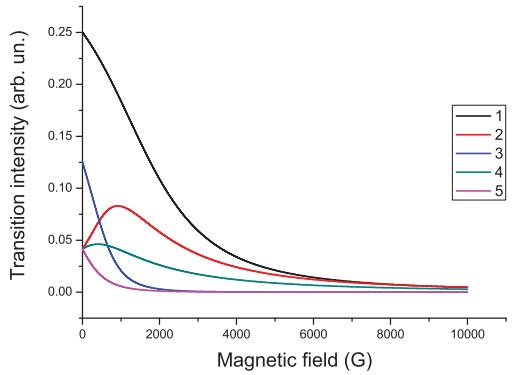

(c) The transitions intensity versus magnetic field, ground state $F_g = 1$.

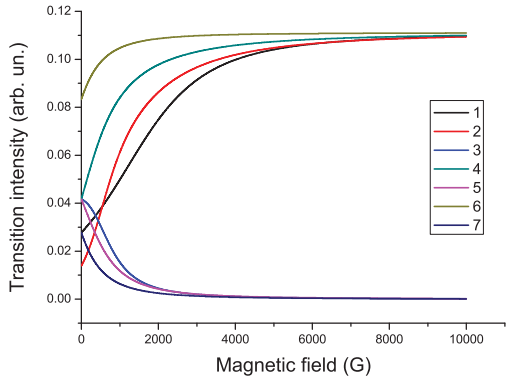

(d) The transitions intensity versus magnetic field, ground state $F_g = 2$.

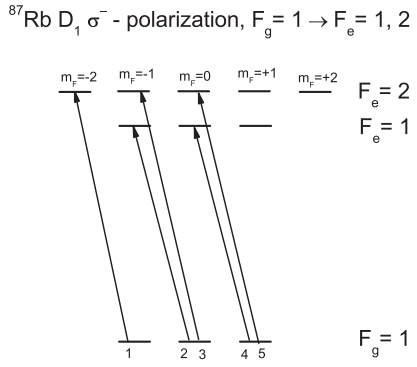

(e) The diagram of transitions from ground state $F_g = 1$.

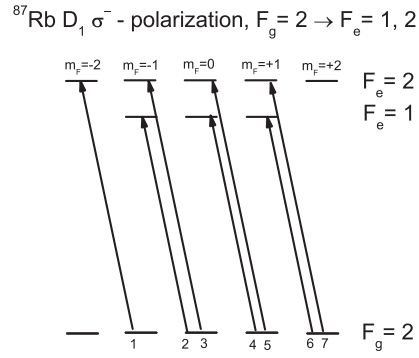

(f) The diagram of transitions from ground state $F_g = 2$.

Figure 3.6: The calculated frequency shift and intensity modification for ^{87}Rb transitions D_1 line for σ^--polarized exciting radiation.

the frequency in respect to initial value, meanwhile transitions from the ground state $F_g = 2$ demonstrate strong negative shift of the frequency. These shifts achieve $\sim$ 18 GHz for the value of magnetic field $B = 10\ 000$ G.

The calculated dependence of the transitions intensity modification is exhibited on the fig. 3.6(c) and fig. 3.6(d) respectively from $F_g = 1$ and $F_g = 2$ ground states. The calculated curves demonstrate a quite opposite behaviour in comparison with σ^+ polarization of the laser radiation. Meanwhile the intensities of transitions from $F_g = 1$ increase for major part of transitions, the intensity of transitions from same ground state in case of σ^- polarization decrease and tend to zero with increasing magnetic field magnitude. Similar behaviour demonstrate transition from ground state $F_g = 2$. In case of σ^+ polarization of the exciting laser radiation the intensities of the transitions tend to zero, except transition denoted 2, meanwhile for σ^- polarization the intensities of the major part of transitions asymptotically tend to same maximal value.

3.3.2 ^{85}Rb D_1 line transitions from the ground states $F_g = 2, 3$

The diagram of the energy levels for ^{8}5Rb D_1 line transitions is demonstrated of fig. 1.4. The total number of Zeeman sublevels for ground states is equal to 12 (5 Zeeman sublevels for $F_g = 2$ and 7 sublevels for $F_g = 3$) and 12 sublevels for excited states $F_e = 2, 3$ (5 Zeeman sublevels for $F_e = 2$ and 7 sublevels for $F_e = 3$).

We calculated frequency shifts and intensity modifications for all possible 62 transitions between the ground and excited states for σ^+, π and σ^- polarizations of the exciting laser radiation. On fig. 3.7, 3.8 and 3.9 are exhibited the results of the calculation made for ^{85}Rb D_1 line transitions from the ground states $F_g = 2, 3$ respectively for σ^+, π and σ^- polarizations of the exciting laser radiation.

Calculation for the all transitions demonstrates very close behaviour with ^{87}Rb D_1 line transitions. Main difference is number of transition satisfying to the selection rules.

Calculations for σ^+ polarization are shown on fig. 3.7. Frequency shifts for the transitions

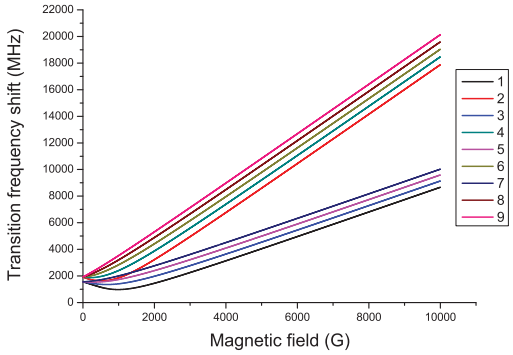

(a) The transitions frequency shift versus magnetic field, ground state $F_g = 2$.

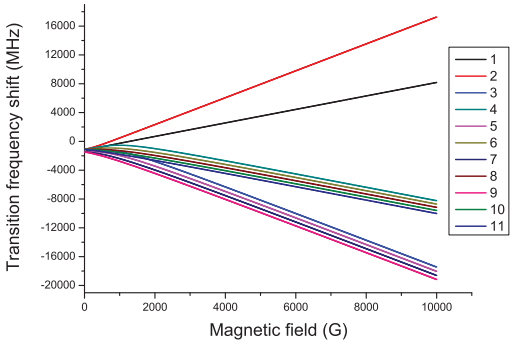

(b) The transitions frequency shift versus magnetic field, ground state $F_g = 3$.

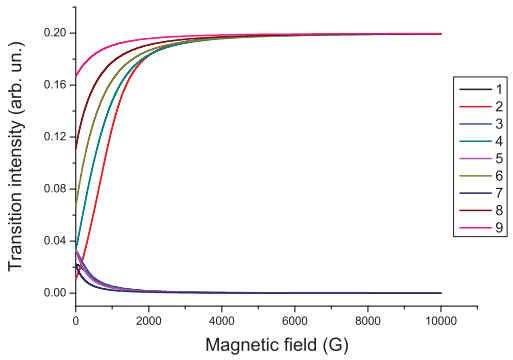

(c) The transitions intensity versus magnetic field, ground state $F_g = 2$.

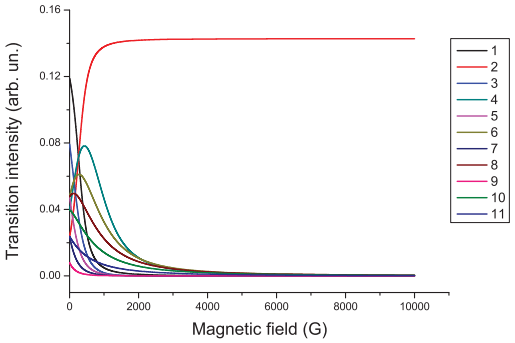

(d) The transitions intensity versus magnetic field, ground state $F_g = 3$.

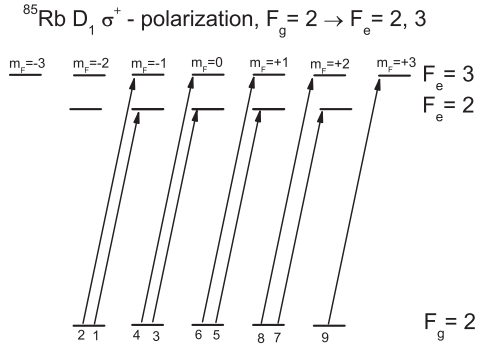

(e) The diagram of transitions from ground state $F_g = 2$.

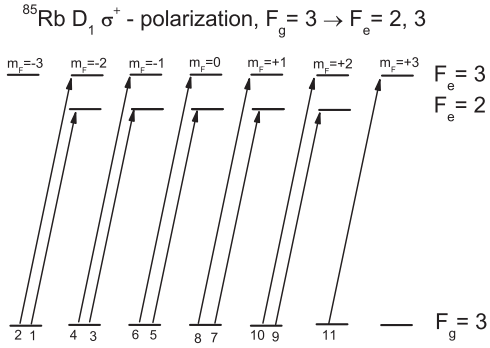

(f) The diagram of transitions from ground state $F_g = 3$.

Figure 3.7: The calculated frequency shift and intensity modification for ^{85}Rb transitions D_1 line for σ^+-polarized exciting radiation.

between the ground state $F_g = 2$ and excited states are shown on fig. 3.7(a) and from the ground state $F_g = 3$ on fig. 3.7(b). The intensities of the transitions from the ground state $F_g = 2$ are demonstrated on fig. 3.7(c). Values of the intensities for five transitions numbered 2, 4, 6, 8 and 9 (numbers of the curves correspond to the numbers of the transition indicated on the diagrams respectively for the ground state $F_g = 2$ on fig. 3.7(e) and for $F_g = 3$ on fig. 3.7(f)) increase with increasing of the magnetic field value and asymptotically tend to maximum and for transitions numbered 1, 3, 5 and 7 decrease and tend to zero with increasing magnetic field. The transitions from the ground state $F_g = 3$ are exhibited on fig. 3.7(d). The intensities of these transitions tend to zero with increasing magnetic field value, except one transition denoted 2 (see fig. 3.7(d)).

On fig. 3.8 are shown calculations for π polarized laser excitation. The frequency shift for transitions from $F_g = 2, 3$ are demonstrated respectively on fig. 3.8(a) and fig. 3.8(b). Calculations demonstrate strong shift of the transitions frequency in respect to the initial position for $B = 0$. These shifts are about 20 GHz for $B = 10\ 000$ G. Two transitions from ground state $F_g = 3$ numbered 1 ($F_g = 3, m_F = -3 \rightarrow F_e = 3, m_F = -3$) and 12 ($F_g = 3, m_F = 3 \rightarrow F_e = 3, m_F = 3$), as well as for for ^{87}Rb, exhibit linear shift in whole range of the magnetic field values. The absence of the quantum states mixing is the reason of these linear shifts.

On fig. 3.8(c) and fig. 3.8(d) are demonstrated transitions intensity modification versus magnetic field values. As well as for ^{87}Rb, for ^{85}Rb there exist two transitions, numbered 5 on fig. 3.8(c) and 7 on fig. 3.8(d), which are forbidden in dipole approximation for $B = 0$ and with increasing the value of magnetic field increase their intensities. These transitions are $F_g = 2, m_F = 0 \rightarrow F_e = 2, m_F = 0$ and $F_g = 3, m_F = 0 \rightarrow F_e = 3, m_F = 0$. For ^{85}Rb the reason of these observed peculiarities is the same as for ^{87}Rb (see explanation in section 3.3.1). Two horizontal lines denoted 1 and 12 on fig. 3.8(d) (due to the same value of the transition intensity, it is impossible to distinguish these curves from each other) correspond respectively to the transitions $F_g = 3, m_F = -3 \rightarrow F_e = 3, m_F = -3$ and $F_g = 3, m_F = 3 \rightarrow F_e = 3, m_F = 3$. The reason of this fact is that the Zeeman sublevels corresponding to these transitions do

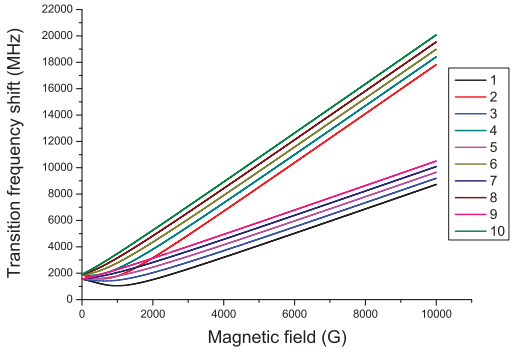

(a) The transitions frequency shift versus magnetic field, ground state $F_g = 2$.

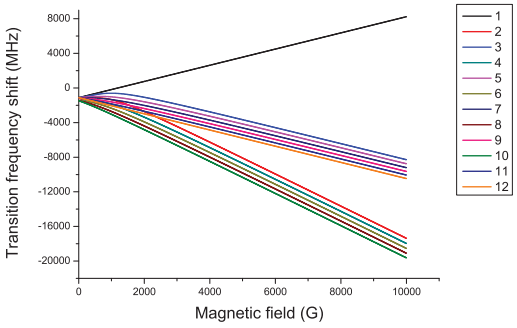

(b) The transitions frequency shift versus magnetic field, ground state $F_g = 3$.

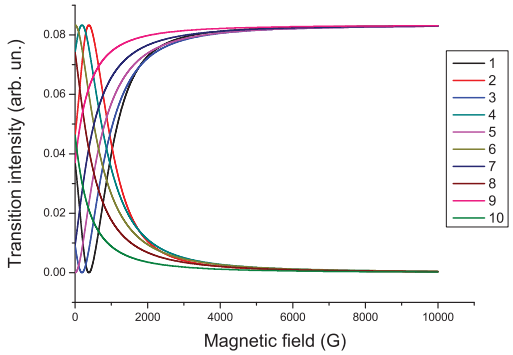

(c) The transitions intensity versus magnetic field, ground state $F_g = 2$.

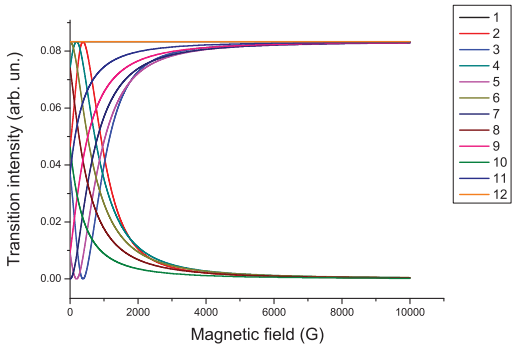

(d) The transitions intensity versus magnetic field, ground state $F_g = 3$.

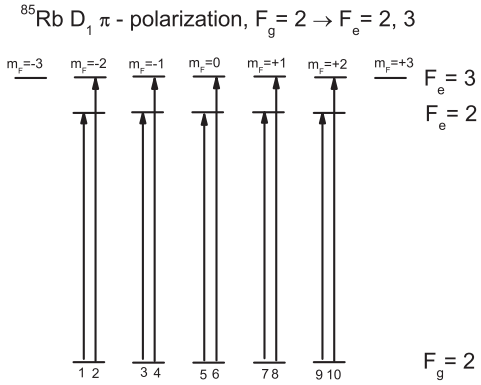

(e) The diagram of transitions from ground state $F_g = 2$.

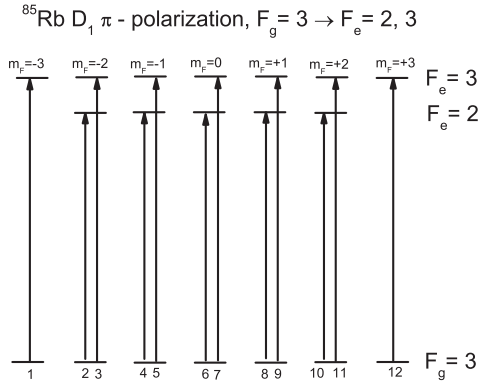

(f) The diagram of transitions from ground state $F_g = 3$.

Figure 3.8: The calculated frequency shift and intensity modification for ^{85}Rb transitions D_1 line for π-polarized exciting radiation.

not interact with any others Zeeman sublevels. Thus, magnetic field do not mix quantum states of these sublevels and as a result one may observe linear Zeeman effect in whole range of magnetic field values.

On fig. 3.9 is demonstrated frequency shift and intensity modification for ^{85}Rb D_1 system in case of σ^- polarization of the laser radiation. The allowed transitions between magnetic sublevels for the ^{85}Rb, D_1 line from $F_g = 2$ and $F_g = 3$ ground states in the case of σ^- (right circle) polarized excitation and selection rules $\Delta m_F = -1$ are shown respectively on fig. 3.9(e) and fig. 3.9(f).

The frequency shifts of the transition in case of σ^- polarization of the exciting radiation are demonstrated on fig. 3.9(a) and fig. 3.9(b) respectively from $F_g = 2$ and $F_g = 3$ ground states. The transitions from both ground state $F_g = 2, 3$ demonstrate strong shift of the frequency. These shifts are about ~ 18 GHz for the value of magnetic field $B = 10\,000$ G. The calculated dependence of the transitions intensity modification is exhibited on the fig. 3.9(c) and fig. 3.9(d) respectively from $F_g = 2$ and $F_g = 3$ ground states. As well as for ^{87}Rb, the calculated curves demonstrate a quite opposite behaviour in comparison with σ^+ polarization of the laser radiation. Meanwhile the intensities of transitions from $F_g = 2$ increase for major part of the transitions, the intensities of the transitions from the same ground state in case of σ^- polarization decrease and tend to zero with increasing of magnetic field magnitude. The transitions from ground state $F_g = 3$ demonstrate similar behaviour. In case of σ^+ polarization of the exciting laser radiation the intensities of the transitions tend to zero, except transition denoted 2, meanwhile for σ^- polarization the intensities of the major part of the transitions asymptotically tend to the same maximal value.

3.3.3 ^{87}Rb D_2 line transitions from the ground states $F_g = 1, 2$

The diagram of the energy levels for ^{87}Rb D_2 line transitions is demonstrated of fig. 1.5. Initially the system has a more complicated structure of the energy levels in comparison with Rb D_1 line. Taking into account the degeneracy of the hyperfine levels, the diagram of

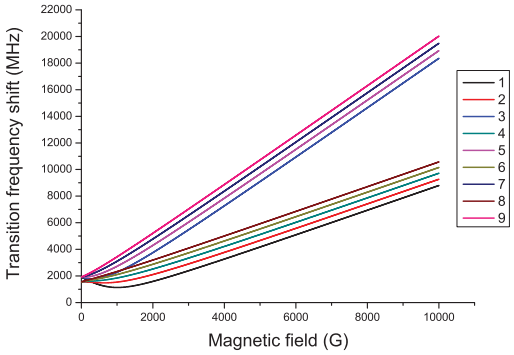

(a) The transitions frequency shift versus magnetic field, ground state $F_g = 2$.

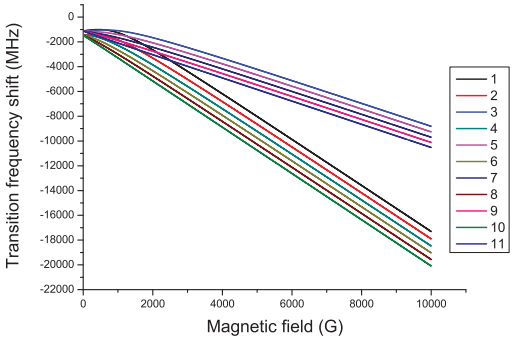

(b) The transitions frequency shift versus magnetic field, ground state $F_g = 3$.

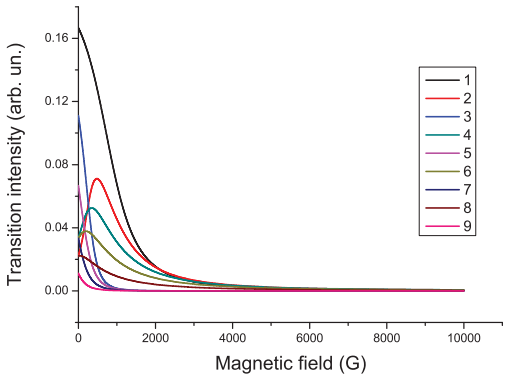

(c) The transitions intensity versus magnetic field, ground state $F_g = 2$.

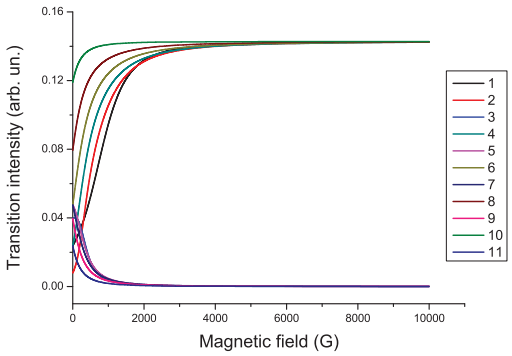

(d) The transitions intensity versus magnetic field, ground state $F_g = 3$.

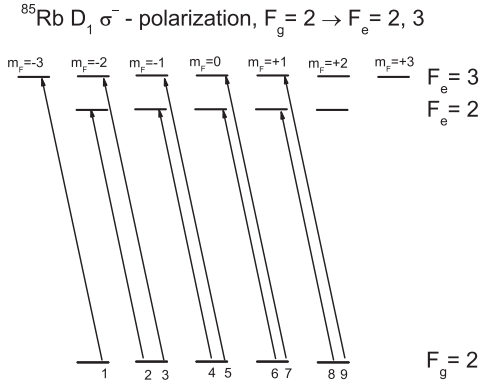

(e) The diagram of transitions from ground state $F_g = 2$.

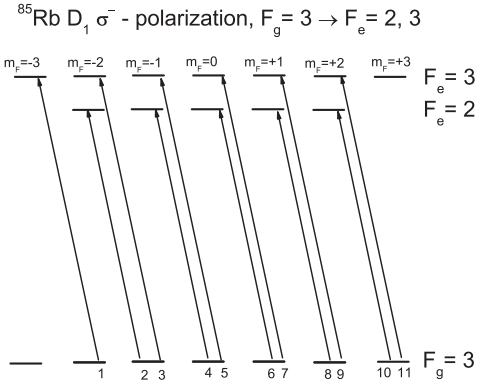

(f) The diagram of transitions from ground state $F_g = 3$.

Figure 3.9: The calculated frequency shift and intensity modification for ^{85}Rb transitions D_1 line for σ^--polarized exciting radiation.

the energy levels has even a more complicated structure. The total number of the Zeeman sublevels for ^{87}Rb D_2 line is equal to 24. The number of Zeeman sublevels corresponding to the ground states is the same as for D_1 and is equal to 8. However for the excited states it is 16 (1 Zeeman sublevel for excited hyperfine state $F_e = 0$, 3 sublevels for $F_e = 1$, 5 sublevels for $F_e = 2$ and 7 sublevels for excited state $F_e = 3$). Due to the large number of the excited states, the interactions, under the influence of the external magnetic field, between the Zeeman sublevels, are more complex. Mixing of the quantum states corresponding to the $6^2P_{3/2}$ has a more significant contribution in quantum magnitudes modification and due to this reason more complex picture of the observed nonlinear effects.

We calculated frequency shifts and intensity modifications for all possible transitions between the ground and excited states for σ^+, π and σ^- polarizations of the exciting laser radiation. On fig. 3.10, 3.11 and 3.12 (resp.) are exhibited the result of the calculation made for ^{87}Rb D_2 line transitions from the ground states $F_g = 1, 2$ for σ^+, π and σ^- (resp.) polarizations of the exciting laser radiation.

All the possible transitions between magnetic sublevels of hyperfine states for the ^{87}Rb, D_2 line from ground states $F_g = 1, 2$ in the case of σ^+ (left circular) polarized excitation and selection rules $\Delta m_F = +1$ are depicted respectively on fig. 3.10(e) and fig. 3.10(f). As it is seen from these diagrams, there are 9 transitions allowed from $F_g = 1$ and 13 transitions from $F_g = 2$. One of the most interesting peculiarities of these systems is the fact, that a number of transition is strictly forbidden in the dipole approximation according to the selection rules of F angular momentum $\Delta F = 0, \pm 1$. However with increasing the magnitude of magnetic field, the intensity of these transition is modified. The reason of this modification is, as in the previously considered cases, mixing of the quantum states of the unperturbed system. There are 3 forbidden transitions from ground state $F_g = 1$: $F_g = 1, m_F = -1 \rightarrow F_g = 3, m_F = 0$, $F_g = 1, m_F = 0 \rightarrow F_g = 3, m_F = +1$ and $F_g = 1, m_F = +1 \rightarrow F_g = 3, m_F = +2$ denoted respectively 4, 7 and 9 on diagram 3.10(e); and one transition from the ground state $F_g = 2$: $F_g = 2, m_F = -1 \rightarrow F_g = 0, m_F = 0$ denoted 4 on diagram 3.10(f).

The frequency shifts of transitions are shown on fig. 3.10(a) and fig. 3.10(b) respectively for

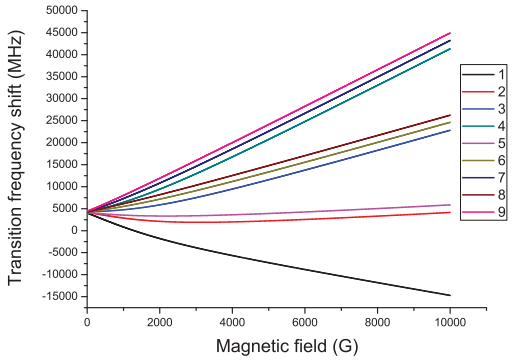

(a) The transitions frequency shift versus magnetic field, ground state $F_g = 1$.

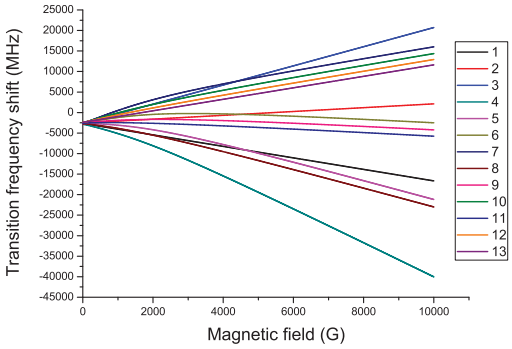

(b) The transitions frequency shift versus magnetic field, ground state $F_g = 2$.

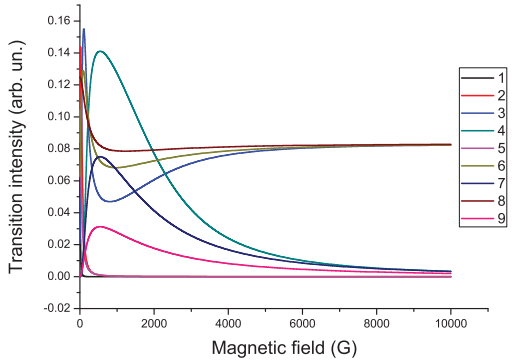

(c) The transitions intensity versus magnetic field, ground state $F_g = 1$.

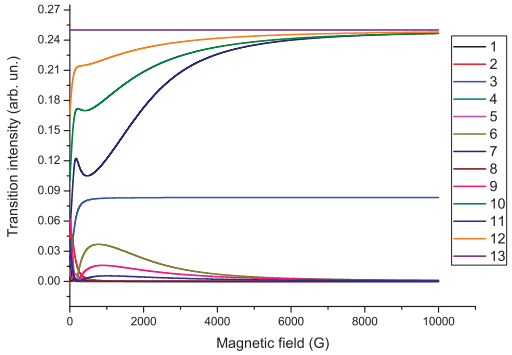

(d) The transitions intensity versus magnetic field, ground state $F_g = 2$.

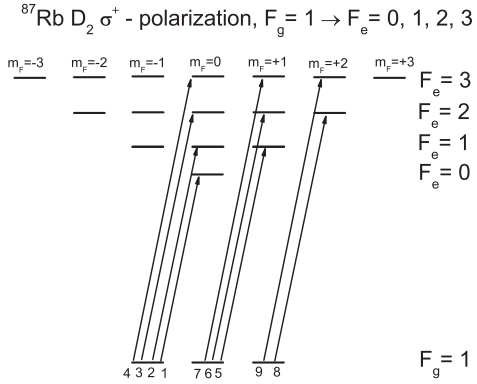

(e) The diagram of transitions from ground state $F_g = 1$.

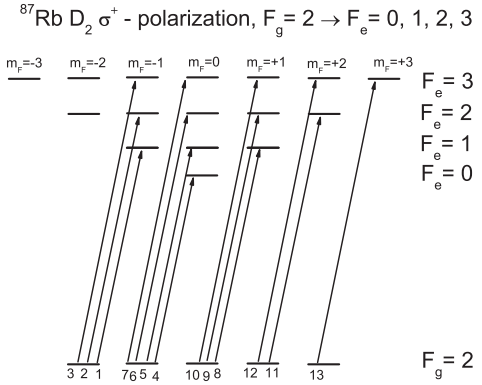

(f) The diagram of transitions from ground state $F_g = 2$.

Figure 3.10: The calculated frequency shift and intensity modification for ^{87}Rb transitions D_2 line for σ^+-polarized exciting radiation.

$F_g = 1$ and $F_g = 2$. The numbering of the curves on the figure corresponds to the numbering of the transitions on the diagrams exhibited on fig. 3.10(e) and fig. 3.10(f). From fig. 3.10(a) and fig. 3.10(b) it is seen that under the influence of external magnetic field, the transitions between Zeeman sublevels undergo strong frequency shift in respect with their initial value. These shifts are conditioned by strong shift of the Zeeman sublevels in respect to the initial positions, which exceeds the frequency distance between hyperfine levels and may achieve tens of GHz.

On fig. 3.10(c) and fig. 3.10(d) are demonstrated transitions intensity modification respectively for $F_g = 1$ and $F_g = 2$.

As it is seen from fig. 3.10(c) and 3.10(d) the behaviour of the curves has a complex character. For instance behaviour of the transitions intensity numbered 4, 7 and 9 on fig. 3.10(c) which are initially equal to zero for $B = 0$. With increasing of magnetic filed value, the intensity of these transitions increase and became the strongest transitions. However, with further increasing of the magnetic field value, the intensity of these transitions decrease and tend to zero. Finally, we have nonzero intensities only for three transitions, numbered 3, 6 and 8, and amplitudes of all the other transitions tend to zero.

For the transitions from ground state $F_g = 2$ other peculiarities are observed. The transition $F_g = 2, m_F = +2 \rightarrow F_e = 3, m_F = +3$ numbered 13 (see diagram 3.10(f)) demonstrates linear shift of the transition frequency in whole range of the magnetic field values. The absence of mixing of the quantum states is the reason of this linearity. Same reason leads to the constant value of the intensity for this transition and one may see on fig. 3.10(d) a horizontal line describing transition numbered 13.

On fig. 3.11 are demonstrated frequency shift and intensity modification for ^{87}Rb D_2 system in the case of π polarization of the laser radiation.All the possible transitions between magnetic sublevels for the ^{87}Rb, D_2 line from $F_g = 1$ and $F_g = 2$ ground states in the case of π (linear polarization) polarized excitation and selection rules $\Delta m_F = 0$ are exhibited respectively on fig. 3.11(e) and fig. 3.11(f). As it is seen from these diagrams, there are 10 allowed transitions from $F_g = 1$ and 14 transitions from $F_g = 2$.

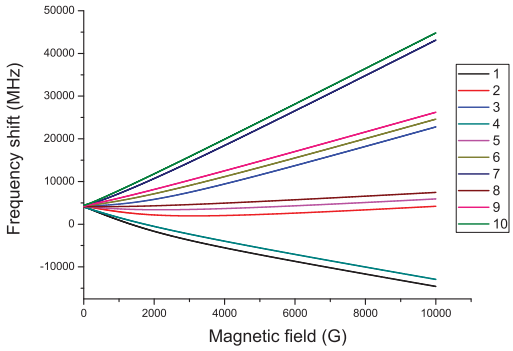

(a) The transitions frequency shift versus magnetic field, ground state $F_g = 1$.

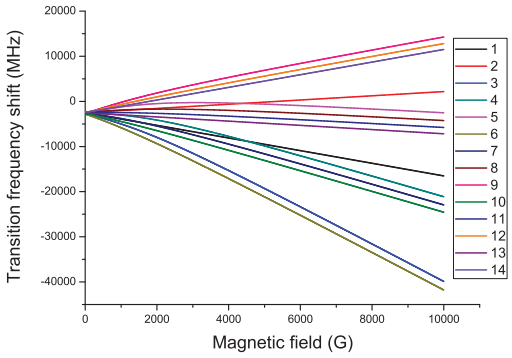

(b) The transitions frequency shift versus magnetic field, ground state $F_g = 2$.

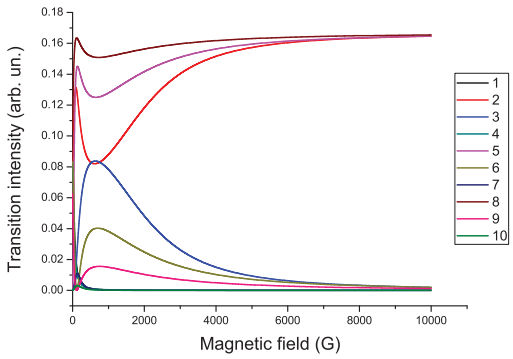

(c) The transitions intensity versus magnetic field, ground state $F_g = 1$.

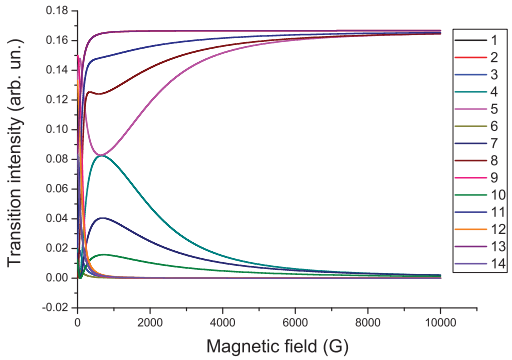

(d) The transitions intensity versus magnetic field, ground state $F_g = 2$.

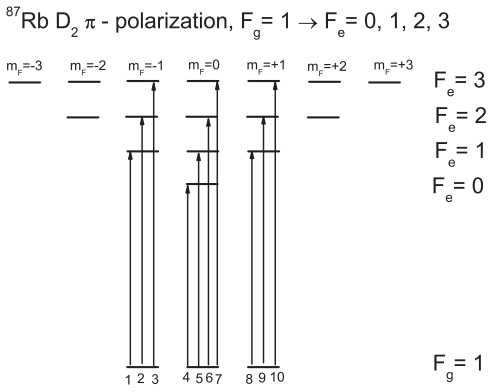

(e) The diagram of transitions from ground state $F_g = 1$.

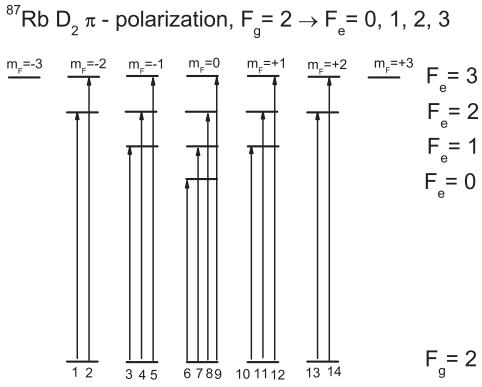

(f) The diagram of transitions from ground state $F_g = 2$.

Figure 3.11: The calculated frequency shift and intensity modification for ^{87}Rb transitions D_2 line for π-polarized exciting radiation.

The transitions frequency shifts are shown on fig. 3.11(a) and fig. 3.11(b) respectively for $F_g = 1$ and $F_g = 2$. In case of π polarization of laser radiation, this systems has two transitions $F_g = 1, m_F = 0 \rightarrow F_g = 1, m_F = 0$ and $F_g = 2, m_F = 0 \rightarrow F_g = 2, m_F = 0$, which are forbidden due to the symmetry of the system and four transitions which are strictly forbidden in the dipole approximation according to the selection rules of F angular momentum $\Delta F = 0, \pm 1$. These four forbidden transitions are: three forbidden transitions from ground state $F_g = 1$: $F_g = 1, m_F = -1 \rightarrow F_g = 3, m_F = -1$, $F_g = 1, m_F = 0 \rightarrow F_g = 3, m_F = 0$ and $F_g = 1, m_F = +1 \rightarrow F_g = 3, m_F = +1$ denoted respectively 3, 7 and 10 on diagram 3.11(e); and one transition from the ground state $F_g = 2$: $F_g = 2, m_F = 0 \rightarrow F_g = 0, m_F = 0$ denoted 6 on diagram 3.11(f). The variation of the magnetic field leads to modification of the system quantum characteristics. The reason of this modification is, as in the previously considered cases, mixing of the quantum states of the unperturbed system.

Among all these transitions it is interesting to mention the behaviour of two transitions denoted 5 and 8 on on fig. 3.11(e). The transition numbered 5 demonstrate very strong nonlinear shift of transition frequency. The nonlinear Zeeman effect is observed for magnetic field value equal to ~ 3 G. The intensity of this transition is among the strongest transitions. The transition denoted 8, as well as transition 5, demonstrates a strong nonlinear shift of transition frequency, but expressed in opposite way. The frequency of this transition vary insides of ~ 15 MHz in large range of magnetic field values, from 100 to 1000 G. This transition in whole range of the magnetic field values demonstrate largest intensity of transition.

On fig. 3.12 are demonstrated frequency shift and intensity modification for ^{87}Rb D_2 line system in case of σ^- polarization of the laser radiation. The allowed transitions between magnetic sublevels for the ^{87}Rb, D_2 line from $F_g = 1$ and $F_g = 2$ ground states in the case of σ^- (right circle) polarized excitation and selection rules $\Delta m_F = -1$ are shown respectively on fig. 3.12(e) and fig. 3.12(f). As it is seen from these diagrams, there are 9 allowed transitions from $F_g = 1$ and 13 transitions from $F_g = 2$.

The frequency shifts of the transition in case of σ^- polarization of the exciting radiation are demonstrated on fig. 3.12(a) and fig. 3.12(b) respectively from $F_g = 1$ and $F_g = 2$ ground

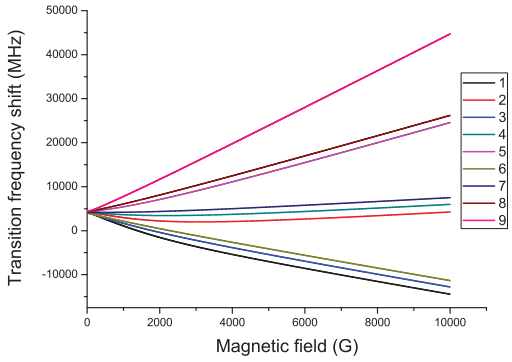

(a) The transitions frequency shift versus magnetic field, ground state $F_g = 1$.

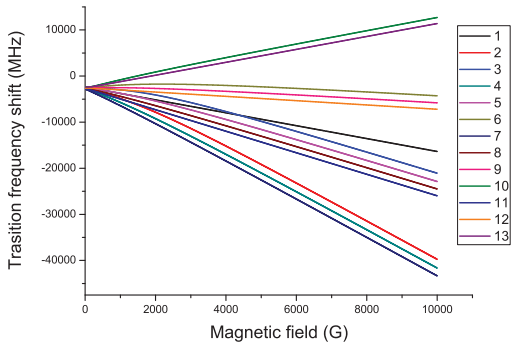

(b) The transitions frequency shift versus magnetic field, ground state $F_g = 2$.

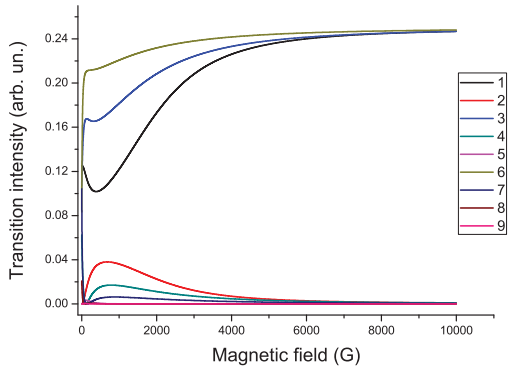

(c) The transitions intensity versus magnetic field, ground state $F_g = 1$.

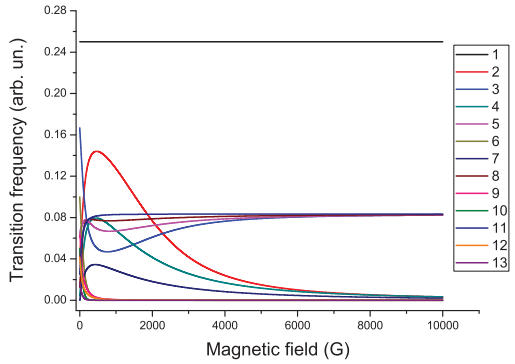

(d) The transitions intensity versus magnetic field, ground state $F_g = 2$.

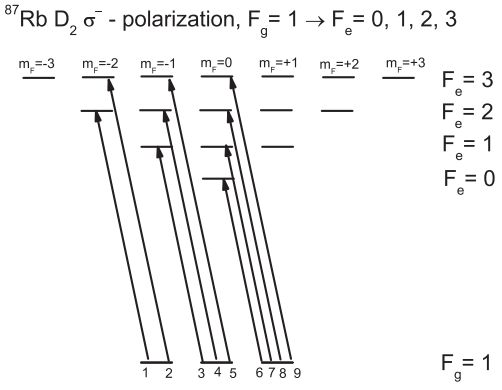

(e) The diagram of transitions from ground state $F_g = 1$.

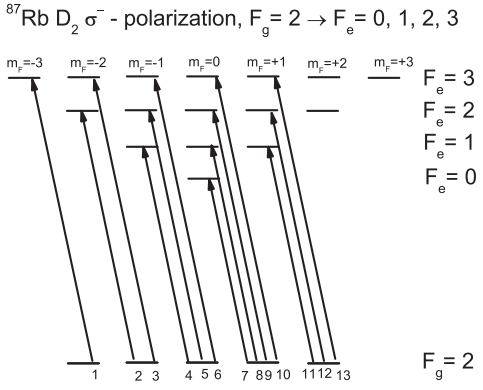

(f) The diagram of transitions from ground state $F_g = 2$.

Figure 3.12: The calculated frequency shift and intensity modification for ^{87}Rb transitions D_2 line for σ^--polarized exciting radiation.

states. The transitions from the ground states $F_g = 1$ and $F_g = 2$ demonstrate strong shift of the frequency in respect to initial value. These shifts achieves ~ 40 GHz for the value of magnetic field $B = 10\ 000$ G.

The calculated dependence of the transitions intensity modification is exhibited on the fig. 3.12(c) and fig. 3.12(d) respectively from $F_g = 1$ and $F_g = 2$ ground states. The calculated curves demonstrate a complex behaviour of the transitions intensity modification. There are four transitions forbidden in the dipole approximation for σ^- polarization of laser radiation. Three of them correspond to the transitions from ground state $F_g = 1$: $F_g = 1, m_F = -1 \rightarrow F_g = 3, m_F = -2$, $F_g = 1, m_F = 0 \rightarrow F_g = 3, m_F = -1$ and $F_g = 1, m_F = +1 \rightarrow F_g = 3, m_F = 0$ denoted respectively 2, 5 and 9 on diagram 3.12(e); and one transition from the ground state $F_g = 2$: $F_g = 2, m_F = +1 \rightarrow F_g = 0, m_F = 0$ denoted 7 on diagram 3.12(f). The transition numbered 1 from ground state $F_g = 2$ is an unmixed transition, thus the intensity of this transition does not change with increasing the magnetic field value and it demonstrates a linear shift of transition frequency in whole range of magnetic field.

3.3.4 ^{85}Rb D_2 line transitions from the ground states $F_g = 2, 3$

The diagram of the energy levels for ^{85}Rb D_2 line transitions is demonstrated of fig. 1.5. The total number of Zeeman sublevels for ^{85}Rb D_2 line is equal to 36. The number of Zeeman sublevels corresponding to the ground states is the same as for D_1 and is equal to 12. However for excited states it is 24 (3 Zeeman sublevels for excited hyperfine state $F_e = 1$, 5 sublevels for $F_e = 2$, 7 sublevels for $F_e = 3$ and 9 sublevels for excited state $F_e = 4$). Due to the large number of the excited states, the interactions, under the influence of the external magnetic field, between the Zeeman sublevels, are more complex. Mixing of the quantum states corresponding to the $6^2P_{3/2}$ has a more significant contribution in quantum characteristics modification and due to this reason a more complex picture of the observed nonlinear effects. We calculated frequency shifts and intensity modifications for all possible transitions between the ground and excited states for σ^+, π and σ^- polarizations of the

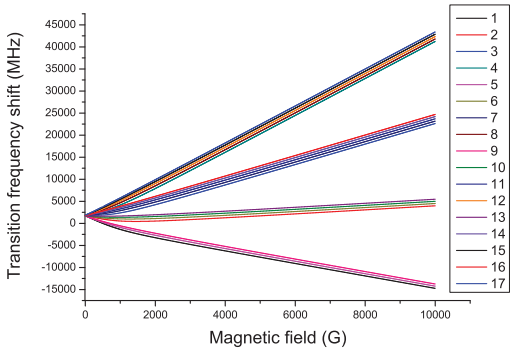

(a) The transitions frequency shift versus magnetic field, ground state $F_g = 2$.

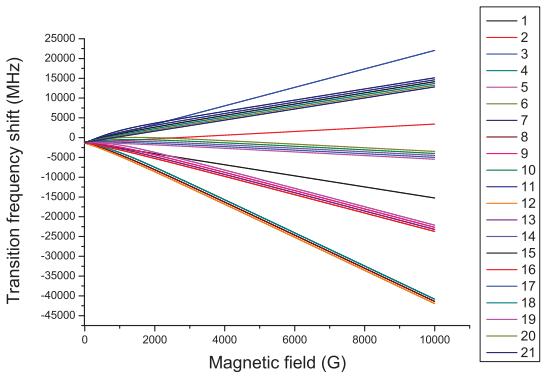

(b) The transitions frequency shift versus magnetic field, ground state $F_g = 3$.

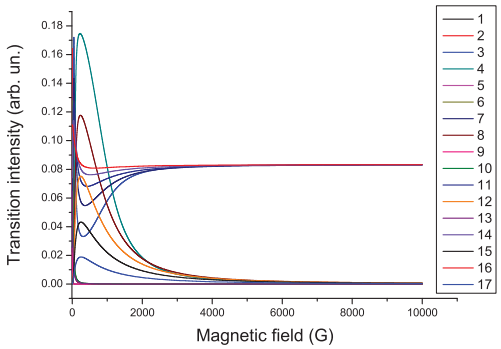

(c) The transitions intensity versus magnetic field, ground state $F_g = 2$.

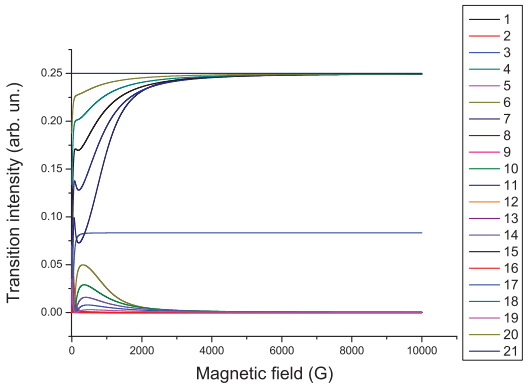

(d) The transitions intensity versus magnetic field, ground state $F_g = 3$.

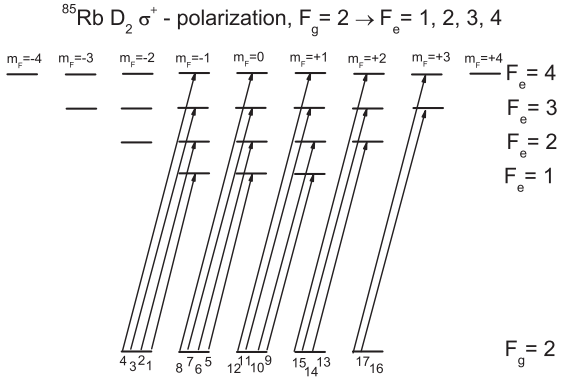

(e) The diagram of transitions from ground state $F_g = 2$.

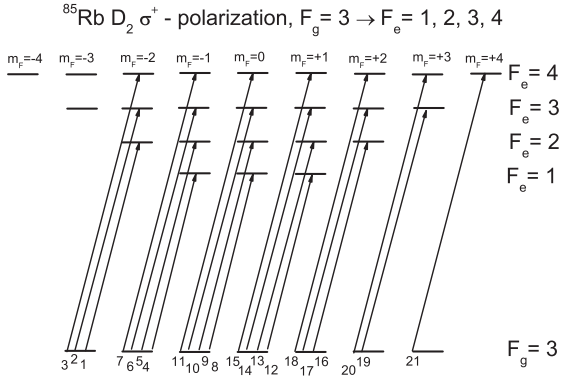

(f) The diagram of transitions from ground state $F_g = 3$.

Figure 3.13: The calculated frequency shift and intensity modification for ^{85}Rb transitions D_2 line for σ^+-polarized exciting radiation.

exciting laser radiation. On fig. 3.13, 3.14 and 3.15 (resp.) are exhibited the result of the calculations made for ^{85}Rb D_2 line transitions from the ground states $F_g = 2, 3$ for σ^+, π and σ^- (resp.) polarizations of the exciting laser radiation.

All the possible transitions between magnetic sublevels of hyperfine states for ^{85}Rb, D_2 line, from ground states $F_g = 2, 3$ in the case of σ^+ (left circular) polarized excitation and selection rules $\Delta m_F = +1$ are depicted respectively on fig. 3.13(e) and fig. 3.13(f). As it is seen from these diagrams, there are 17 allowed transitions from $F_g = 2$ and 21 transitions from $F_g = 3$. One of the most interesting peculiarities of these systems is the fact, that a number of transitions are strictly forbidden in the dipole approximation according to the selection rules of F angular momentum $\Delta F = 0, \pm 1$. However with increasing the magnitude of magnetic field, the intensity of these transitions is modified. The reason of this modification is, as in the previously considered cases, mixing of the quantum states of the unperturbed system. There are 5 forbidden transitions from ground state $F_g = 2$: $F_g = 2, m_F = -2 \to F_g = 4, m_F = -1$, $F_g = 2, m_F = -1 \to F_g = 4, m_F = 0$, $F_g = 2, m_F = 0 \to F_g = 4, m_F = +1$, $F_g = 2, m_F = +1 \to F_g = 4, m_F = +2$ and $F_g = 2, m_F = +2 \to F_g = 4, m_F = +3$ denoted respectively 4, 8, 12, 15 and 17 on diagram 3.13(e); and 3 transitions from the ground state $F_g = 3$: $F_g = 3, m_F = -2 \to F_g = 1, m_F = -1$, $F_g = 3, m_F = -1 \to F_g = 1, m_F = 0$ and $F_g = 3, m_F = 0 \to F_g = 1, m_F = +1$ denoted 4, 8 and 12 on diagram 3.13(f).

The frequency shifts of transitions are shown on fig. 3.13(a) and fig. 3.13(b) respectively for $F_g = 2$ and $F_g = 3$. The numbering of the curves on the figure corresponds to the numbering of the transitions on the diagrams exhibited on fig. 3.13(e) and fig. 3.13(f). On fig. 3.13(c) and fig. 3.13(d) are demonstrated transitions intensity modification respectively for $F_g = 2$ and $F_g = 3$.

On fig. 3.14 are demonstrated frequency shift and intensity modification for ^{85}Rb D_2 system in case of π polarization of the laser radiation. All the possible transitions between magnetic sublevels for the ^{85}Rb, D_2 line from $F_g = 2$ and $F_g = 3$ ground states in the case of π (linear polarization) polarized excitation and selection rules $\Delta m_F = 0$ are exhibited respectively on fig. 3.14(e) and fig. 3.14(f). There are allowed 18 transitions from $F_g = 2$ and 22 transitions

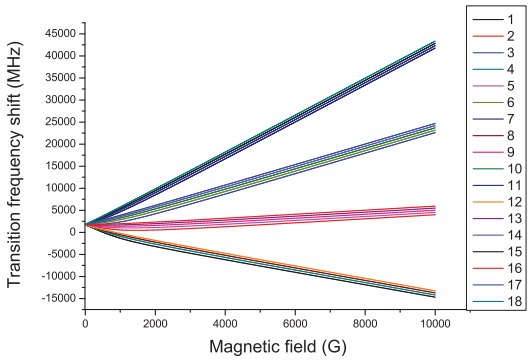

(a) The transitions frequency shift versus magnetic field, ground state $F_g = 2$.

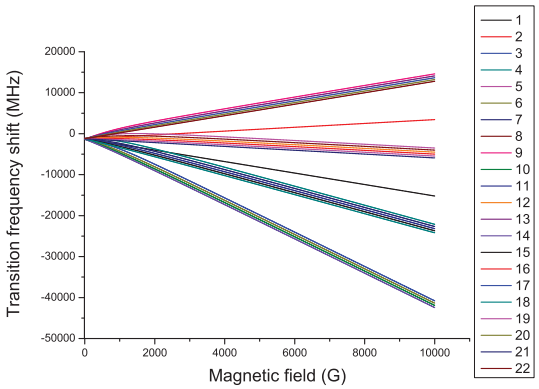

(b) The transitions frequency shift versus magnetic field, ground state $F_g = 3$.

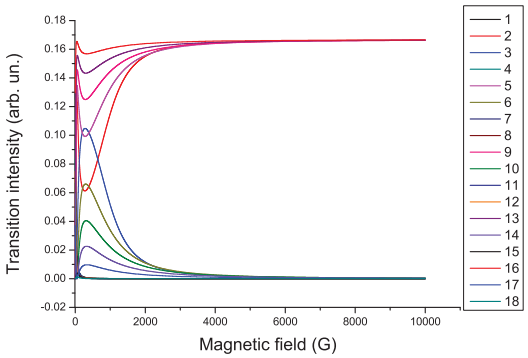

(c) The transitions intensity versus magnetic field, ground state $F_g = 2$.

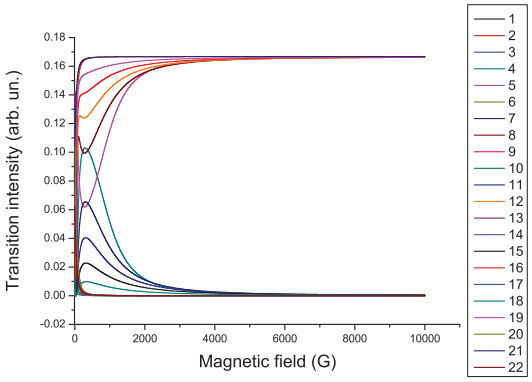

(d) The transitions intensity versus magnetic field, ground state $F_g = 3$.

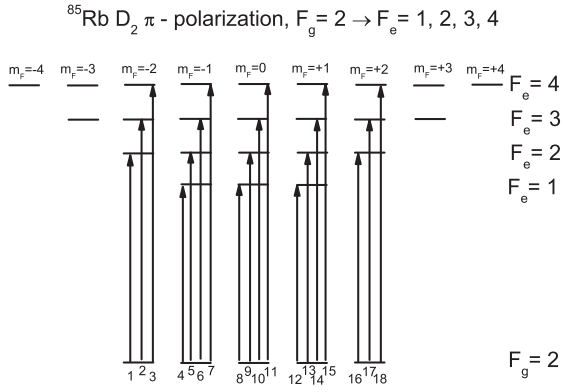

(e) The diagram of transitions from ground state $F_g = 2$.

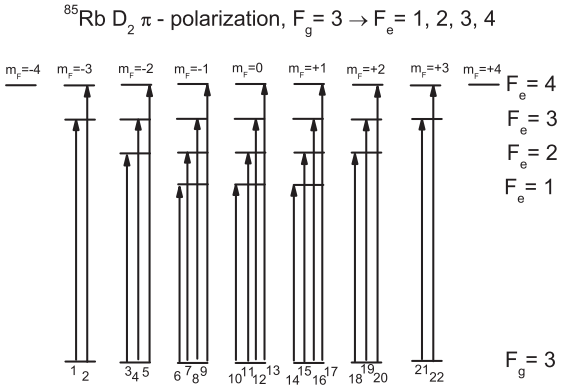

(f) The diagram of transitions from ground state $F_g = 3$.

Figure 3.14: The calculated frequency shift and intensity modification for ^{85}Rb transitions D_2 line for π-polarized exciting radiation.

from $F_g = 3$.

The transitions frequency shifts are shown on fig. 3.14(a) and fig. 3.14(b) respectively for $F_g = 2$ and $F_g = 3$. In case of π polarization of laser radiation, this systems has two transitions $F_g = 1, m_F = 0 \to F_g = 2, m_F = 0$ and $F_g = 3, m_F = 0 \to F_g = 3, m_F = 0$, which are forbidden due to the symmetry of the system and 8 transitions which are strictly forbidden in the dipole approximation according to the selection rules of F angular momentum $\Delta F = 0, \pm 1$. These 8 forbidden transitions are: 5 forbidden transitions from ground state $F_g = 2$: $F_g = 2, m_F = -2 \to F_g = 4, m_F = -2$, $F_g = 2, m_F = -1 \to F_g = 4, m_F = -1$, $F_g = 2, m_F = 0 \to F_g = 4, m_F = 0$, $F_g = 2, m_F = +1 \to F_g = 4, m_F = +1$, and $F_g = 2, m_F = +2 \to F_g = 4, m_F = +2$, denoted respectively 3, 7, 11, 15 and 18 on diagram 3.14(e); and 3 transitions from the ground state $F_g = 3$: $F_g = 3, m_F = -1 \to F_g = 1, m_F = -1$, $F_g = 3, m_F = 0 \to F_g = 1, m_F = 0$ and $F_g = 3, m_F = +1 \to F_g = 1, m_F = +1$ denoted 6, 10 and 14 on diagram 3.14(f). The variation of the magnetic field leads to modification of the system quantum characteristics. The reason of this modification is, as in the previously considered cases, mixing of the quantum states of the unperturbed system.

On fig. 3.15 are demonstrated frequency shift and intensity modification for ^{85}Rb D_2 line system in case of σ^- polarization of the laser radiation. The allowed transitions between magnetic sublevels for the ^{85}Rb, D_2 line from $F_g = 2$ and $F_g = 3$ ground states in the case of σ^- (right circle) polarized excitation and selection rules $\Delta m_F = -1$ are shown respectively on fig. 3.15(e) and fig. 3.15(f).

The frequency shifts of the transition in case of σ^- polarization of the exciting radiation are demonstrated on fig. 3.15(a) and fig. 3.15(b) respectively from $F_g = 2$ and $F_g = 3$ ground states. The transitions from the ground states $F_g = 2$ and $F_g = 3$ demonstrate strong shift of the frequency in respect to their initial value. These shifts achieve ~ 40 GHz for the value of magnetic field $B = 10\ 000$ G.

The calculated dependence of the transitions intensity modification is exhibited on the fig. 3.15(c) and fig. 3.15(d) respectively from $F_g = 2$ and $F_g = 3$ ground states. The calculated curves demonstrate complex behaviour of the transitions intensity modification. There are 8

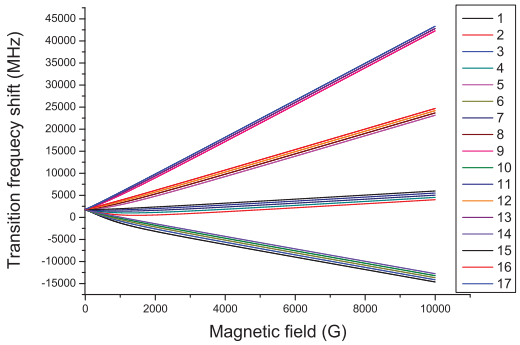

(a) The transitions frequency shift versus magnetic field, ground state $F_g = 2$.

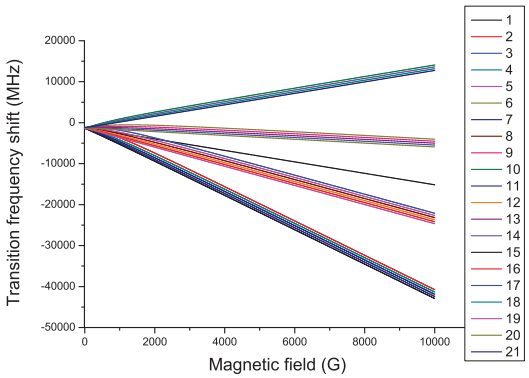

(b) The transitions frequency shift versus magnetic field, ground state $F_g = 3$.

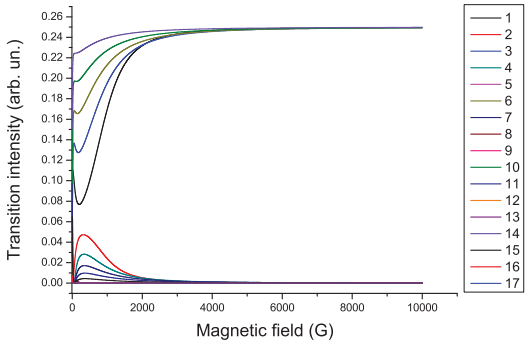

(c) The transitions intensity versus magnetic field, ground state $F_g = 2$.

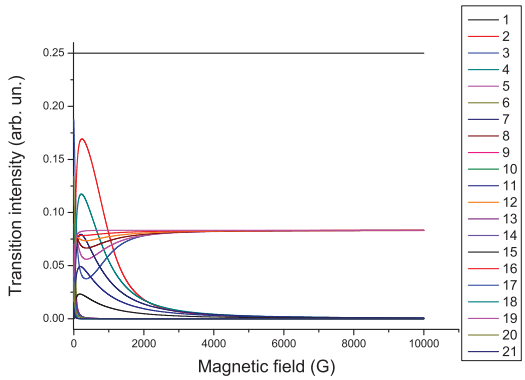

(d) The transitions intensity versus magnetic field, ground state $F_g = 3$.

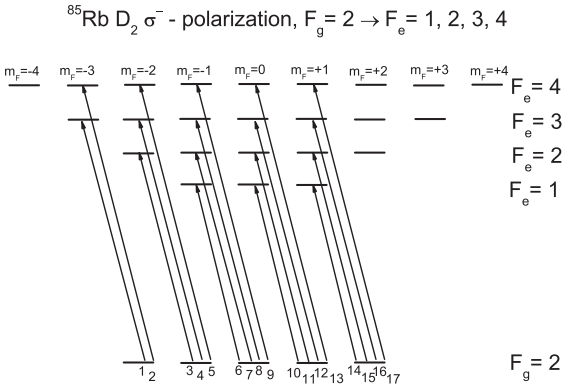

(e) The diagram of transitions from ground state $F_g = 2$.

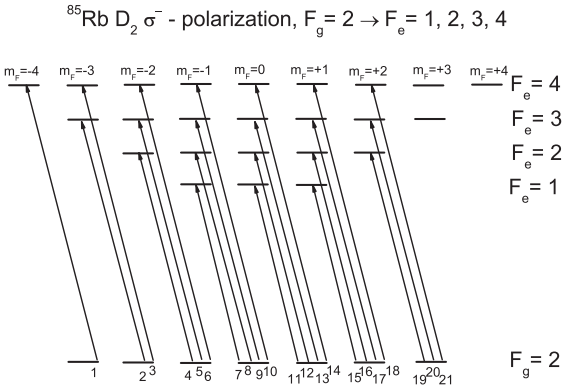

(f) The diagram of transitions from ground state $F_g = 3$.

Figure 3.15: The calculated frequency shift and intensity modification for ^{85}Rb transitions D_2 line for σ^--polarized exciting radiation.

transitions forbidden in the dipole approximation for σ^- polarization of laser radiation. Five of them correspond to the transitions from ground state $F_g = 2$: $F_g = 2, m_F = -2 \to F_g = 4, m_F = -3$, $F_g = 2, m_F = -1 \to F_g = 4, m_F = -2$, $F_g = 2, m_F = 0 \to F_g = 4, m_F = -1$, $F_g = 2, m_F = +1 \to F_g = 4, m_F = 0$ and $F_g = 2, m_F = +2 \to F_g = 4, m_F = +1$ denoted respectively 2, 5, 9, 13 and 17 on the diagram 3.15(e); and 3 transitions from the ground state $F_g = 3$: $F_g = 3, m_F = 0 \to F_g = 1, m_F = -1$, $F_g = 3, m_F = +1 \to F_g = 1, m_F = 0$ and $F_g = 3, m_F = +2 \to F_g = 1, m_F = +1$ denoted 7, 11 and 15 on the diagram 3.15(f). The transition numbered 1 from ground state $F_g = 3$ is unmixed transition, thus the intensity of this transition does not change with increasing the magnetic field value and it demonstrates a linear shift of the transition frequency in the whole range of the magnetic field.

3.4 Summary

1. It is represented theoretical description of the hydrogen-like, alkali metals atomic systems interaction with the external magnetic field.

2. The mathematical model describing theoretical background of interaction process is shown.

3. It is explained main principle of computational model, mathematical methods and principles which are in the base of our model; and numerical software which allows one to calculate the frequency shifts and intensity modifications of transitions between Zeeman sublevels of alkali metals (especially Rb) hyperfine structure D lines.

4. The frequency shifts and intensity modifications of the transitions for ^{85}Rb and ^{87}Rb, D_1 and D_2 lines in case of σ^+, π and σ^- polarizations of exciting laser radiation are considered.

5. It is represented detailed discussions about particular behaviour of different transitions between Zeeman sublevels of ^{85}Rb and ^{87}Rb, D_1 and D_2 lines in case of σ^+, π and σ^- polarizations.

6. For the first time it is demonstrated that for a certain values of the magnetic field the probability of the "forbidden" transitions (at zero magnetic field) ^{87}Rb, D_2 line, $F_g = 1 \rightarrow F_e = 3$ (three transitions between the Zeeman sublevels for a σ^+ polarization of the exciting radiation), $F_g = 1 \rightarrow F_e = 1$ and $F_g = 1 \rightarrow F_e = 3$ (one in each group of transitions between the Zeeman sublevels for a π polarization of the exciting radiation); ^{87}Rb, D_1 line, $F_g = 1 \rightarrow F_e = 1$ (one transition between the Zeeman sublevels for a π polarization of the exciting radiation), strongly increase and exceed the probability of the allowed atomic transitions. Frequency shift of the strong atomic transition ^{87}Rb, D_2 line, $F_g = 1, m_F = +1 \rightarrow F_e = 1, m_F = +1$ shows a particular behaviour: the frequency remains practically unchanged in the range of magnetic field of $100 - 1100$ G.

Chapter 4

Magneto-optical processes in nano-cell. Part II

Introduction. Alkali-metal atoms, particularly Rb atoms, are widely used in laser atomic physics because they have strong atomic transitions in a convenient range of the spectrum (near infrared), where diode lasers with good parameters are available. Rb atoms are often used in laser cooling experiments, information storage, spectroscopy, magnetometry, etc [111–113]. These atoms are of a special interest for Bose-Einstein Condensate (BEC) experiments [112]. This is why a detailed knowledge of the behaviour of Rb atomic transitions, particularly, in an external magnetic field is of a high importance.

It is well-known that atomic energy levels split in a magnetic field into Zeeman sub-levels, and frequency shifts of atomic transitions between ground and upper sub-levels (optical domain) deviate from the linear behaviour even in quite moderate magnetic field [105, 114]. Also, atomic transition intensities undergo significant changes depending on external magnetic B-field [105]. Usually, frequency separation between atomic transitions in an external magnetic field of $50-1000$ G achieves $20-200$ MHz. However, because of Doppler broadening (~ 500 MHz), in order to study separately each individual atomic transition behaviour one should implement a technique providing sub-Doppler resolution.

It is known that, with the SA technique, the sub-Doppler spectral resolution can be

reached using conventional centimeter-scale cells. In Refs. [115,116] the SA technique is used to study spectra of D_2 line of Rb atoms. However, one of the significant disadvantages of the SA technique is the presence of the CO resonances in the spectra. In a magnetic field, these resonances split into numerous components, making the spectrum very difficult to analyze. This restricts the magnitude of acceptable magnetic field below 100 G. Another disadvantage of the SA technique is the fact that, the amplitudes of VSOP resonances formed in SA spectrum do not correspond to the intensities of the corresponding atomic transitions. This additionally strongly complicates the analysis of spectra. Note, that sub-Doppler spectral resolution could be obtained by using expensive and complicated systems based either on cold and trapped atoms or with the help of sufficiently well collimated Rb atomic beam propagated in vacuum conditions.

Recently, it has been demonstrated that a one-dimensional nano-cell filled with Rb atoms is a very convenient tool to obtain sub-Doppler spectral resolution when the thickness L of atomic vapour column is either $L = \lambda/2$ or $L = \lambda$, where λ is the laser radiation wavelength resonant with the Rb D_1 or D_2 lines ($\lambda = 794$ nm or 780 nm). In case of the thickness $L = \lambda/2$ it is more convenient to use the fluorescence spectrum of the nano-cell since the spectrum linewidth is $7-8$ times narrower than that of the Doppler width obtained with a conventional cm-size Rb cell. The method is called "half-λ Zeeman technique" (HLZT) [7, 117, 118].

In case of the thickness $L = \lambda$ spectrally-narrow VSOP resonances appear at laser intensities ~ 10 mW/cm^2 in the transmission spectrum of the nano-cell. The formation of VSOP resonances with the help of nano-cell has several advantages in comparison with the SA technique: i) the absence of cross-over resonances, which is very important for some applications, particularly, when an external magnetic field is applied; ii) the ratio of amplitudes of VSOP resonances is close to the ratio of the corresponding atomic transition intensities; iii) a single beam transmission is used; iv) the laser power required for the formation of VSOP resonances is as low as 0.1 mW. In a magnetic field these VSOP resonances are split into several new components, the number of which depends on the quantum numbers F of the lower and upper levels, while the amplitudes and frequency positions of the components depend on

the B-field magnitude. This method allows one to study separately each individual atomic transition behaviour ("λ-Zeeman technique" (LZT)) [8–10, 88].

Below are presented the results of the experimental study of the ^{85}Rb and ^{87}Rb, $D_{1,2}$ lines atomic transitions, including "forbidden" transitions for σ^+, π and σ^--polarizations of the exciting laser radiation. For this study Rb a nano-cell is placed in a strong external magnetic field B varying in the range of $5-7000$ G. A theoretical model described in Chapter 3 is used to explain the experimental results.

4.1 The nano-cell transmission for $L = \lambda$ in a external magnetic field, LZT method

As written in previous section, energy levels of atoms placed in an external magnetic field undergo frequency shifts and changes in their transition intensities. These effects were studied for hyperfine components of atomic optical transitions in the transmission spectra obtained with an ordinary centimeter-size cell containing Rb and Cs vapour in Ref. [105]. However, because of Doppler broadening (hundreds of MHz), it was possible to partially separate different hyperfine transitions only for $B > 1500$ G. Note that even for these large B values, the lines of ^{87}Rb and ^{85}Rb are strongly overlapped, and pure isotopes have to be used to avoid complicated spectra. In order to eliminate the Doppler broadening, in [115] the SA technique was implemented to study the Rb hyperfine transitions. However, in this case the complexity of the Zeeman spectra in a magnetic field arises primarily from the presence of CO resonances, which are also split into many components. That is why, as mentioned in Ref. [115], the SA technique is applicable only for $B < 50$ G. The CO resonances can be eliminated with selective reflection spectroscopy [114], but to correctly determine the hyperfine transition position, the spectra must undergo further nontrivial processing. Another method based on the fluorescence spectrum emitted from a nano-cell at thickness $L = \lambda/2$ was presented in Ref. [117, 118]. This point will be more precisely

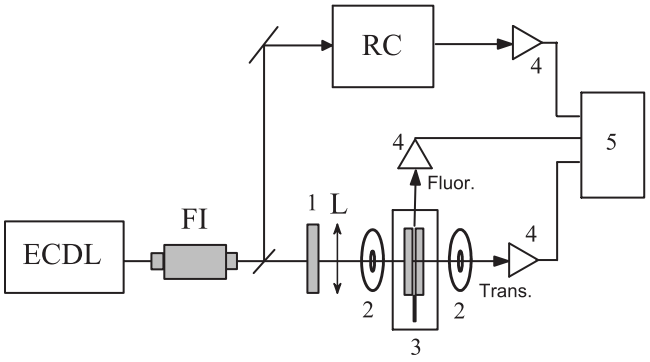

Figure 4.1: Sketch of experimental setup. FI - Faraday Isolator, L - lens, RC - reference cell, 1 - $\lambda/4$-plate, 2 - PRM, 3 - nano-cell and oven, 4 - photodetectors, 5 - digital storage oscilloscope.

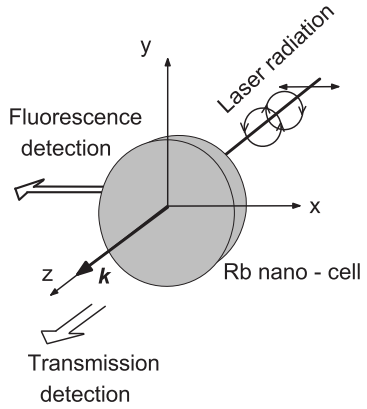

Figure 4.2: Scheme of detection.

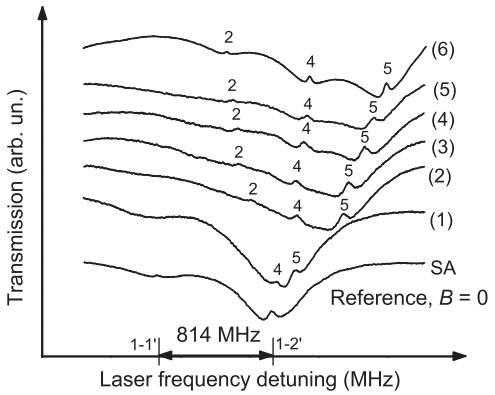

Figure 4.3: Nano-cell transmission spectra for $L = \lambda$ for different values of the magnetic field $B = 140$, 405, 440, 515, 555 and 590 G respectively for curves (1) - (6).

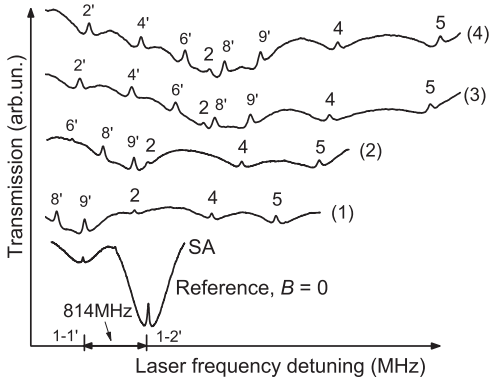

Figure 4.4: Nano-cell transmission spectra for $L = \lambda$ for different values of the magnetic field $B = 1170$, 1540, 2300 and 2400 G respectively for curves (1) - (4).

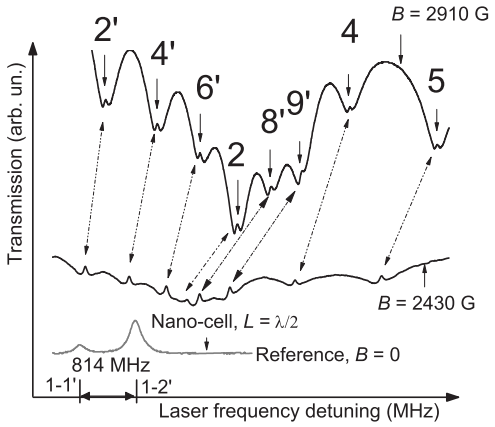

Figure 4.5: Nano-cell transmission spectra for $L = \lambda$ in the case of σ^+ excitation at $B = 2910$ G (the upper curve) and $B = 2430$ G (middle curve).

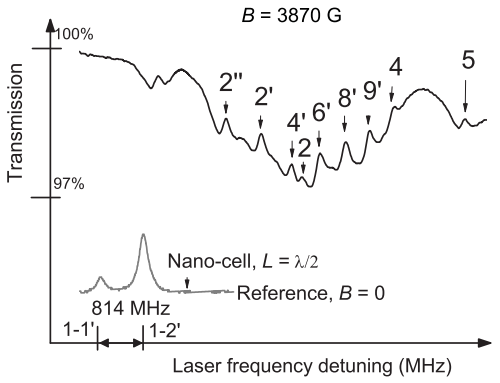

Figure 4.6: Nano-cell transmission spectrum for $L = \lambda$ in the case of σ^+ excitation at 3870 G (the upper curve).

discussed later. Coherent population trapping (CPT) allows to study the behaviour of hyperfine transitions in a magnetic field with very high accuracy (several kilohertz) [71], however the experimental realization is complicated. Moreover, measuring hyperfine level shifts of several gigahertz for $B \sim 1000$ G using CPT is not realistic.

We present a method based on narrow (close to natural linewidth) VSOP resonance peaks of reduced absorption located at the atomic transitions [6, 8–11]. As was shown in Ref. [42], the ratio L/λ is a significant parameter for VSOP resonance formation. The VSOP peaks appear at laser intensity ~ 1 mW/cm^2 in the transmission spectrum of the nano-cell with atomic vapour column of thickness $L = \lambda$. At $B > 0$, the VSOP resonance is split into several Zeeman components, the number of which depends on the quantum numbers F of the lower and upper levels. The amplitudes of these peaks and their frequency positions depend unambiguously on the B value. This so-called λ-Zeeman technique (LZT) allows one to study not only the frequency shift of any individual hyperfine optical transition, but also the modification in transition intensity in the region of $10 - 7000$ G. Possible applications of a nano-cell for diagnostics and mapping of large magnetic gradients and for making widely tunable compact frequency references are addressed too.

Experimental realization of LZT is rather simple. The sketch of experimental setup is shown on fig. 4.1 and detection scheme is shown on fig. 4.2. The circularly polarized beam of an extended cavity diode laser ($\lambda = 794$ nm, $P_L \sim 5$ mW, $\gamma_L < 1$ MHz) resonant with the ^{87}Rb D_1 transition frequency, after passing through a Faraday isolator, was focused (diameter ≈ 0.5 mm) onto a Rb nano-cell with a vapour column of thickness $L = \lambda$ at an angle close to the normal incidence. The design of a nano-cell is presented in section 1.4. The source temperature of the atoms of the nano-cell was 110 °C, corresponding to a vapour density $N \sim 10^{13}$ at/cm^3, but the windows were maintained at a temperature that was 20 °C higher. Part of the laser radiation was diverted to a centimeter-size Rb cell (denoted RC on fig. 4.1) to obtain a SA spectrum for $B = 0$, which served as frequency reference. The nano-cell transmission and SA spectra were detected by photodetectors and recorded by a digital storage oscilloscope. Moderate longitudinal magnetic field ($B < 250$ G) was applied

to the nano-cell by a system of Helmholtz coils (not shown in fig. 4.1). The B-field strength was measured by a calibrated Hall gauge. It is important to note that the use of the nano-cell allows one to apply very strong magnetic fields using widely available strong permanent ring magnets (PRM): in spite of strong inhomogeneity of the magnetic field (in our case it can reach 150 G/mm), the variation of B-field inside the atomic vapour column is ~ 0.1 G, i.e. by several orders less than the applied B value, thanks to small thickness of the nano-cell ($L = 794$ nm).

The allowed transitions between magnetic sublevels of hyperfine states for the ^{87}Rb D_1 line in the case of σ^+ (left circular) polarized excitation are depicted in fig. 3.4(e) (LZT also works well for σ^- excitation). Figure 4.3 shows the nano-cell transmission spectra for the $F_g = 1 \rightarrow F_e = 1, 2$ transitions at different values of B (the labels denote corresponding transitions shown in fig. 3.4(e)). As shown, all the individual Zeeman transitions are clearly detected. The two transitions $F_g = 1, m_F = -1 \rightarrow F_e = 1, m_F = 0$ and $F_g = 1, m_F = 0 \rightarrow F_e = 1, m_F = +1$ (not shown in fig. 4.3) are detectable for $B < 120$ G, while at higher B their intensities are strongly reduced (this is also confirmed theoretically (see fig. 3.4(c)). Note that the absence of CO resonances in transmission spectra is an important advantage of the nano-cell [8].

Transmission spectra for larger B values are presented in fig. 4.4. On spectrum 4.4 the transitions between Zeeman sublevels of the ^{85}Rb D_1 line are seen as well. These transition are denoted with primed numbers. Numbering of the transition on the spectrum corresponds to numbering of the transitions of the ^{85}Rb D_1 line in fig. 3.7(e). The strong magnetic field was produced by two PRM of diameter 50 mm, with 3 mm holes to allow radiation to pass, placed on opposite sides of the nano-cell oven and separated by a distance that was varied between 25 and 50 mm (see fig. 4.1). To control the magnetic field value, one of the magnets was mounted on a micrometric translation stage for longitudinal displacement. In particular, the B-field difference of curves (4) and (3) (see fig. 4.4) is obtained by a PRM displacement of 0.67 mm, corresponding to a rate of 150 G/mm. The frequency difference between the VSOP peaks numbered 5 (curves (4) and (3)) for this case is 160 MHz. By a 20 μm displacement of the

PRM, it is easy to detect a 3 MHz frequency shift of peak 5. The advantage of a submicron-size magnetic field probe can be fully exploited for the case of a larger B-field gradient as well as after further optimization of the method (reduction in laser intensity, implementation of frequency modulation, lock-in detection, etc.). An important advantage of LZT is that the amplitude of VSOP peaks is linearly proportional to the corresponding Zeeman transition intensity, which offers the possibility to quantitatively study the modification of individual Zeeman transition intensities in a magnetic field. Thus, in weak magnetic fields ($B \approx 0$), the intensities of transitions labeled 5, 4, and 3 compose the ratio $6:3:1$, which varies rapidly as B increases.

The aim of the work is to demonstrate that LZT can also be successfully used for even higher external magnetic fields. On fig. 4.5 are presented spectra of transmission for two values of magnetic field. The oblique arrows indicate the positions of the VSOP resonances with the labels 2, 4, 5 (fig. 3.4(e)) and $2'$, $4'$, $6'$, $8'$ and $9'$ (fig. 3.7(e)) for $B = 2430$ and 2910 G. As seen from fig. 4.5 for magnetic field measurement the most convenient is the VSOP peak number 5 (^{87}Rb, $F_g = 1$, $m_F = +1 \rightarrow F_e = 2$, $m_F = +2$), since it has the largest peak amplitude among transitions 2, 4 and 5 of the ^{87}Rb and it is not overlapped with any other transition, while having a strong detuning value versus magnetic field strength of ~ 1.8 MHz/G. It is important to note that LZT allows one to check whether the VSOP resonance (i.e. peak of reduced absorption) is a real one or has an artificial/noise nature. For this purpose one should simply increase the side-arm temperature by additional $20 - 30$ °C in order to provide larger absorption in the transmission spectrum. The real VSOP must be located exactly at the bottom of the absorption at the position of the corresponding atomic transition shifted in the magnetic field, as it is shown on the upper curve of fig. 4.5 (the side-arm temperature is 140 °C).

The nano-cell transmission spectrum for the thickness $L = \lambda$, for the ^{85}Rb and ^{87}Rb, D_1 line in the case of σ^+ excitation at $B = 3870$ G (the upper curve) are presented in fig. 4.6. The labels 2, 4, 5 (^{87}Rb); $2'$, $4'$, $6'$, $8'$, $9'$ (^{85}Rb $F_g = 2$) and $2''$ (^{85}Rb $F_g = 3$) denote the corresponding transitions between the magnetic sublevels shown correspondingly

in fig. 3.4(e), 3.7(e) and 3.7(f). The lower grey curve presents the fluorescence spectrum of the nano-cell of $L = \lambda/2$, which is the reference spectrum for the case $B = 0$. A new VSOP with label $2''$ is seen in the spectrum (the corresponding atomic transition is shown in fig. 3.7(f)), while it was absent for the case of smaller B-field shown in fig. 4.5. As it is seen from fig. 4.6 the most convenient is still the VSOP peak number 5 for magnetic field measurement.

The following control experiment was carried out: one of the PRM was set on the table with the micrometer step. In the magnetic field ~ 4000 G, one PRM was shifted toward the other by the displacement of PRM of 15 μm leading to the frequency shift of component 5 by 4 MHz to the high frequency region, which was relatively easily detected.

The nano-cell transmission spectra for thickness $L = \lambda$, for the ^{85}Rb and ^{87}Rb, D_1 line in the case of σ^+ excitation at $B = 4770$ G (the upper curve) is presented in fig. 4.7. The labels $2,\ 4,\ 5$ (^{87}Rb); $2',\ 4',\ 6',\ 8',\ 9'$ (^{85}Rb $F_g = 2$) and $2''$ (^{85}Rb $F_g = 3$) denote the corresponding transitions between the magnetic sublevels shown correspondingly in fig. 3.4(e), 3.7(e) and 3.7(f). The lower grey curve presents the fluorescence spectrum of the nano-cell of $L = \lambda/2$, which is the reference spectrum for the case $B = 0$. As it is seen from fig. 4.7 the VSOP peak number 5 is still the most convenient for magnetic field measurement.

We note that transition 5 is strongly shifted by ~ 7.7 GHz from the $B = 0$ position of the $F_g = 1 \to F_e = 2$ transition. The latter allows to develop a frequency reference based on a nano-cell and PRM, widely tunable over a range of several gigahertz onto high-frequency wing of transition of ^{87}Rb atom by simple displacement of the magnet.

Fig. 4.8(a) shows the frequency shift of components 2, 4 and 5 (see diagram in fig. 3.4(e)) relatively to their initial position at $B = 0$. Fig. 4.8(b) shows the intensity for the atomic transitions 2, 4, 5 (i.e. the atomic line intensity) for the case of σ^+ excitation versus magnetic field (theory). However, in the experiment it is more convenient to measure the ratio of the VSOP amplitudes $A(2)$, $A(4)$ and $A(5)$ of transitions 2, 4 and 5 versus B (shown in fig. 4.8(b)), since the absolute value of the VSOP amplitude depends on laser intensity, nano-cell temperature, etc. Note that for $B \approx 0$ the ratios $A(5) : A(4) : A(2) = 6 : 3 : 1$,

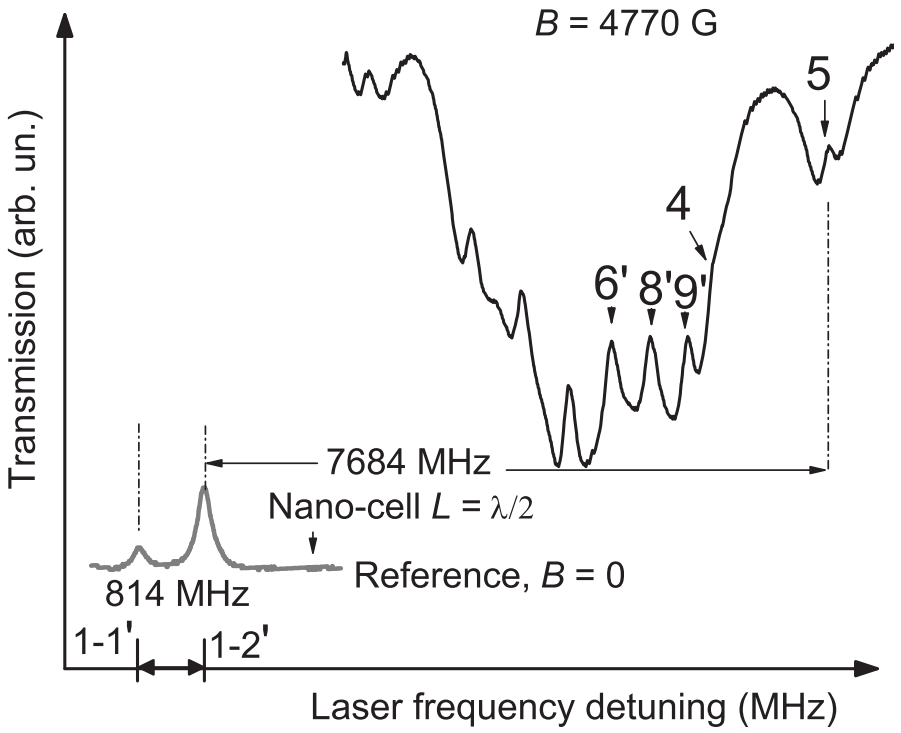

Figure 4.7: Nano-cell transmission spectra for $L = \lambda$ for the ^{85}Rb and ^{87}Rb D_1 line in the case of σ^+ excitation at $B = 4770$ G (the upper curve).

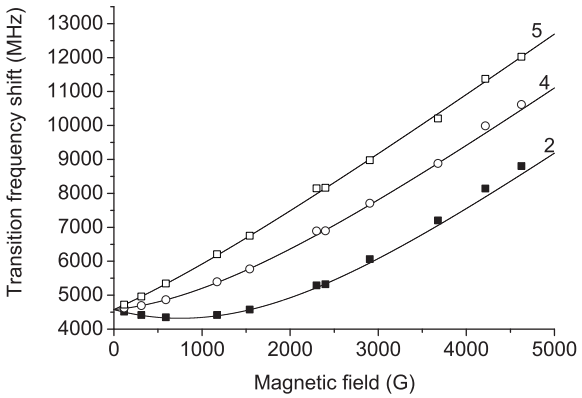

(a) Transition's frequency shift of components 5, 4 and 2 relatively to the initial position at $B = 0$, solid line is the theory.

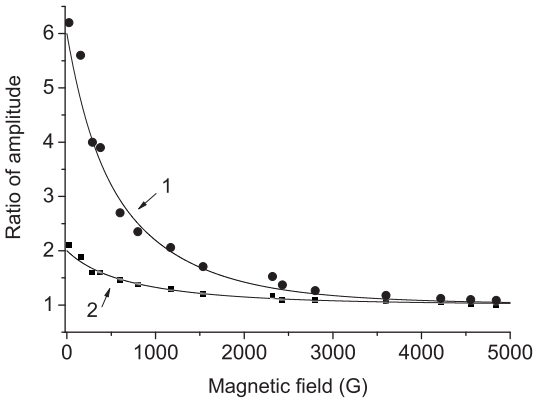

(b) The intensity for the atomic transitions 2, 4, 5 in the case of σ^+ excitation, curve 1 shows the ratio of the amplitudes $A(5)/A(2)$ and curve 2 shows the ratio of the amplitudes $A(5)/A(4)$ versus B.

Figure 4.8: Comparison of the theoretically calculated data with the experimental results.

while for large B, these ratios become $A(5) \approx A(4) \approx A(2)$. Also, as it is seen for B up to 5000 G the VSOP amplitude $A(5)$ is increasing, which makes it convenient to use VSOP with label 5 for a magnetic field measurement.

4.2 Fluorescence of an nano-cell with $L = \lambda/2$ in external magnetic field, HLZT method.

Below it is demonstrated that using fluorescence spectra from an nano-cell with thickness $L = \lambda/2$, it is possible to efficiently study the above mentioned changes: transition frequency shift and transition intensity modification (so called "$\lambda/2$-Zeeman technique") [7,12,13]. The fluorescence emitted by an nano-cell with $L = \lambda/2$ has an advantages of narrow sub-Doppler spectral width (~ 70 MHz) and zero detection off-resonance background [117].

Sketch of the experimental setup is similar with the one used for LZT presented in fig. 4.1. The circularly polarized beam of extended cavity diode laser (ECDL, $\lambda = 794$ nm, $P_L \sim 30$ mW, $\lambda_L < 1$ MHz) resonant with ^{87}Rb D_1 transition frequency was directed onto the Rb nano-cell with the thickness of vapour column $L = \lambda/2$, at an angle close to the normal incidence. The needed temperature regime of the nano-cell ($T_{SA} \sim 110 - 120$ °C, $T_W \sim 140 - 150$ °C, corresponding $N \sim 6 \cdot 10^{12} - 1.5 \cdot 10^{13}$ at/cm^3) was provided by a special oven with 3 openings: 2 inlets for laser beam passage, and one orthogonal inlet for side fluorescence detection. This geometry allows simultaneous recording of fluorescence and transmission spectra. Geometrical configuration of the experiment is shown in fig. 4.2. The magnetic field is directed along the laser radiation propagation direction $\vec{k}$ ($\vec{B} \| \vec{k}$).

The allowed transitions between magnetic sublevels of hyperfine states for ^{87}Rb D_1 line in the case of σ^+ (left circular) polarized excitation and selection rules $\Delta m_F = +1$ are depicted in fig. 3.4(e) (HLZT also works well for σ^- excitation).

The fluorescence spectra of the ^{87}Rb, $5S_{1/2}, F_g = 1 \rightarrow 5P_{1/2}, F = 1, 2$ and ^{85}Rb $5S_{1/2}, F_g = 2 \rightarrow 5P_{1/2}, F = 2, 3$ for the case of different values of longitudinal magnetic field B, with σ^+ laser radiation excitation are presented in fig. 4.9. The laser power is 2 mW and beam

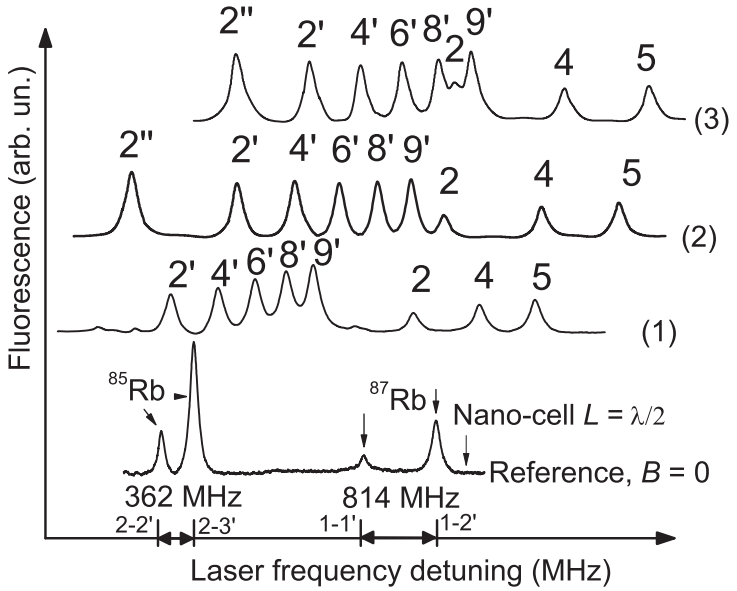

Figure 4.9: Fluorescence spectra obtained with nano-cell of $L = \lambda/2$ for different values of the magnetic field $B = 830,\ 1350$ and 1875 G respectively for curves (1), (2) and (3). Lower curve is the reference spectrum for $B = 0$.

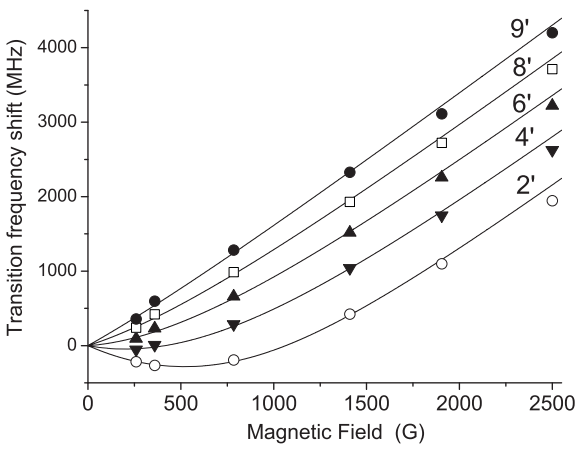

(a) Frequency shift of the fluorescence peaks 2', 4', 6', 8', 9' relatively to the initial frequency position (for $B = 0$). Theoretical curves are shown by solid lines.

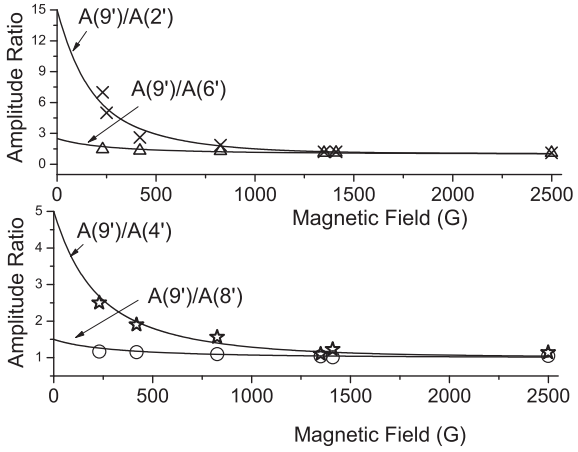

(b) Ratio of the fluorescence peak's amplitude under number 2', 4', 6', 8' relatively to the amplitude of the peak number 9'.

Figure 4.10: Comparison of the theoretically calculated data with the experimental results.

diameter is 2 mm. For the convenience spectra are shifted vertically. The lower curve is the fluorescence spectrum for $B = 0$. It is easy to identify all nine transitions. The labels 2, 4, 5 (^{87}Rb); $2'$, $4'$, $6'$, $8'$, $9'$ (^{85}Rb $F_g = 2$) and $2''$ (^{85}Rb $F_g = 3$) denote the corresponding transitions between the magnetic sublevels shown correspondingly in fig. 3.4(e), 3.7(e) and 3.7(f). Note, that the fluorescence amplitude of the individual transition is proportional to its intensity. It is interesting to note also, that the intensity of the fluorescence peak amplitude under number $2'$ is increasing rapidly with B, and for $B \sim 1000$ G the ratio of the fluorescence peak amplitude under number $9'$ and $2'$ is equal to $A(9')/A(2') \sim 1$, meanwhile the initial ratio $A(9')/A(2') \sim 15$ (for $B = 0$). As it is seen in fig. 4.9, for the magnetic field measurement the most convenient is the fluorescence peak under number 5 (^{87}Rb, $F_g = 1, m_F = +1 \rightarrow F = 2, m_F = +2$ transition), since it has the largest peak amplitude among transitions 2, 4, 5. Also, the fluorescence peak under number 5 is not overlapped with any other transitions for any value of the magnetic field strength B.

In fig. 4.10(a) the frequency shift of the fluorescence peaks 2', 4', 6', 8' and 9' relatively to the initial frequency position (for $B = 0$) is shown. Theoretical curves are shown by solid lines and indicated a good agreement with experimental data.

For low magnetic field the intensity for the fluorescence peaks under number 2', 4', 6', 8' and 9' are strongly different (the maximum one is for 9'), however they are increasing with the magnetic field and practically became equal to each other. In fig. 4.10(b) it is shown the ratio of the intensities for the fluorescence peaks under number 2', 4', 6', 8' relatively to the amplitude of peak number 9'. Theoretical curves are shown by solid lines and as it is seen there is a good agreement.

It is interesting to note, that at a moderate magnetic field $B = 250$ G all nine components of the $5S_{1/2}, F_g = 2 \rightarrow 5P_{1/2}, F = 2, 3$ transitions (shown in diagram fig. 3.7(e)) are well resolved (fitting is provided by nine Lorentzian profiles - grey lines) and presented in fig. 4.11. For $B = 0$ the ratio of the intensities of the transitions under number $9' : 8' : 6' : 4' : 2'$ (σ^+ excitation) are $15 : 10 : 6 : 3 : 1$ and the intensities of the transitions under number $7' : 5' : 3' : 1'$ are $2 : 3 : 3 : 2$.

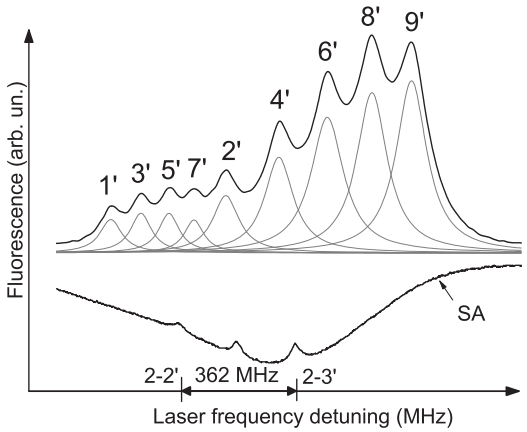

Figure 4.11: Fluorescence spectrum of all nine components of the $5S_{1/2}, F_g = 2 \rightarrow 5P_{1/2}, F = 2, 3$ transitions, $B = 250$ G.

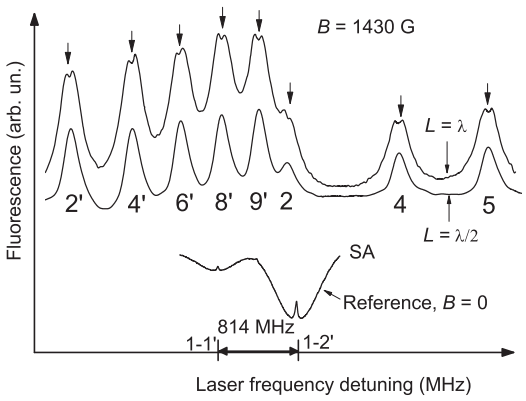

Figure 4.12: Fluorescence spectra of the $5S_{1/2}, F_g = 2 \rightarrow 5P_{1/2}, F = 2, 3$ transitions, $B = 1430$ G; upper curve for $L = \lambda$, middle curve for $L = \lambda/2$.

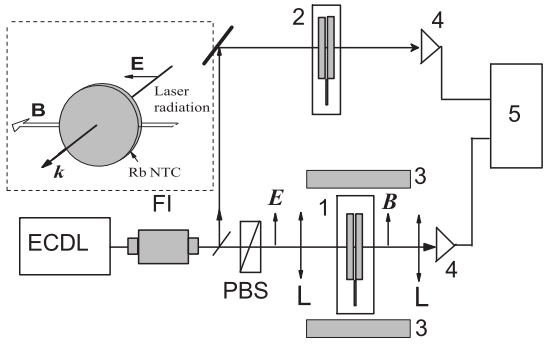

Figure 4.13: Sketch of the experimental setup. 3 - PRM, L - lenses, 4 - photodetectors, 5 - digital oscilloscope, $\vec{E}$ - electrical field of the laser radiation, $\vec{B}$ - magnetic field applied to the nano-cell.

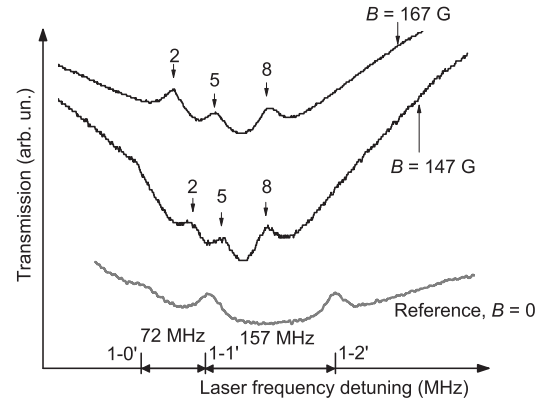

Figure 4.14: Transmission spectra from the Rb nano-cell ($L = \lambda = 780$ nm) for transitions $F_g = 1 \rightarrow F_e = 0, 1, 2, 3$ for two values of the magnetic field B: 147 G and 167 G.

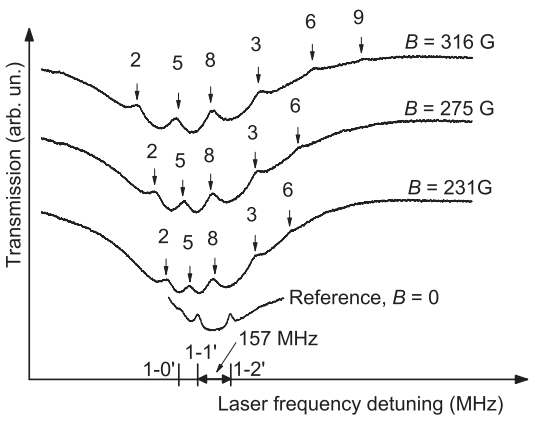

Figure 4.15: Nano-cell transmission spectra for $L = \lambda$ for atomic transitions $F_g = 1 \rightarrow F_e = 0, 1, 2, 3$.

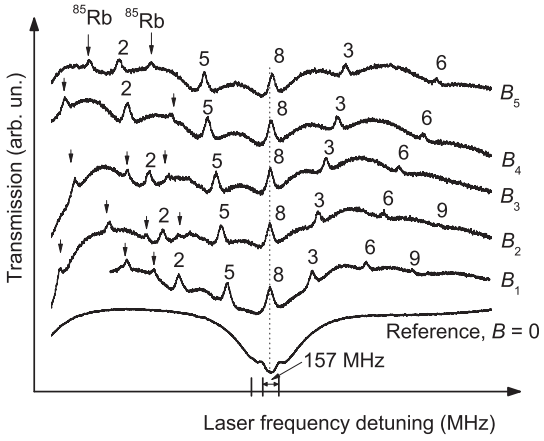

Figure 4.16: Transmission spectra for $L = \lambda$. Magnetic field $B_{1,\ 2,\ 3,\ 4,\ 5} = 700, 740, 865, 1010$ and 1080 G, correspondingly.

Thus, the HLZT allows one to study not only the frequency shift of any individual Zeeman transition, but also the modification in its transition intensity in the region of $10 - 2500$ G.

4.3 Fluorescence of an nano-cell with $L = \lambda$ in a external magnetic field, LFZT method.

As it was demonstrated in fig. 2.13 for the thickness $L = \lambda$, and relatively high laser intensity ~ 30 mW/cm^2, narrow dips (of spectral width $10 - 20$ MHz) of reduced fluorescence appear at all transitions of the Rb D_1 line in the fluorescence spectrum. It is expected that in the case of external magnetic field the splitting of the fluorescence spectrum for the thickness $L = \lambda$ will occur (as it is for the case of $L = \lambda/2$) while containing the dips of reduced fluorescence. In fig. 4.12 is presented the fluorescence spectrum of the $5S_{1/2}, F_g = 2 \rightarrow 5P_{1/2}, F = 2, 3$ transitions (8 components), for $B = 1430$ G. Upper curve for the thickness $L = \lambda$ (containing dips of the fluorescence marked by the arrows) and laser intensity ~ 30 mW/cm^2 (we call this technique "λ - Fluorescence Zeeman technique" (LFZT)). Middle curve for the thickness $L = \lambda/2$ and laser intensity ~ 10 mW/cm^2. Lower curve is the reference one obtained by the SA technique. Since LFZT provides larger peak amplitude of the fluorescence, in the case of weak transitions it could be a convenient one. Moreover, increasing the thickness L up to several λ will allow one to increase the fluorescence amplitude as it is shown in fig. 2.15. Note, that the dips of reduced fluorescence which appear exactly at the atomic transitions (see fig. 2.13) are good "markers" of the atomic transition frequency position in external magnetic field. However, the benefit of HLZT is that it provides narrower spectral width of the fluorescence which causes better spectral resolution, and thus, better accuracy of the amplitude measurement which is needed for the measurement of modification of atomic transition intensity.

4.4 Study of the "forbidden" atomic transitions on D_2 line, π-polarization.

Below are presented the results of the experimental study of the ^{87}Rb, D_2 line $F_g = 1 \rightarrow$

$F_e = 0, 1, 2, 3$ atomic transitions, including "forbidden" $F_g = 1, m_F = 0 \rightarrow F_e = 1, m_F = 0$ and $F_g = 1, m_F = -1 \rightarrow F_e = 3, m_F = -1$ transitions for π-polarized exciting laser radiation. For this study a Rb nano-cell is placed in a strong external magnetic field B varying in the range of $100 - 1100$ G.

The sketch of the experimental setup is shown in fig. 4.13. The π-polarized beam of the extended cavity diode laser (ECDL, $\lambda = 780$ nm, $P_L = 30$ mW, $\gamma_L < 1$ MHz) resonant with the ^{87}Rb, D_2 transition frequency, is focused (the laser spot diameter is ≤ 0.1 mm) at nearly normal incidence onto the Rb nano-cell 1 with the vapour column thickness $L = \lambda = 780$ nm. A polarization beam splitter (PBS) is used to purify initial linear radiation polarization of the laser. A part of the pumping radiation was directed to the auxiliary (reference) Rb nano-cell 2, which without magnetic field; transmission spectrum of this nano-cell is used as a frequency reference.

The magnetic field $\vec{B}$ is directed along the laser electric field direction $\vec{E}$ ($\vec{B} \| \vec{E}$). The configuration of the magnetic measurement is presented in the inset in fig. 4.13. The B-field strength was measured by a calibrated Hall gauge.

The atomic transitions $F_g = 1 \rightarrow F_e = 0, 1, 2, 3$ between magnetic sublevels of hyperfine states for the ^{87}Rb, D_2 line (optical domain) in the case of π-polarized laser radiation excitation are depicted in fig. 3.11(e). Note that when $B = 0$, according to the selection rules, the atomic transitions with the corresponding $\Delta F = 2$, namely $F_g = 1 \rightarrow F_e = 3$ and $F_g = 1, m_F = 0 \rightarrow F_e = 1, m_F = 0$ transitions are "electric-dipole forbidden", while all others presented transitions with $\Delta F = F_g - F_e = 0, \pm 1$ and $\Delta m_F = 0$ are allowed [44]. As it was recently shown, λ-Zeeman technique implemented in case of σ^+ (left circle) polarized excitation allows one to study separately each individual atomic transition behaviour in an external magnetic field [8, 9, 44].

As demonstrated below, the λ-Zeeman technique implemented in case of π-polarized excitation is also very convenient, since the examination of the VSOP resonances formed in the nano-cell allows one to obtain, identify, and investigate each individual atomic transition between the Zeeman sublevels in the transmission spectrum of the ^{87}Rb D_2 line in a very

wide range of magnetic fields from a few tens up to several thousands of gauss.

The two upper curves in fig. 4.14 show the transmission spectra from the Rb nano-cell $L = \lambda = 780$ nm for the magnetic field $B = 147$ G and 167 G, with π-polarized exciting laser radiation (VSOP numbers denote the corresponding transitions depicted in fig. 3.11(e)). The magnetic field is produced by Helmholtz coils (the maximum available B-field is ~ 200 G). The splitting and shifts of the three VSOP resonances 2, 5, and 8 are clearly seen in fig. 4.14. Thus, the remarkable result is that the initially "forbidden" transition $F_g = 1, m_F = 0 \rightarrow F_e = 1, m_F = 0$ labeled 5 at $B \sim 150$ G is among the three strongest atomic transitions, while the others transitions have smaller intensities, and thus are not detectable in the spectra (this is confirmed by the theory - see fig. 3.11(c)). The lower grey curve is the transmission spectrum as given by the reference nano-cell which shows the positions of the atomic transitions, i.e., the VSOP resonances (with the linewidth of ~ 20 MHz) for $B \sim 0$. We measure the atomic frequency shifts with respect to the initial position of $F_g = 1 \rightarrow F_e = 1, 2, 3$.

Figure 4.15 demonstrates the transmission spectra for the atomic transitions $F_g = 1 \rightarrow F_e = 0, 1, 2, 3$ at the following values of the magnetic field B: 231, 275 and 316 G. As mentioned earlier, a strong magnetic field is produced by two PRM (with a diameter of 50 mm) placed on the opposite sides of the nano-cell oven and separated by a variable distance. To control the magnetic field value, one of the magnets is mounted on a micrometric translation stage for longitudinal displacement. The splitting and shifts of the six VSOP resonances 2, 5, 8, 3, 6 and 9 are clearly seen. Note, that at $B \geq 230$ G the "forbidden" transition labeled 5 together with another initially "forbidden" transition $F_g = 1, m_F = -1 \rightarrow F_e = 3, m_F = -1$ labeled 3 is among the four strongest atomic transitions (this is also confirmed by the theory - fig. 3.11(c)).

Figure 4.16 shows transmission spectra for the atomic transitions for the following values of the magnetic fields, $B_{1,\ 2,\ 3,\ 4,\ 5} = 700, 740, 865, 1010$ and 1080 G, correspondingly. Again, the splitting and shifts of the six VSOP resonances 2, 5, 8, 3, 6 and 9 are clearly seen. Importantly, the both initially "forbidden" transitions labeled 3 and 5 are always among the

four strongest atomic transitions. Note, that at $B \geq 700$ G the ^{85}Rb, D_2 line, $F_g = 2 \rightarrow F_g = 1, 2, 3$ atomic transitions (marked by the vertical arrows) are also detected. However, up to ~ 1100 G the influence of the ^{85}Rb, D_2 line atomic transitions does not affect strongly the ^{87}Rb spectra. A striking point is also as follows: the variation of the magnetic field in the range of $100 - 1100$ G practically does not cause frequency shift of the $F_g = 1, m_F = +1 \rightarrow F_e = 1, m_F = +1$ atomic transition labeled 8 (this is also confirmed by the theory - fig. 3.11(c)).

The frequency shifts of the atomic transitions 2, 5, 8, 3, 6 and 9 versus magnetic B-field with respect to the initial position are presented by solid curves in fig. 4.17(a) (the corresponding initial positions at $B = 0$ are indicated by arrows). The black squares represent experimentally measured values, i.e. the frequency shifts of VSOP labeled 2, 5, 8, 3, 6 and 9 (numbers denote the corresponding transitions), while the solid lines shows the results of the theoretical calculation. As seen the theoretical model very well describes the observed experimental results. In fig. 4.17(a) are only shown the atomic transitions (represented by VSOP) that are observed in the spectra (particularly, the atomic transition $F_g = 1 \rightarrow F_e = 0$ is omitted). It is interesting to note, that the frequency of the transition labeled 8 remains practically the same in the range of $100 - 1100$ G, while g_F-factors for the ground and excited levels are -0.7 MHz/G and 0.93 MHz/G respectively. Thus, in the linear Zeeman effect (i.e. when a frequency shift is proportional to B-field) one expects to detect a shift of ~ 1600 MHz at $B = 1000$ G, while the shift is nearly zero. Obviously, this is caused by the influence of the neighboring levels. Another interesting point is that for transition labeled 6 there is a deviation from the linear Zeeman effect at small B-field values of the order of a few gauss. Note, that the atomic transition represented by VSOP labeled 2 could be convenient for external magnetic field measurements since it has a constant frequency shift of 1.28 MHz/G in the whole region $1 - 1000$ G. Also, the intensity of this atomic transition is large enough and this is displayed by the large amplitude of VSOP labeled 2. The transition labeled 9 indicates a higher constant frequency shift as compared to the transition 2, but (see fig. 4.16) its intensity (displayed by small amplitude of VSOP labeled 9) is essentially lower.

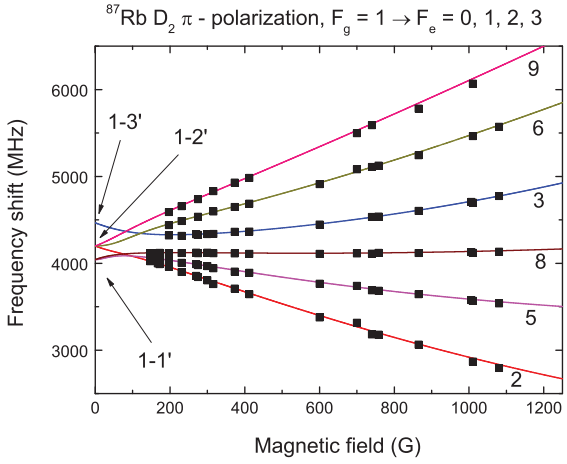

(a) Frequency shifts of components 2, 5, 8, 3, 6 and 9 versus B-field relatively to the initial position (indicated by the arrows at $B = 0$). The black squares represent the experimental results and the solid curves show the results of the theoretical calculation (numbers denote the corresponding transitions, see fig. 3.11(e))

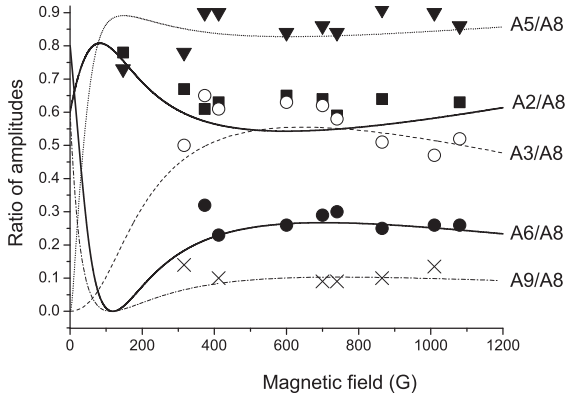

(b) The ratio of the amplitudes (i.e. ratio of the intensities) $Ai/A8$ ($i = 2, 3, 5, 6, 9$) in the case of π-excitation versus magnetic B-field: experimental points are presented by squares, hollow circles, triangles, filled circles, and crosses, correspondingly and theory by solid, dashed, dotted, solid, and dot-dashed lines, correspondingly.

Figure 4.17: Comparison of the theoretically calculated data with the experimental results.

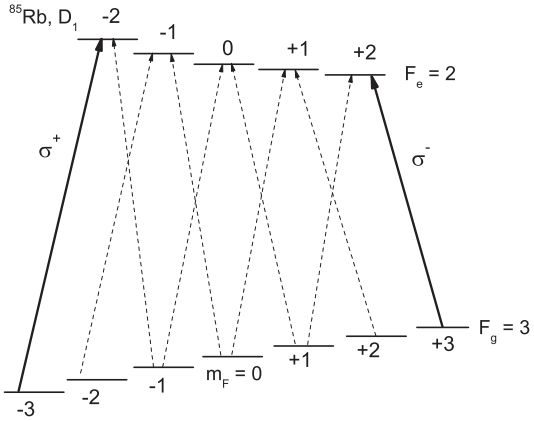

(a) System of energy levels of ^{85}Rb atoms, D_1 line, transitions $F_g = 3 \rightarrow F_e = 2$ in external magnetic field. Arrows show allowed atomic transitions. Solid arrows indicate two transitions for circular polarizations σ^+ and σ^-.

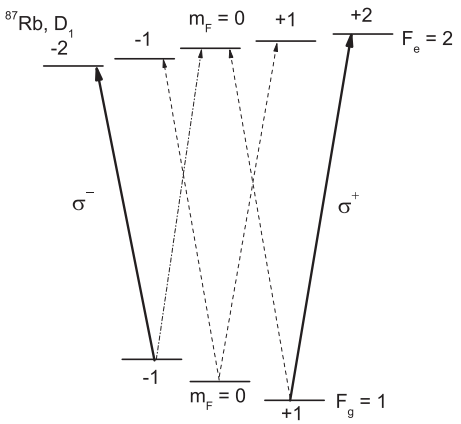

(b) System of energy levels of ^{87}Rb atoms, D_1 line, transitions $F_g = 1 \rightarrow F_e = 2$ in external magnetic field. Arrows show allowed atomic transitions. Solid arrows indicate two transitions for circular polarizations σ^+ and σ^-.

Figure 4.18: System of energy levels of $^{85,\ 87}$Rb atoms, D_1 line.

Let us now consider the change in the intensity of atomic transitions versus applied magnetic B-field. As it was demonstrated in [8–10] the change in the intensity (i.e. change of the dipole moment) causes the change in the Rabi frequency of the laser radiation and, as a consequence, the change in the efficiency of the optical pumping process. This is revealed as an increase or decrease in the corresponding VSOP resonance amplitudes presented on the spectra at Figs. (4.14-4.16). Note, that in the experiment it is more convenient to measure the ratio of the VSOP amplitudes, $A2$, $A3$, $A5$, $A6$, $A8$ and $A9$ of the corresponding transitions as a function of B, since the absolute value of the VSOP amplitude depends on the laser intensity, scan time of an atomic transition by laser radiation frequency, nano-cell temperature, etc. Consequently in fig. 4.17(b) shown are experimental (squares, hollow circles, triangles, filled circles, and crosses, correspondingly) and theoretical (by solid, dashed, dotted, solid, and dot-dashed curves, correspondingly) ratios of the $A2$, $A3$, $A5$, $A6$, $A9$ divided by $A8$ ($A8$ is chosen since the amplitude of VSOP denoted 8 changes most slowly than the others). Note, that coincidence of the experiment and the theory is not as good as it is for the frequency shifts. The explanation is as follows: since the VSOP resonance is located exactly at the atomic transition, thus a shift of the VSOP frequency displays exactly the shift of the atomic transition. As to the VSOP resonance amplitude, although it linearly depends on the intensity of the corresponding atomic transition, however some other factors can also have a slight influence on it. Note that VSOP resonances formed by the widely used SA technique are not useful for the above mentioned studies since the ratio of the amplitudes of VSOP resonances completely does not match the ratio of the corresponding transition intensities.

4.5 Measurement of weak magnetic fields.

In the present section we show that in case of exploiting the transition $F_g = 3 \rightarrow Fe = 2$ of D_1 line of ^{85}Rb, the rate of departure of two VSOP peaks is high (3.41 MHz/G) allowing one to measure weak magnetic fields, down to 5 G [14]. In this case we measure the frequency

distance between two VSOP peaks having equal amplitudes and formed by linearly polarized laser radiation. We show also that employing VSOP peaks of the same amplitudes and formed by linearly polarized laser radiation in the transition $F_g = 1 \rightarrow F_e = 2$ of D_1 line of ^{87}Rb with the two peaks departing at the rate 2.32 MHz/G is a more suitable technique for the measurements of weak magnetic fields in the range $30 - 80$ G as compared with the methods described in works [8–10]. In both transition systems under study employing linearly polarized radiation is also technically simpler, since there is no need to apply a $\lambda/4$-plate.

The diagram of experimental setup is similar with the one shown in fig. 4.1, with one differense, there is no need to use a $\lambda/4$-plate. Nano-cell was placed in the center of a system of Helmholtz coils. Magnetic field was directed along the direction of propagation of laser radiation ($\vec{B} \| \vec{k}$). Energy level diagram of ^{85}Rb, D_1 line, transitions $F_g = 3 \rightarrow F_e = 2, 3$, are shown in fig. 1.4 and in fig. 1.7 are demonstrated the transmission spectrum of nano-cell with $L = \lambda = 794$ nm for the transitions $3 \rightarrow 2', 3'$ with the frequency spacing 362 MHz; arising VSOP correspond to the $3-2'$ and $3-3'$ transitions. It is important to note that the ratio of amplitudes $A(3-2')/A(3-3') = 70/56 = 1.25$, i.e., the VSOP amplitude is proportional to the transition intensity. In experiments the $3-2'$ resonance is used as reference; its FWHM is 22 MHz. To obtain narrow VSOP the laser power was reduced down to 0.2 mW.

For the employed experimental geometry where magnetic field is directed along the propagation of laser radiation, linearly polarized radiation may be considered as two radiations with circular polarizations σ^+ and σ^- (respectively, left and right circles). Figure 4.18(a) depicts the transition $F_g = 3 \rightarrow F_e = 2$ (D_1 ^{85}Rb) in a external magnetic field and the allowed atomic transitions between Zeeman sublevels for which the selection rules for quantum numbers F ($F_g - F_e = \Delta F = 0, \pm 1$) and m_F ($\Delta m_F = \pm 1$) are valid [44]. Solid arrows show two transitions with circular polarizations σ^+ and σ^-, which are most interesting because they have the highest probabilities and the largest spacing.

It is easy to see that the frequency distance between the pair of transitions σ^+ and σ^- (marked by solid arrows) is the largest among all other pairs and amounts to $\Delta = B(\mathrm{G}) \times 3.41$ MHz/G. In the transmission spectrum the amplitudes of these two resonances

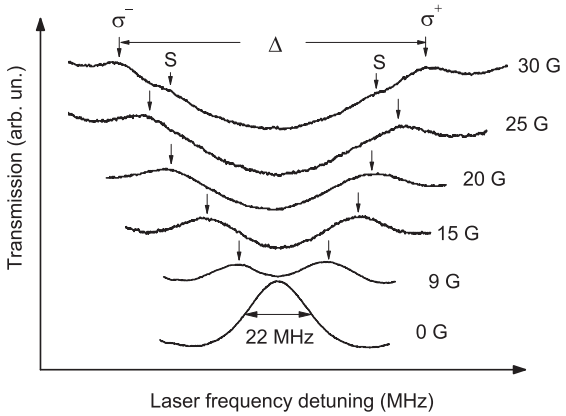

(a) Transmission spectra of nano-cell ($L = 794$ nm) in D_1 line of ^{85}Rb for atomic transitions with polarizations σ^+ and σ^- at different values of magnetic field B: 9, 15, 20, 25 and 30 G.

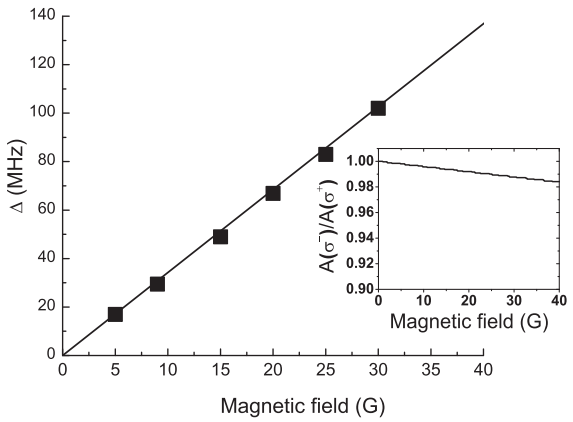

(b) Comparison of theoretical and experimental results for D_1 line of ^{85}Rb: Solid line - theoretical curve of magnetic field dependence of the frequency interval Δ; squares depict the experimental results.

Figure 4.19: Theoretical and experimental results for D_1 line of ^{85}Rb.

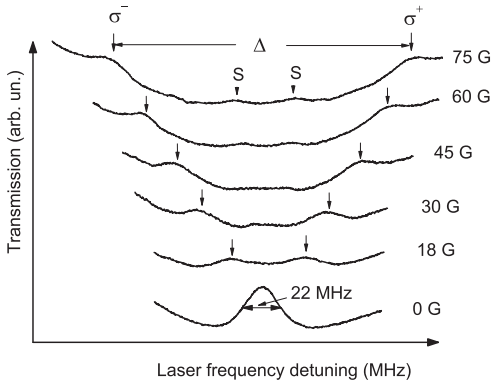

(a) Transmission spectra of nano-cell ($L = 794$ nm) in D_1 line of ^{87}Rb for atomic transitions with polarizations σ^+ and σ^- at different values of magnetic field B: 18, 30, 45, 60 and 75 G.

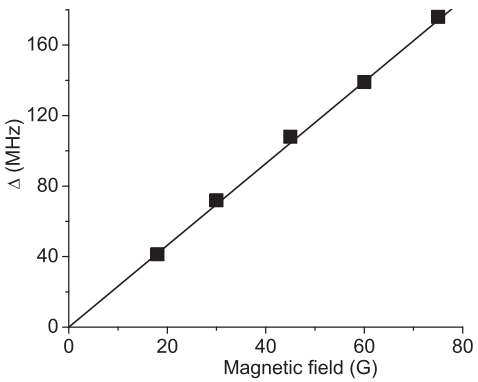

(b) Solid line - theoretical curve of magnetic field dependence of of frequency spacing Δ between VSOP-σ^+ and VSOP-σ^-. Squares indicate the experimental results.

Figure 4.20: Theoretical and experimental results for D_1 line of ^{87}Rb.

have equal amplitudes: $A(\sigma^+) = A(\sigma^-)$. Figure 4.19(a) shows transmission spectra for σ^+ and σ^- transitions and different values of magnetic field B: 9, 15, 20, 25, and 30 G. Frequency distance Δ is determined between the peaks (marked in the figure by arrows). The lower resonance (transition $3 - 2'$) is the reference peak ($B = 0$) with spectral width 22 MHz. We note that the lowest value of B, for which the dip between the two VSOP is reliably recorded is 5 G with $\Delta \approx 17$ MHz.

It is important to note that the value 3.41 MHz/G is obtained with the assumption that the Zeeman effect is linear. It is, however, well known that the linear dependence may break even in moderate magnetic fields. Besides, the intensities of atomic transitions may be strongly B-dependent. Therefore, with the model employed in a number of works [10, 107, 119], we obtained curves, which accurately describe the behaviour of both frequency shifts and corresponding transition intensities. Depicted in fig. 4.19(b) is the theoretical curve of the B-dependence of the frequency interval Δ. It is seen that up to 40 G the observed dependence is linear; deviations are observed only at high values: so, for $B = 200$ G the value 3.41 MHz/G increases by 3%. Constance of this quantity is convenient for practical application because there is no need to use the B-dependence curve of Δ. The inset on fig. 4.19(b) demonstrates the theoretical curve of the B-dependence of the ratio of amplitudes $A(\sigma^-)/A(\sigma^+)$. This ratio is seen to be practically unity up to $B < 30$ G, however with the increase of B it decreases monotonically and at 200 G it is equal to 0.9. In fig. 4.19(a), note that already at $B = 30$ G, close to the main peaks VSOP-σ^+ and VSOP-σ^- satellite peaks VSOP-σ^+-s and VSOP-σ^--s appear marked with s-letter. These peaks are due to the transitions $F_g = 3, m_F = 2 \to F_e = 2, m_F = 1$ and $F_g = 3, m_F = +2 \to F_e = 2, m_F = +1$.

It is known that by means of SA technique with centimeter-long cells also sub-Doppler spectral resolution is achieved. One of the essential shortcomings of the SA technique is the presence of CO resonances (whose frequencies are exactly in the middle between the VSOP and have as a rule higher amplitudes). These CO resonances, like VSOP, are split in the magnetic field into a large number of components and the spectrum becomes extremely complicated to analyze. The analyzes of the spectrum, full of the additional strong components

(introduced by CO resonances), seems to be a difficult and ambiguous problem (at $B > 100$ G the spectrum becomes complicated to such extent that its attribution is practically impossible). In the Ref. [120] the SA technique was employed for measuring magnetic fields with use of ^{85}Rb levels (D_1 line) as in fig. 4.18(a). As in our case, the frequency interval was measured between the σ^+ and σ^- peaks.

For measuring fields 30 G $< B <$ 80 G, exploiting the D_1 line $F_g = 1 \rightarrow F_e = 2$ transitions of ^{87}Rb (see fig. 1.4) with linearly polarized laser radiation is more suitable. Figure 4.18(b) shows the same, $F_g = 1 \rightarrow F_e = 2$ transitions in external magnetic field and allowed atomic transitions between Zeeman sublevels. Arrows show all possible transitions. Solid arrows show two transitions with circular polarizations σ^+ and σ^-, which are most interesting because they have the highest probabilities. It is easy to see that the frequency distance between the pair of transitions σ^+ and σ^- is the largest among all other pairs and amounts to $\Delta = B(\text{G}) \times 2.32$ MHz/G. Figure 4.20(a) shows transmission spectra for σ^+ and σ^- transitions and different values of magnetic field B: 18, 30, 45, 60, and 75 G. Frequency distance is determined between the corresponding peaks (marked in the figure by arrows). The lower resonance (transition $1 - 2'$) is the reference peak ($B = 0$) with spectral width 22 MHz.

Note that already at $B > 40$ G satellites (marked with letter s) appear next to the main VSOP-σ^+ and VSOP-σ^- peaks. These are due to transitions $F_g = 1, m_F = 0 \rightarrow F_e = 2, m_F = +1$ and $F_g = 1, m_F = 0 \rightarrow F_e = 2, m_F = +1$. At low values of B the satellite amplitudes are half as high as the main peak amplitudes, but with increase of B their amplitudes increase and become nearly equal to those of main peaks. Depicted in fig. 4.20(b) is the theoretical curve of the B-dependence of the frequency interval Δ. It is seen that up to 80 G the observed dependence is linear; deviations are observed only at high values: so, for $B = 300$ G the value 2.32 MHz/G increases by 3%.

As follows from theoretical consideration, the amplitudes $A(\sigma^-)$ and $A(\sigma^+)$ are practically equal up to 100 G, however at further increase in B the amplitude $A(\sigma^-)$ rapidly decreases. Another shortcoming of this method at strong fields is the frequency shift of

VSOP-σ^- towards the low-frequency range where strong VSOP are present coming from atomic transitions of ^{85}Rb D_1 line. Therefore for the measurement of strong magnetic fields (up to 5000 G [8, 10]) the use of VSOP-σ^+ (marked in fig. 4.18(b) by solid arrow) is most suitable.

It should be noted that with the use of electromagnetically-induced transparency (EIT) in atomic vapour of alkali metals, it is possible to determine significantly lower values of magnetic fields, 1 mG [121], but in order to achieve a so high sensitivity it is necessary to use two phase-correlated laser radiations, which is far not trivial problem. We perform now comparison with the results of work [122] where the EIT resonance was formed by means of two independent diode lasers with the same, as in our work, system of ^{87}Rb levels (D_1 line). Usual Rb cell with $L = 5$ cm was used and it was shown that the EIT resonance enables one to measure magnetic fields as weak as $2 - 3$ G. If we compare with described results using nano-cell, an advantage should be mentioned: the cell with $L = 5$ cm used in [122] enables measuring only homogeneous magnetic fields, whereas in our case with submicron-thick atomic vapour column, the LZT may successfully be applied for even strongly inhomogeneous magnetic fields.

So, by exploiting LZT and atomic transitions of D_1 line of rubidium with linearly or circularly polarized laser radiation, the range of measuring magnetic fields may be extended to $5 - 5000$ G.

4.6 Hyperfine Paschen-Back regime in Rb nano-cell

A simple and efficient scheme based on one-dimensional nanometric thin cell filled with Rb and strong permanent ring magnets allowed direct observation of hyperfine Paschen-Back (HPB) regime on D_1 line in $0.5 - 0.7$ T magnetic field. Miniaturization of alkali vapour cells is important for many applications [8, 10, 123, 124]. In this section we describe a simple and robust system based on nano-cell and permanent magnets, which allows of achieving magnetic field up to 0.7 T sufficient to observe a hyperfine Paschen-Back regime [15,106]. The magnetic

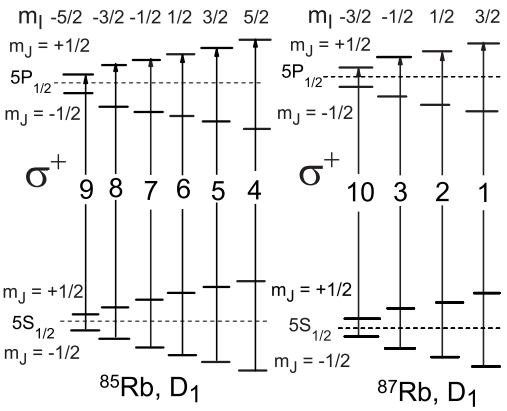

(a) Diagram of ^{85}Rb ($I = 5/2$) and ^{87}Rb ($I = 3/2$) transitions for σ^+ laser excitation in HPB regime. The selection rules: $m_J = +1$; $m_I = 0$.

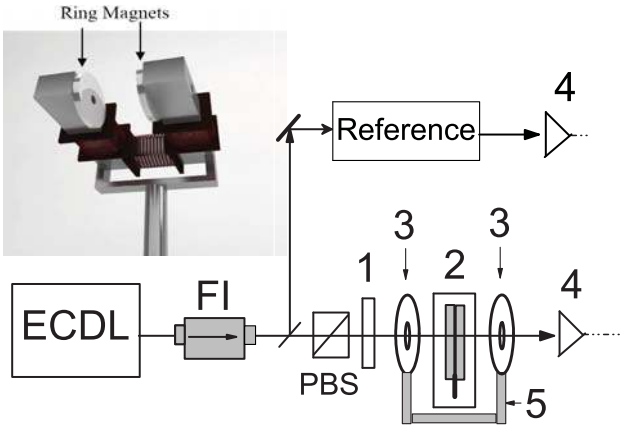

(b) Sketch of the experimental setup. ECDL - diode laser, FI - Faraday Isolator, 1 - $\lambda/4$ plate, 2 - nano-cell in the oven, PBS - polarizing beam splitter, 3 - permanent ring magnets, 4 - photodetectors, 5 - stainless steel Π-shape holder (shown in the inset).

Figure 4.21: Diagram of transitions and the sketch of the experimental setup.

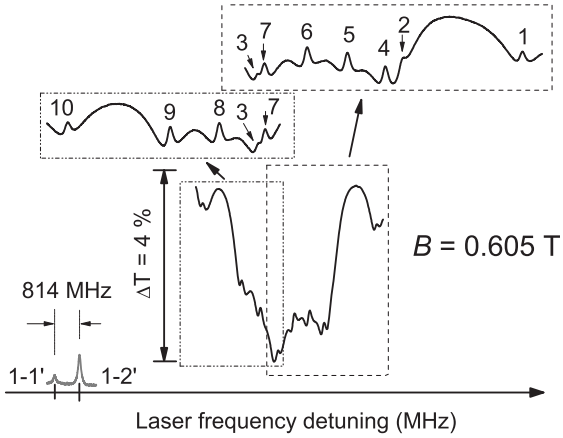

(a) Transmission spectrum of Rb nano-cell with $L = \lambda$ for $B = 0.605$ T and σ^+ laser excitation. Well resolved VSOP resonances located at atomic transitions are labeled $1 - 10$ (six transitions, $4 - 9$ belonging to ^{85}Rb, and four transitions, 1, 2, 3 and 10 belonging to ^{87}Rb). Change in probe transmission is $\Delta T = 4\%$.

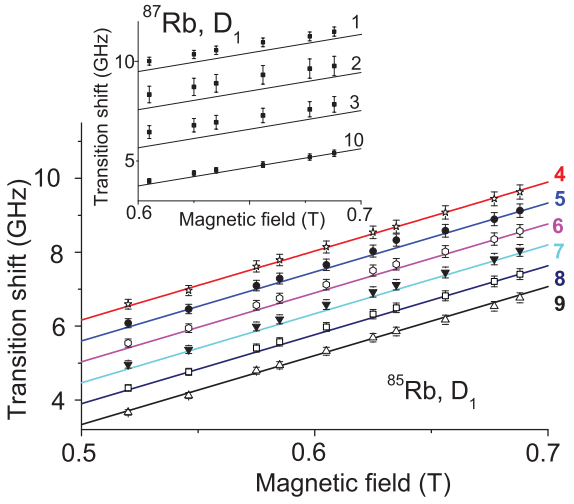

(b) Magnetic field dependence of frequency shift for transition components labeled $4 - 9$ (^{85}Rb) and $1 - 3$, 10 (^{87}Rb, in the inset). Solid lines: theory; symbols: experiment. The inaccuracy is $\leq 2\%$ for components 1, $4 - 9$ and 10; and $\leq 5\%$ for components 2 and 3. Larger error for 3 and 2 is caused by closely located strong transition 7 and location on the transmission spectrum wing, respectively.

Figure 4.22: The experimental and theoretical results.

field required to decouple the nuclear and electronic spins is given by $B \gg A_{hfs}/\mu_B \cong 0.2$ T for ^{87}Rb, and $\cong 0.07$ T for ^{85}Rb, where A_{hfs} is the ground-state hyperfine coupling coefficient for ^{87}Rb and ^{85}Rb and μ_B is the Bohr magneton [125]. For such a large magnetic field the eigenstates of the Hamiltonian are described in uncoupled basis of J and I projections (m_J, m_I). In fig. 4.21(a) six transitions of ^{85}Rb labeled $4-9$, and four transitions of ^{87}Rb labeled $1-3$ and 10 are shown in the case of σ^+ polarized laser excitation for the HPB regime.

The sketch of the experimental setup is shown in fig. 4.21(b). The circularly (σ^+) polarized beam of ECDL ($\lambda = 794$ nm, $P_L = 30$ mW, $\gamma_L < 1$ MHz) resonant with Rb D_1 line, was directed at normal incidence onto the Rb nano-cell 2 with the vapour column thickness $L = \lambda = 794$ nm. The magnetic field was directed along the laser radiation propagation direction $\vec{k}$. About 30% of the pump power was branched to the reference unit with an auxiliary Rb nano-cell. The fluorescence spectrum of the latter at $L = \lambda/2$ was used as a frequency reference for $B = 0$. The magnetic field was measured by a calibrated Hall gauge.

Extremely small thickness of nano-cell is advantageous for application of very strong magnetic fields by permanent ring magnets (PRM) otherwise unusable because of strong inhomogeneity of magnetic field. The ring magnets are mounted on a 50×50 mm^2 cross section Π-shaped holder made from soft stainless steel (see inset in fig. 4.21(b)). Additional form-wounded Cu coils allow of applying extra B-field (up to ± 0.1 T). Nano-cell is placed between PRM. The linearity of the scanned frequency was tested by simultaneously recorded transmission spectra of a Fabry-Pérot etalon (not shown). The nonlinearity has been evaluated to be about 1% throughout the spectral range. The imprecision in the measurement of the absolute B-field value is ± 5 mT.

The recorded transmission spectrum of the Rb nano-cell with $L = \lambda$ for σ^+ laser excitation and $B = 0.605$ T is shown in fig. 4.22(a). The VSOP resonances labeled $1-10$ demonstrate increased transmission at the positions of the individual Zeeman transitions. In the case of HPB the energy of the ground $5S_{1/2}$ and upper $5P_{1/2}$ levels for Rb D_1 line is given by a

simple formula [106]:

$$E_{|J,m_J,I,m_I\rangle} = A_{hfs} m_J m_I + \mu_B (g_J m_J + g_I m_I) B. \tag{4.1}$$

The values for nuclear (g_I) and fine structure (g_J) Landé factors, and hyperfine constants A_{hfs} are given in [100]. The magnetic field dependence of frequency shift for components $4-9$ (^{85}Rb) is shown in fig. 4.22(b) (solid lines: HPB theory; symbols: experiment, inaccuracy does not exceed 2%). The similar dependence for ^{87}Rb (components $1-3$ and 10) are shown in the inset of fig. 4.22(b). The HPB regime condition is fulfilled better for $B > 0.6$ T. As it is seen from Eq. (4.1), and also confirmed experimentally, the dependence slope is the same for all the transition components of both ^{85}Rb and ^{87}Rb: $[g_J(5S_{1/2})m_J + g_J(5P_{1/2})m_J]$ $\mu_B B = 18.6$ MHz/mT (as $g_I \ll g_J$ we ignore its contribution). Onset of this value is indicative of Rb D_1 line HPB regime.

Rb nano-cell could be implemented for mapping strongly inhomogeneous magnetic fields by local submicron spatial resolution. Particularly, for 0.1 T/mm gradient, the displacement of nano-cell by 5 μm results in 10 MHz frequency shift of VSOP resonance, which is easy to detect. Also development of a frequency reference based on nano-cell and PRM, which is B-field-tunable in over 10 GHz range, is of high interest. The above studies and techniques can be successfully implemented also for HPB studies of D lines of Na, K, Cs, and other atoms.

4.7 Summary

1. It is demonstrated experimental justification of computational results considered in ***Chapter III***. We considered three different methods for experimental study: i) "λ-Zeeman technique" - method based on the use of transmission spectrum of a nano-cell of thickness equal to laser radiation wavelength; ii) "$\lambda/2$-Zeeman technique" - method based on the use of narrow-band fluorescence spectrum of a nano-cell of thickness equal

to the half of the laser radiation wavelength; iii) "λ-Fluorescence Zeeman technique" - method based on the use of narrow-band fluorescence spectrum of a nano-cell of thickness equal to laser radiation wavelength.

2. We demonstrated that using these methods, it is possible to study both, frequency shifts and intensity modification of individual transition between Zeeman sublevels of $^{85,\ 87}$Rb D lines for σ^+, π and σ^- polarizations of the laser radiation in the range of magnetic field values $5 - 7000$ G.

3. We considered peculiarities of behaviour of "forbidden" at zero magnetic field transitions.

4. It is developed configuration which allows to measure weak magnetic field of magnitude 5 G.

5. It is studied Paschen-Back regime of ^{87}Rb D_1 line for values of magnetic field $0.5 - 0.7$ tesla $(5000 - 7000$ G).

6. It is demonstrated that interaction with strong magnetic field significantly modifies quantum characteristics of the atomic system.

7. The comparison of theoretical results with experimental data is exhibited for all studied values of the magnetic filed.

Conclusion

In this work, we have proposed a robust tool for magnetometery. Summarizing all results represented in this thesis we may assume, that a large range $\sim 5 - 7000$ G magnetometer based on the use of a nano-cell filled with Rb vapour can be developed.

For this purpose in the first chapter we demonstrated that usage of nano-cell filled with atomic vapours and narrow-band extended cavity diode laser allows to obtain sub-Doppler narrow optical fluorescence resonances and spectrally narrow, close to natural linewidth, VSOP resonances, which allow to realize spectroscopy of high resolution. We have proved advantages of the methods based on use of a nano-cell in comparison with widely utilized methods (Saturated absorption, Selective reflection, Atomic beam, CPT and methods using cells of $0.5 - 1$ cm) of the sub-Doppler spectroscopy. Moreover we may affirm the simplicity of the technical realization, as there is no need to use a supplementary technique and furthermore the absence of auxiliary cross over resonances, with our techniques, increases the resolution of the spectroscopic lines.

In the second chapter we studied the influence of external conditions on the transmission and fluorescence spectra of a nano-cell such as: influence of buffer gas, effect of the laser radiation intensity, quite different behaviours in the spectra due to the cell thickness; and visible changes in these spectra due to the cell temperature. For the first time, it is shown that in the presence of the 6 torr Ne gas, it is possible to detect confidently VSOP resonances in transmission spectra. Also for the first time, it is demonstrated that for all pressures of the

buffer gas, the fluorescence spectra of a nano-cell are narrower than the fluorescence spectra of an ordinary centimeter cell with the same pressures of the buffer gas. This investigation leads to suggest the development of a new "hot" optical manometer based on use of a nano-cell. The main advantage of this manometer its ability to work with hot atomic vapours. Such kind of manometer may help to control and monitor a chemical reaction. Pressure of a gas in the cell may strongly vary in the course of a chemical reaction; that is why it is extremely important to have an adapted tool for the *in situ* pressures monitoring. The use of conventional room-temperature gas pressure gauges, especially for heated cell, is impossible because atomic vapours will condensate in the gauge. Alternatively, a nano-cell can be soldered to the main cell and heated in the same oven up to the needed temperature.

The study of laser radiation intensity, cell thickness and cell temperature influence gave us the opportunity to determine optimal experimental conditions and system stability rate.

Further, in the third chapter we considered a mathematical model describing interaction of the alkali, hydrogen-like, atoms with a magnetic field. This model allowed us to develop a universal, i.e. for all alkali metallic vapours, computational program, calculating energy shifts and intensity modification of the transitions between the Zeeman sublevels of D lines hyperfine structure. To be more precisely we built the Hamiltonian matrix taken into account the interaction between atom and B field. The numerical diagonalization of this matrix gives eigenvalues and eigenvectors of the interacting system. Thus applying the well known Wigner-Eckart theorem to the dipole momentum tensor, we deduced the transition shifts and transition intensities of the perturbed atom. One significant result is that "forbidden" transitions for zero magnetic field appear and may even become stronger than all others transitions. As expected, transitions between non-mixed states after diagonalization preserve their linear characteristics with increasing value of B, while others due to a strong mixing of the initial states exhibit a strong non-linear behaviour.

In the last fourth chapter the previous assertions were confronted with experimental re-

sults. All the figures and graphs in this chapter indicate an excellent agreement between theoretical and experimental points of view. One should notice that these theory-experiment comparisons were made for all possible polarizations of laser radiation and for B-field varying between $5 - 7000$ G. Experimental data, used to compare with theoretical calculations, were obtained through three different techniques, LZT, HLZT and FLZT, which were precisely detailed in this work. An appropriate configuration which allows to measure weak magnetic field ~ 5 G is also presented in this section.

One of the goals of this work was devoted to stress the obvious technologic advantage of the use of the nano-cell to study spectroscopic lines of atomic vapours. One may emphasize that this nano-technology has proven its high efficiency and remarkable adaptability in many others domains of the Physics: van der Waals forces measurement, Electro-magnetically Induced Transparency, Hanle effect, EIT in ladder systems and Rydberg states, ... No doubt that close future will show us many others possibilities of this remarkably efficient nano-tool.

Bibliography

The thesis is based on the following papers

[1] G. Hakhumyan, A. Sargsyan, C. Leroy, Y. Pashayan-Leroy, A. Papoyan, D. Sarkisyan, "Essential features of optical processes in Rb submicron thin cell filled with Neon gas", Opt. Express **18**, 14577 (2010).

[2] D. Sarkisyan, G. Hakhumyan, A. Sargsyan, R. Mirzoyan, C. Leroy, Y. Pashayan-Leroy, "Laser Spectroscopy with Nanometric Cells Containing Atomic Vapor of Metal: Influence of Buffer Gas", Proc. SPIE **7747**, 77470C-1 (2011).

[3] D. Sarkisyan, G. Hakhumyan, A. Sargsyan, Y. Pashayan-Leroy, C. Leroy, "Sub-Doppler features of optical processes in the extremely thin Rb cell filled with an additional buffer gas", Proceedings of conference "Laser Physics - 2009", pp. 5-8, Ashtarak, Armenia (2010).

[4] A. Nersisyan, T. Varzhapetyan, N. Balasanyan, H. Hakhumyan, A. Sarkisyan, "Measurement of the spectral broadening and shift of the Rb D_2 line caused by Nitrogen and Neon gases", Proceedings of conference "Laser Physics - 2005", pp. 21-24 , Ashtarak, Armenia (2006).

[5] C. Leroy, G. Hakhumyan, Y. Pashayan-Leroy, D. Sarkisyan, "Alkali metal atomic transition probability in strong external magnetic field and it's application", Proc. SPIE **7998**, 79980S (2010).

[6] D. Sarkisyan, G. Hakhumyan, R. Mirzoyan, A. Papoyan, A. Atvars, M. Auzinsh, "Use of nanocell with the thickness $L = \lambda$ for study atomic transition of Rb D_2 line in magnetic field", Proceedings of conference "Laser Physics - 2007", pp. 87-90, Ashtarak, Armenia (2008).

[7] G. Hakhumyan, D. Sarkisyan, A. Sargsyan, A. Atvars, M. Auzinsh, "Investigation of Rb D_1 atomic lines in strong magnetic fields by fluorescence from a half-wave-thick cell", Optics and Spectroscopy, Vol. 108, No. 5, pp. 685-692 (2010).

[8] A. Sargsyan, G. Hakhumyan, A. Papoyan, D. Sarkisyan, A. Atvars, M. Auzinsh,"A novel approach to quantitative spectroscopy of atoms in a magnetic field and applications based on an atomic vapor cell with $L = \lambda$", Appl. Phys. Lett. **93**, 021119 (2008).

[9] T.S. Varzhapetyan, G.T. Hakhumyan, V.V. Babushkin, D.H. Sarkisyan, A. Atvars, M. Auzinsh, "Study of atomic spectral lines in a magnetic field with use of a nanocell with the thickness $L = \lambda$", Journal of Contemporary Physics (Armenian Academy of Sciences), Vol. 42, No. 6, pp. 223-229 (2007).

[10] G. Hakhumyan, C. Leroy, Y. Pashayan-Leroy, D. Sarkisyan, M. Auzinsh, "High-spatial-resolution monitoring of strong magnetic field using Rb vapor nanometric-thin cell", Opt. Comm. **284**, 4007 (2011).

[11] G. Hakhumyan, "Optical Magnetometer with submicron spatial resolution based on Rb vapors", Journal of Contemporary Physics (Armenian Academy of Sciences), Vol. 47, No. 3, pp. 105-112 (2012).

[12] G. Hakhumyan, A. Sargsyan, C. Leroy, Y. Pashayan-Leroy, D. Sarkisyan, "Study of Rb Atomic Transitions D_2 Line in Strong Magnetic Field Based on Fluorescence Spectra of Sub-Micron Thin Cell", Proc. SPIE **7998**, 79980V (2010).

[13] G. Hakhumyan, "Usage of the resonant fluorescence from the cell with thickness equal to half-wavelength of the resonant radiation for study of the atomic transitions of D_1 line of Rb atom", Proceedings of conference "Laser Physics - 2009", pp. 33-36, Ashtarak, Armenia (2010).

[14] A.D. Sargsyan, G.T. Hakhumyan, D.H. Sarkisyan,"Usage of Sub-Doppler optical resonances for measurement of weak magnetic fields using an extremely thin cell filled with rubidium vapor", Journal of Contemporary Physics (Armenian Academy of Sciences), Vol. 47, No. 2, pp. 64-72 (2012).

[15] A. Sargsyan, G. Hakhumyan, C. Leroy, Y. Pashayan-Leroy, A. Papoyan, D. Sarkisyan, "Hyperfine Paschen-Back regime realized in Rb nanocell", Opt. Lett. **37**, 1379 (2012).

Conference theses and abstracts

[16] G. Hakhumyan, D. Sarkisyan, A. Sargsyan, C. Leroy, Y. Pashayan-Leroy, "Peculiarities of resonant absorption and fluorescence in extremely thin cell filled with Rb and buffer gas", Book of abstracts "ECAMP-10", Salamanca, Spain P-352 (2010).

[17] A. Papoyan, G. Hakhumyan, A. Atvars, M. Auzinsh and D. Sarkisyan, "Method for quantitative study of atomic transitions in magnetic field based on vapor nanocell with $L = \lambda$", Book of abstract "EGAS - 40", CP-89, p. 111, Graz, Austria (2008).

[18] A. Papoyan, H. Hakhumyan, A. Sargsyan, D. Sarkisyan, A. Atvars, M. Auzinsh, "Quantitative spectroscopy of atoms in a strong magnetic field based on an atomic vapor cell with $L = \lambda$", Book of abstract "EGAS - 41", CP-189, p. 249, Gdańsk, Poland (2009).

[19] G. Hakhumyan, D. Sarkisyan, C. Leroy, Y. Pashayan-Leroy, M. Auzinsh, "Quantitative spectroscopy of Rb atoms in strong magnetic field based on submicron thin vapour", Book of abstracts "ECAMP-10", P-340, Salamanca, Spain (2010).

[20] A. Papoyan, D. Sarkisyan, G. Hakhumyan, C. Leroy, Y. Pashayan-Leroy, "High-spatial-resolution monitoring of strong magnetic field using Rb nano-thin-cell", Book of abstract "EGAS-43", AAP-016, p. 82, Fribourg, Switzerland (2011).

[21] G. Hakhumyan, D. Sarkisyan, C. Leroy, Y. Pashayan-Leroy, "Monitoring of Strong Magnetic field Using Rb or Cs Thin Cell", Book of abstracts "HRMS-22", O26, p. 377, Dijon, France (2011).

[22] G. Hakhumyan, R. Mirzoyan, C. Leroy, Y. Pashayan-Leroy, D. Sarkisyan, "Study of Forbidden Atomic Transitions on D Line Using Rb Nano-cell Placed in External Magnetic Field", Book of abstracts "Laser Physics - 2011", O11, p. 25, Ashtarak, Armenia (2011).

[23] A. Sargsyan, G. Hakhumyan, R. Mirzoyan, C. Leroy, Y. Pashayan-Leroy, D. Sarkisyan, "Atom-wall collisions influence on dark-line atomic resonances in submicron thin vapour cells", Book of abstracts "ECAMP-10", P-339, Salamanca, Spain (2010).

[24] G. Hakhumyan, A. Sargsyan, D. Sarkisyan, C. Leroy, Y. Pashayan-Leroy, "Passive Q-Switching and Frequency Stabilization by Dense Molecular Alkaline Vapor for Laser

Operating in the Range of 500 − 1100 nm", Book of abstracts "HRMS-22", Q26, p. 431, Dijon, France (2011).

[25] D. Sarkisyan, Y. Pashayan-Leroy, C. Leroy, A. Papoyan, G. Hakhumyan, A. Sargsyan, "Selective Addressing of Amplification of Narrow Resonance Formed in Transmission Spectrum of Nano-cell Placed in External Magnetic Field", Book of abstracts "Laser Physics - 2011", O2, p. 16, Ashtarak, Armenia (2011).

References

[26] B. Ai, D.S. Glassner, R.J. Knize, J.P. Partanen, "A thin atomic vapor as a nonlinear optical medium", Appl. Phys. Lett. **64**, 951 (1994).

[27] D.S. Glassner, B. Ai, R.J. Knize, "Low-intensity degenerate four-wave mixing at the cesium D_1 resonance in thin cells", Opt. Lett. **19**, 2071 (1994).

[28] B. Ai, D.S. Glassner, R.J. Knize, "Enhancement of degenerate four-wave mixing by atom-wall collisions in atomic vapors", Phys. Rev. A **50**, 3345 (1994).

[29] A.Ch. Izmailov, "On the possibility of detecting the sub-Doppler structure of spectral lines of gas particles by a single traveling monochromatic wave", Laser Phys. **2**, 762 (1992).

[30] T.A. Vartanyan, D. Lin, "Enhanced selective reflection from a thin layer of a dilute gaseous medium", Phys. Rev. A **51**, 1959 (1995).

[31] B. Zambon, G. Nienhuis, "Reflection and transmission of light by thin vapor layers", Opt. Comm. **143**, 308 (1997).

[32] S. Briaudeau, D. Bloch, M. Ducloy, "Detection of slow atoms in laser spectroscopy of a thin vapor film", Europhys. Lett. **35**, 337 (1996).

[33] S. Briaudeau, S. Saltiel, G. Nienhuis, D. Bloch, M. Ducloy, "Coherent Doppler narrowing in a thin cell: observation of the Dicke regime in the optical domain", Phys. Rev. A **57**, R3169 (1998).

[34] S. Briaudeau, D. Bloch, M. Ducloy, "Sub-Doppler spectroscopy in a thin film of resonant vapor", Phys. Rev. A **59**, 3723 (1999).

[35] S. Briaudeau, S. Saltiel, M. Oria, A.Weis, D. Bloch, M. Ducloy, "Recent developments in sub-Doppler spectroscopy in a thin cell", J. Phys. IV **10**, Pr8-145 (2000).

[36] D. Sarkisyan, D. Bloch, A. Papoyan, M. Ducloy, "Sub-Doppler spectroscopy by sub-micron thin Cs vapour layer", Opt. Comm. **200**, 201 (2001).

[37] D. Sarkisyan, T. Becker, A. Papoyan, P. Thoumany, H. Walther, "Sub-Doppler fluorescence on the atomic D_2 line of a submicron rubidium-vapor layer", Appl. Phys. B **76**, 625 (2003).

[38] D. Sarkisyan, A. Papoyan, T. Varzhapetyan, T. Becker, H. Walther, "Influence of the spectral linewidth of the laser radiation on the sub-Doppler structure in the resonant fluorescence of atomic vapours in a nanocell", Izvestiya of the NAS of Armenia, Physics, Vol. 37, No. 6, pp. 342-349 (2002).

[39] G. Dutier, A. Yarovitski, S. Saltiel, A. Papoyan, D. Sarkisyan, D. Bloch, M. Ducloy, "Collapse and revival of a Dicke-type coherent narrowing in a sub-micron thick vapor cell transmission spectroscopy", Europhys. Lett. **63**, 35 (2003).

[40] G. Dutier, S. Saltiel, D. Bloch, M. Ducloy, "Revisiting optical spectroscopy in a thin vapor cell: mixing of reflection and transmission as a Fabry-Perot microcavity effect", J. Opt. Soc. Am. B **20**, 793 (2003).

[41] G. Nikogosyan, D. Sarkisyan, Yu. Malakyan, "Absorption of resonance radiation and fluorescence of an atomic gas with thickness of the order of a wavelength", J. Opt. Technol. **71**, 602 (2004).

[42] D. Sarkisyan, T. Varzhapetyan, A. Sarkisyan, Yu. Malakyan, A. Papoyan, A. Lezama, D. Bloch, M. Ducloy, "Spectroscopy in an extremely thin vapor cell: comparing the cell-length dependence in fluorescence and in absorption techniques", Phys. Rev. A **69**, 065802 (2004).

[43] A.D. Sargsyan, D.H. Sarkisyan, Y. Pashayan-Leroy, C. Leroy, P. Moroshkin, A. Weis, "Dependence of the cesium absorption D_1 linewidth on the thickness of atomic vapor column", Journal of Contemporary Physics (Armenian Academy of Sciences) Vol. 43, No. 1, pp.7-12 (2008).

[44] W. Demtröder, "Laser Specroscopy: Basic Concepts and Instrumentation" (Springer-Verlag, Berlin, 2nd ed. 1996).

[45] R.H. Romer, R.H. Dicke, "New Technique for High-Resolution Microwave Spectroscopy", Phys. Rev. **99**, 532 (1955).

[46] T. Varzhapetyan, D. Sarkisyan, L. Petrov, C. Andreeva, D. Slavov, S. Saltiel, A. Markovski, S. Cartaleva, "Sub-Doppler spectroscopy and coherent resonances in submicron Cs vapor layer", Proc. SPIE 5830, 196 (2005).

[47] D. Sarkisyan, T. Varzhapetyan, A. Papoyan, D. Bloch, M. Ducloy, "Absorption and fluorescence in submicron cell: high laser intensity case", Proc. SPIE 6257, 625701 (2006).

[48] C. Wieman, T.W. Hanch, "Doppler-free laser polarization spectroscopy", Phys. Rev. Lett. **36**, 1170 (1976).

[49] M. Pinard, C.G. Aminoff, F. Laloe, "Velocity-selective optical pumping and Doppler-free spectroscopy", Phys. Rev. A **19**, 2366 (1979).

[50] J. Bowie, J. Boyce, R. Chiao, "Saturated-absorption spectroscopy of weak-field Zeeman splittings in rubidium", J. Opt. Soc. Am. B **12**, 1839 (1995).

[51] O. Schmidt, K.-M. Knaak, R. Wynands, D. Meschede, "Cesium saturation spectroscopy revisited: How to reverse peak and observe narrow resonances", Appl. Phys. B **59**, 167 (1994).

[52] A. Banerjee, V. Natarajan, "Saturated-absorption spectroscopy: eliminating crossover resonances by use of copropagating beams", Opt. Lett. **28**, 1912 (2003).

[53] T.W. Hansch, I.S. Shahin, A.L. Schawlow, "High-Resolution Saturation Spectroscopy of the Sodium D lines with a Pulsed tunable Dye Laser", Phys. Rev. Lett. **27**, 707 (1971).

[54] R. Grimm, J. Mlynek, "The effect of resonant light pressure in saturation spectroscopy", Appl. Phys. B **49**, 179 (1989).

[55] A.M. Akulshin, A.A. Celikov, V.L. Velichansky, "Nonlinear Doppler-free spectroscopy of the 61S0-63P1 intercombination transition in barium", Opt. Comm. **93**, 54 (1992).

[56] S.D. Badger, I.G. Hughes, C.S. Adams, "Hyperfine effects in electromagnetically induced transparency", J. Phys. B: At. Mol. Opt. Phys. **34**, L749 (2001).

[57] D. Smith, I. Hughes, "The role of hyperfine pumping in multilevel systems exhibiting saturation absorption", American Journal of Physycs **72**, 631 (2004).

[58] R. Drampyan, A.D. Greentree, A.V. Durrant, "Two field nonlinear Faraday rotation in rubidium vapor in a Doppler-free geometry", Opt. Comm. **276**, 251 (2007).

[59] S.A. Knappe, H.G. Robinson, L. Hollberg, "Microfabricated saturated absorption laser spectrometer", Opt. Express **15**, 6293 (2007).

[60] G. Moon, H.-R. Noh, "Analytic solutions for the saturated absorption spectra", J. Opt. Soc. Am. B **25**, 701 (2008).

[61] V.A. Sautenkov, H. van Kampen, E.R. Eliel, J.P. Woerdman, "Dipole-dipole broadened line shape in a partially excited dense atomic gas", Phys. Rev. Lett. **77**, 3327 (1996).

[62] S. Le Boiteux, P. Simoneau, D. Bloch, M. Ducloy, "Doppler-free spectroscopy at a glass-vapour interface by saturated selective reflection at near normal incidence", J. Phys. B: At. Mol. Phys. **20**, L149 (1987).

[63] P. Wang, A. Gallagher, J. Cooper, "Selective reflection by Rb", Phys. Rev. A **56**, 1598 (1997).

[64] M.F.H. Schuurmans, "Spectral narrowing of selective reflection", J. Phys. **37**, 469 (1976).

[65] M. Chevrollier, M. Oria, J.G. de Souza, D. Bloch, M. Fichet, M. Ducloy, "Selective reflection spectroscopy of a resonant vapor at the interface with a metallic layer", Phys. Rev. E **63**, 046610 (2001).

[66] N. Papageorgiou, M. Fichet, V.A. Sautenkov, D. Bloch, M. Ducloy, "Doppler-free reflection spectroscopy of self-induced and krypton-induced collisional shift and broadening of cesium D_2 line components in optically dense vapor", Laser Phys. **4**, 392 (1994).

[67] M. Chevrollier, M. Fichet, M. Oria, G. Rahmat, D. Bloch, M. Ducloy, "High resolution selective reflection spectroscopy as a probe of long-range surface interaction : measurement of the surface van der Waals attraction exerted on excited Cs atoms", J. Phys. II **2**, 631 (1992).

[68] H. van Kampen, A.V. Papoyan, V.A. Sautenkov, P.H.A.M. Castermans, E.R. Eliel, J.P. Woerdman, "Observation of collisional modification of the Zeeman effect in a high-density atomic vapor", Phys. Rev. A **56**, 310 (1997).

[69] A. Papoyan, G. Grigoryan, S. Shmavonyan, D. Sarkisyan, J. Guena, M. Lintz, M.A. Bouchiat, "New feature in selective reflection with a highly parallel window: phase-tunable homodyne detection of the radiated atomic field", Eur. Phys. J. D **30**, 265 (2004).

[70] K.L. Andrew, J.R. Beacham, "Optical study of the hyperfine structure of the rubidium resonance lines", J. Opt. Soc. Am. **61**, 231 (1971).

[71] R. Wynands, A. Nagel, "Precision spectroscopy with coherent dark states", Appl. Phys. B **68**, 1 (1999).

[72] Y. Zhu, T.N. Wasserlauf, "Sub-Doppler linewidth with electromagnetically induced transparency in rubidium atoms", Phys. Rev. A **54**, 3653 (1996).

[73] S. Brandt, A. Nagel, R. Wynands, D. Meschede, "Buffer-gas-induced linewidth reduction of coherent dark resonances to below 50 Hz", Phys. Rev. A **56**, R1063 (1997).

[74] A.M. Akulshin, S. Barreiro, A. Lezama, "Electromagnetically induced absorption and transparency due to resonant two-field excitation of quasidegenerate levels in Rb vapor", Phys. Rev. A **57**, 2996 (1998).

[75] A. Lezama, S. Barreiro, A.M. Akulshin, "Electromagnetically induced absorption", Phys. Rev. A **59**, 4732 (1999).

[76] R. Wynands, A. Nagel, S. Brandt, D. Meschede, A. Weis, "Selection rules and line strengths of Zeeman-split dark resonances", Phys. Rev. A **58**, 196 (1998).

[77] M. Tachikawa, K. Fukuda, S. Hayashi, T. Kawamura, "Sub-Doppler spectroscopy of Cs atoms optically pumped in a thin cell", Jpn. J. Appl. Phys. **37**, L1556 (1998).

[78] K. Fukuda, M. Farukawa, S. Hayashi, M.Tachikawa, "Frequency stabilization of a diode laser with a thin Cs-vapor cell", IEEE Trans. Ultras. Ferr. Freq. Control **47**, 502 (2000).

[79] M. Otake, K. Fukuda, M. Tachikawa, "High-resolution spectroscopy of velocity-selected atoms in a thin cell", Appl. Phys. B **74**, 503 (2002).

[80] A.Ch. Izmailov, "Sub-Doppler spectroscopy based on optical pumping and transit relaxation of atoms in a thin gas cell", Proc. SPIE 6727, 67270B (2007).

[81] K. Fukuda, M. Tachikawa, M. Kinoshita, "Allan-variance measurements of diode laser frequency-stabilized with a thin vapor cell", Appl. Phys. B **77**, 823 (2003).

[82] R. Hamid, M. Celik, E. Sahin, A.Ch. Izmailov, "Sub-Doppler absorption resonances of ring-shaped laser beams in a thin vapor cell", Laser Phys. **16**, 1621 (2006).

[83] A. Mikata, U. Tanaka, Sh. Urabe, "Thin-cell sub-Doppler spectroscopy by spatially separated beam method and pump-probe method", Appl. Opt. **47**, 639 (2008).

[84] D.H. Sarkisyan, A.S. Sarkisyan, A.K. Yalanusyan, "Thermal Dissociation of Cesium Dimers", Appl. Phys. B **66**, 241 (1998).

[85] D. Sarkisyan, U. Hinze, L. Meyer, B. Wellegehausen, "Efficient cw Sodium dimer Raman laser operation in a high-temperature sapphire cell", Appl. Phys. B **70**, 351 (2000).

[86] C. Andreeva, S. Cartaleva, L. Petrov, S.M. Saltiel, D. Sarkisyan, T. Varzhapetyan, D. Bloch, M. Ducloy, "Saturation effects in the sub-Doppler spectroscopy of cesium vapor confined in an extremely thin cell", Phys. Rev. A **76**, 013837 (2007).

[87] S. Cartaleva, S. Saltier, A. Sargsyan, D. Sarkisyan, D. Slavov, P. Todorov, K. Vaseva, "Sub-Doppler spectroscopy of cesium vapor layers with nanometric and micrometric thickness", J. Opt. Soc. Am. B **26**, 1999 (2009).

[88] D. Sarkisyan, A. Papoyan, "Optical processes in micro- and nanometric thin cells containing atomic vapor", New Trends in Quantum Coherence and Nonlinear Optics (Horizons in World Physics, Vol. 263, Nova Science Publishers, 2009).

[89] S. Stenholm, "Foundations of Laser Spectroscopy" (New York: Wiley, 1983).

[90] J.H. Eberly, "Atomic Relaxation in the Presence of Intense Partially Coherent Radiation Fields", Phys. Rev. Lett. **37**, 1387 (1976).

[91] G.S. Agarwal, "Exact Solution for the Influence of Laser Temporal Fluctuations on Resonance Fluorescence", Phys. Rev. Lett. **37**, 1383 (1976).

[92] G.S. Agarwal, "Quantum statistical theory of optical-resonance phenomena in fluctuating laser fields", Phys. Rev. A **18**, 1490 (1978).

[93] V. Chaltykyan, Yu. Malakyan, S. Shmavonyan, A. Papoyan, "Resonant laser-induced formation of caesium hydride molecules in a room temperature vapour cell: experimental results and rate equation calculations", J. Phys. B: At. Mol. Opt. Phys. **37**, 3735 (2004).

[94] A. Badalyan, V. Chaltykyan, Y. Fujii, Yu. Malakyan, M. Ozawa, A. Papoyan, S. Shmavonyan, "Studies of laser induced cesium and rubidium hydride formation in vapor cells and their application for isotope separation", Progress in Nuclear Energy **47**, 389 (2005).

[95] R.H. Dicke, "The effect of collisions upon the Doppler width of spectral lines", Phys. Rev. 89, 472 (1953).

[96] R.S. Eng, A.R. Calawa, T.C. Harman, P.L. Kelley, "Collisional narrowing of infrared water vapor transitions", Appl. Phys. Lett. **21**, 303 (1972).

[97] A.T. Ramsey, L.W. Anderson, "Pressure Shifts in the ^{23}Na Hyperfine Frequency", J. Chem. Phys. **43**, 191 (1965).

[98] T. Varzhapetyan, A. Nersisyan, V. Babushkin, D. Sarkisyan, S. Vdovíc, G. Pichler, "Study of atomic transition self-broadening and shift with the help of a nano-cell", J. Phys. B: At. Mol. Opt. Phys. **41**, 185004 (2008).

[99] C.L. Chen, A.V. Phelps, "Self-Broadening of Cesium Resonance Lines at 8521 and 8944 Å", Phys. Rev. **173**, 62 (1968).

[100] D. A. Steck, "Rubidium 85 *D* line data, Rubidium 87 *D* line data", http://steck.us/alkalidata.

[101] L. Labzowsky, I. Goidenko, Pekka Pyykkö, "Estimates of the bound-state QED contributions to the g-factor of valence n_S electrons in alkali metal atoms", Phys. Lett. A **258**, 31 (1999).

[102] E. Arimondo, M. Inguscio, P. Violino, "Experimental determinations of the hyperfine structure in the alkali atoms", Rev. of Mod. Phys. **49**, 31 (1977).

[103] M. Weissbluth, "Atoms and Molecules" (Academic Press, New-York, 1978).

[104] E. Eriksen, "Foldy-Wouthuysen Transformation. Exact Solution with Generalization to the Two-Particle Problem", Phys. Rev. **111**, 1011 (1958).

[105] P. Tremblay, A. Nichaud, M. Levesque, S. Theriault, M. Breton, J. Beaubien, N. Cyr, "Absorption profiles of alkali-metal D lines in the presence of a static magnetic field", Phys. Rev. A **42**, 2766 (1990).

[106] E.B. Aleksandrov, M.P. Chaika, G.I. Khvostenko, "Interference of Atomic States" (Springer-Verlag, New York, 1993).

[107] M. Auzinsh, D. Budker, S.M. Rochester, "Optically polarized atoms: understanding light-atom interactions" (Oxford University Press, 2010).

[108] M. Rotenberg, R. Bivins, N. Metropolis, J.K. Wooten Jr, "The 3-J and 6-J symbols" (Technology Press, 1959).

[109] V. Papoyan, D.H. Sarkisyan, K. Blush, M. Auzinsh, D. Bloch, M. Ducloy, "Magnetic Field-Induced Mixing of the Cs $6^2P_{3/2}$ Level Observed with a Submicron Vapor Cell", Laser Phys. **13**, 1 (2003).

[110] R. Loudon, "The Quantum Theory of Light" (Oxford University Press, 2nd ed. 1983).

[111] D. Budker, W. Gawlik, D. Kimball, S.R. Rochester, V.V. Yaschuk, A. Weis, Rev. Mod. Phys. **74**,1153 (2002).

[112] D. Budker, D.F. Kimball, D.P. DeMille, "Atomic Physics: an exploration through problems and solutions"(Oxford University Press, 2004).

[113] D. Meschede, "Optics, Light and Lasers: The practical Approach to Modern Aspects of Photonics and Laser Physics" (WILEY-VCH Verlag GmbH&Co. KGaA, Weinheim, 2nd ed. 2004).

[114] N. Papageorgiou, A. Weis, V. Sautenkov, D. Bloch, M. Ducloy, "High-resolution selective reflection spectroscopy in intermediate magnetic fields", Appl. Phys. B **59**, 123 (1994).

[115] M.U. Momeen, G. Rangarajan, P.C. Deshmukh, "Variations of intensity in Rb D_2 line at weak/intermediate fields", J. Phys. B: At. Mol. Opt. Phys. **40**, 3163 (2007).

[116] G. Školnik, N. Vujicic, T. Ban, "Optical pumping of the Zeeman components in the rubidium vapor", Opt. Comm. **282**, 1326 (2009).

[117] D. Sarkisyan, A. Papoyan, T. Varzhapetyan, K. Blush, M. Auzinsh, "Fluorescence of Rb in a sub-micron vapor cell: spectral resolution of atomic transitions between Zeeman sublevels in moderate magnetic field", J. Opt. Soc. Am. B **22**, 88 (2005).

[118] D. Sarkisyan, A. Papoyan, T. Varzhapetyan, J. Alnis, K. Blush, M. Auzinsh, "Sub-Doppler spectroscopy of Rb atoms in a sub-micron vapor cell in the presence of a magnetic field", J. Opt. A: Pure and Appl. Opt. **6**, S142 (2004).

[119] D. Sarkisyan, A. Papoyan, T. Varzhapetyan, K. Blush, M. Auzinsh, "Zeeman effect on the hyperfine structure of the D_1 line of a submicron layer of ^{87}Rb vapor", Optics and Spectroscopy, Vol. 96, No. 3, pp. 328-334 (2004).

[120] J.A. Zielinska, F.A. Beduini, N. Godbout, M.W. Mitchell, "Ultra-Narrow Faraday Rotation Filter at the Rb D_1 Line", arXiv:1110.2362v1 [physics.optics] 11 Oct (2011).

[121] M. Fleischhauer, A. Imamoglu, J.P. Marangos,"Electromagnetically induced transparency: Optics in coherent media", Rev. Mod. Phys. **77**, 633 (2005).

[122] S.M. Iftiquar, V. Natarajan, "Line narrowing of electromagnetically induced transparency in Rb with a longitudinal magnetic field", Phys. Rev. A **79**, 013808 (2009).

[123] S. Knappe, L. Hollberg, J. Kitching, "Dark Line Resonances in Sub-Millimeter Structures", Opt. Lett. **29**, 388 (2004).

[124] T. Baluktsian, C. Urban, T. Bublat, H. Giessen, R. Löw, T. Pfau, "Fabrication method for microscopic vapor cells for alkali atoms", Opt. Lett. **35**, 1950 (2010).

[125] B. A. Olsen, B. Patton, Y.-Y. Jau, W. Happer, "Optical pumping and spectroscopy of Cs vapor at high magnetic field", Phys. Rev. A **84**, 063410 (2011).

Table of abbreviations

BEC - Bose-Einstein condensate

CO - Cross over

CPT - Coherent population trapping

CW - Continuous wave

DCN - Coherent Dike narrowing

DG - Diffraction grating

DL - Diode laser

ECDL - Extended cavity diode laser

EIT - Electro-magnetically induced transparency

FI - Faraday isolator

FL - Fluorescence

FM - Frequency modulation

FWHM - Full width on the half maximum

HLZT - $\lambda/2$-Zeeman technique

HPB - Hyperfine Paschen-Back

LFZT - λ-Fluorescence Zeeman technique

LZT - λ-Zeeman technique

MRC - Multi-region cell

OP - Optical pumping

PBS - Polarization beam splitter

PRM - Permanent ring magnet

PZT - Piezoelectric

rme - Reduced matrix element

SA - Saturated absorption

SR - Selective reflection

VSOP - Velocity selective optical pumping

Title: Study of optical and magneto-optical processes in Rb atomic vapor layer of nanometric thickness.

Abstract: Using a narrow-band resonant fluorescence spectra from a nano-cell with a thickness of $L = \lambda/2$, and VSOP resonances formed at a thickness $L = \lambda$ (λ is the wavelength of the resonant radiation), for the first time it was experimentally investigated the behaviour of the frequency and intensity (transition probabilities) of the atomic hyperfine structure transitions between the ^{85}Rb, ^{87}Rb, D_1 and D_2 lines Zeeman sublevels in external magnetic fields in range $5 - 7000$ G. The behaviour of tens of previously unstudied atomic transitions was analyzed and it is demonstrated that the intensities of these lines can both greatly increase, and decrease (tenfold).
For the first time it is demonstrated that, in the case of partial pressure of neon buffer gas up to 6 torr into the nano-cell of thickness $L = \lambda$ filled with Rb, VSOP resonances are recorded confidently, while the addition of 0.1 torr neon buffer gas in a cell of a centimeter thickness leads to the complete disappearance of VSOP resonances formed with the help of the widely used technique of saturated absorption. It is demonstrated for the first time that the spectral width of the resonant fluorescence spectra of the rubidium nano-cell with thickness $L = \lambda/2$, for all values of the neon buffer gas pressures is much narrower ($6 - 8$ times) compared with the resonant fluorescence spectra of an ordinary centimeter cell containing rubidium with the same pressures of neon.

Key words: Rb hyperfine structure; diode laser; high resolution spectroscopy; nano-cells; combined multi-region cells; buffer gas; Coherent Dicke narrowing; Zeeman effect; VSOP resonances; "forbidden" transitions; σ^+, π and σ^- polarizations of the laser radiation.

Titre : Etude des processus optiques et magnéto-optiques dans une couche de vapeur de rubidium atomique d'épaisseur nanométrique.

Résumé : A l'aide d'un spectre de fluorescence de résonance à bande étroite obtenu avec une nano-cellule d'épaisseur $L = \lambda/2$ et des résonances VSOP formées pour une épaisseur $L = \lambda$ (λ est la longueur d'onde de la radiation résonnante), cette thèse présente pour la première fois une étude expérimentale du comportement en fréquence et en intensité (probabilités de transition) des transitions atomiques de la structure hyperfine entre sous-niveaux Zeeman des raies D_1 and D_2 pour le ^{85}Rb et le ^{87}Rb en présence de champs magnétiques extérieurs compris entre 5 et 7000 G. Le comportement d'une dizaine de transitions atomiques inétudiées à ce jour a été analysé et nous avons démontré que l'intensité de ces raies peut montrer alternativement de grandes variations : jusqu'à un facteur 10 de taux de croissance ou de décroissance.
Pour la première fois, nous avons parfaitement enregistré des résonances VSOP dans le cas où un gaz tampon (néon de pression partielle 6 torr) est introduit dans la nano-cellule d'épaisseur $L = \lambda$, alors que l'addition d'un gaz tampon (néon) même à une pression partielle de 0,1 torr, dans une cellule d'épaisseur centimétrique conduit à une complète disparition de ces résonances VSOP obtenues par la méthode usuelle d'absorption saturée. Enfin, nous avons montré pour la première fois que la largeur spectrale d'un spectre de fluorescence de résonance d'une nano-cellule de rubidium d'épaisseur $L = \lambda/2$, quelques soient les pressions du gaz tampon (néon), est beaucoup plus étroite (6 à 8 fois) que celle obtenue avec une cellule centimétrique de rubidium pour les mêmes valeurs de pressions.

Mots clefs : Structure hyperfine Rb ; diode laser ; spectroscopie à haute résolution ; nano-cellules ; cellules multi-régions combinées ; gaz tampon ; rétrécissement Dicke cohérent ; effet Zeeman ; résonances VSOP ; transitions "interdites" ; polarisations σ^+, π et σ^- du rayonnement laser.